CORROSION OF THERMALLY-AGED ADVANCED GAS-COOLED REACTOR FUEL CLADDING

By:

PHUAH, CHIN HENG
(CID# 00577443)

Submitted in partial satisfaction of the requirements for the degree of:

DOCTOR OF PHILOSOPHY

in the:

DEPARTMENT OF MATERIALS
IMPERIAL COLLEGE LONDON

SEPTEMBER 2012

Abstract

The microstructure of Advanced Gas-Cooled Reactor (AGR) fuel cladding that underpins its corrosion behaviour has been established, contributing to an understanding of long-term control, monitoring practice and storage decisions for this fuel. AGR fuel cladding specimens sourced from Sellafield Ltd, cut and individually heat treated at temperatures from 400 to 800°C for 24 to 192h were attempts to approximate irradiated AGR fuel cladding and characterised both in terms of their corrosion behaviour and of microstructure. Niobium carbide (NbC) second phases are the primary local corrosion sites. Bulk austenite-γ cladding metal (50.3±1.7 at% Fe, 21.0±1.1 at% Cr and 21.0±0.4 at% Ni) around NbC precipitates exhibited extensive corrosion even though the precipitate themselves appear unchanged. Corrosion observed from the specimen surface took the form of lacy covers around an NbC precipitate at the cover centre (~10 to 25 μm dia. depending on the site) and in the subsurface were voids (~0.1 μm pin-holes), cavities (~2 to 5 μm), an envelope of dissolved-metal region along NbC peripheries (~1 μm thick with austenite-γ composition decreased by on average 20% Fe, 21% Cr and 17% Ni) or a large, smooth concave pit bottom comparable to the cover dimension. These observations collectively suggest that AGR cladding corrosion is a diffusion-controlled phenomenon where the NbC precipitate may act as the cathode in a local galvanic couple and the adjacent austenite-γ metal is the anode that undergoes preferential oxidation. The primary contributing factors to NbC-induced AGR cladding corrosion are high NaCl concentration of the electrolyte solution, large NbC precipitates, small austenite-γ grains and presence of stress in the microstructure. Specifically, corrosion potential measurements in the 0.001M electrolyte NaCl are ~800mV (v.s. Ag|AgCl reference electrode) more noble than in the 0.1M electrolyte, suggesting that cladding wet storage requires maintenance with lowest chloride concentration practically achievable. Specimens with comparatively large NbC precipitates (~5 μm) and small austenite-γ grains (~10 μm) that result from heat treatment are ~810mV more corrosion susceptible than the as-received specimens with ~0.1 dia. NbC precipitate and ~25 μm austenite-γ grains. Increased dislocation densities were observed adjacent to the grown-NbC precipitate, imparting a stress-corrosion effect on the AGR cladding corrosion.

Table of Contents

Acknowledgements

I dedicate this thesis to my father Phuah Ah Thong and my mother Yap Yoke Peng without whose love and support it could not have been written. I have also been writing with much inspiration from my brothers Kenny and Benny from whom every encouraging long distance calls I was periodically able to put a pair of fresh lenses into the project. With the deepest gratitude, I must especially thank Leo Bey Fen, who rekindled my spirits by sparks from her love during the times when I experienced low.

I am able to produce and accomplish this thesis because of Professor William Lee and Professor Mary Ryan. I am indebted to their guiding and stimulating the progress of my research in Imperial College London and, recently, correcting the many versions of drafts in their valuable time which made the thesis consistent and coherent. I would like to thank Dr. Paul Standring and Dr. Paul Cook at Sellafield Limited for providing samples, as well as the Engineering and Physical Science Research Council (EPSRC) through the Decommissioning Immobilisation and Management of Nuclear Waste for Disposal (DIAMOND) University Consortium and the Department of Materials for providing research funds and nuclear training courses throughout my study. I am most grateful to Mr. Richard Chater, Dr. Mahmoud Ardakani, Mr. Robert Rudkin and Dr. Ecaterina Ware who taught me experimental techniques and provided invaluable suggestions for characterising my samples. I must also thank Mr. Stephen Ramsay, Mr. Russell Stracey and Mr. Phil Jones of the mechanical workshop who on occasions when time was most pressing promptly repaired the broken glass-pieces of my electrochemistry kit and operated the heavy machineries to shape my samples so I could meet conference deadlines. I must thank Mr. Benjamin Chan and Ms. Norma Hikel for their assistance in the laboratory and department throughout my study. I especially would like to thank Prof. John Cosgrove, Dr. Rob Theid, Dr. Barry Jones and Ms. Gill Davies for their unwavering encouragement in my studies.

During my academic training I have been fortunate to have gained from the philosophies, teachings and friendship of my past mentors and supervisors who have opened up my doors to the world. I am truly grateful to Dr. Ann Dillner, Dr. Warren White, Dr. Nicole Hyslop, Prof. Shaliza Ibrahim, Assoc. Prof. Thomas Young,

Assoc. Prof. Michael Kleeman, and Dr. Sumiani Yusoff from whom I learned at the University of California Davis and University of Malaya. I would also like to thank family and friends whose experiences and interactions have inspired not only my thesis but also many other aspects of my life; I am grateful to Uncle Kim, Uncle Jason, Uncle William and Aunty Melinda, Ying Yng Choy, Kathryn Tyson, Anne Beard, Cate Klepacki, Dr. Stephen McCord, Ben and Mary Giudice, Dr. Jon Leatherbarrow, Jennifer Wilson, Elisabet Goula, Melanie Nägele, Dr. Esther Valliant, Dr. Frédéric Aguesse, Marié-Christiné Esposito, Tim "Dr." Crouch and Edoardo Giorgi.

Finally, I want to thank all individuals who will read my thesis about metallurgy and corrosion. It has been a unique opportunity to document such a highly-specialised and important subject. It was composed over many excellent, fine times during the process, and of course also times of stretching that require resilience. It develops the thought process, critical thinking and analytical skills that I am sure are useful in many things continuing. It cultivates good disposition and personality that I am sure can carry me further than most things in life.

List of Figures

List of Tables

List of Appendices

1.0 Introduction

1.1 Research Problem Overview

The Advanced Gas-Cooled Reactor (AGR) has been the primary generation of nuclear electricity in the UK for the past several decades, producing ~15% of the nation's electricity at its peak. Corrosion of the spent AGR fuel cladding – the metal rod that encapsulate the ~4%-enriched uranium oxide fuel pellets and made of austenite-γ stainless steel 20Cr/25Ni/Nb (50.3±1.7 at% Fe, 21.0±1.1 at% Cr, 21.0±0.4 at% Ni and 0.07 at% Nb) – have important, long term implications due to the long-lived radioactive fission products that are contained within the cladding which microstructure adversely impacted from radiation damage effects. The implications are their management measures that include interim storage, handling, transport and geological disposal.

Currently, spent fuels arise from seven AGR power stations (Dungeness B, Hinkley Point B, Hunterston B, Hartlepool, Heysham 1 &2, and Torness). Their subsequent interim store lifecycle include boric acid storage in station ponds for several months, a pond dosed with corrosion inhibitors caustic soda at pH 11.4 or an undosed pond that are maintained with demineralised water at pH7 in Sellafield (following rail transfer) and potentially emplacement in a geological disposal facility (GDF) that would be available around year 2075.

Overall, interim storage of the spent fuels under wet environments, hence corrosion concern of the fuel cladding, are expected to last for several decades and may even extend in the GDF environments should a first wet condition potentially occur beyond year 2075. So, while the current use of corrosion inhibitor has demonstrated measurable success in controlling cladding corrosion, the underlying corrosion mechanisms and its mode of control has nonetheless been an important subject in order to provide a more comprehensive understanding on the implications of AGR spent fuel management strategy.

The focus of the investigation reported in this thesis is the impact of microstructure and secondary phase formation on Advanced Gas-Cooled Reactor (AGR) fuel cladding corrosion in chloride aqueous solutions, amongst other known corrosion factors which include radiation-induced segregation and thermal sensitisation. The experimental conditions of the investigation are reflective of the

AGR fuel cladding storage in the demineralised-water Receipt and Storage Pond at the Thermal Oxide Reprocessing Plant (THORP). THORP, built in 1994 and situated in Sellafield, Cumbria, is a facility that reprocesses both the AGR spent fuels and the Light Water Reactors' (LWR) that were contracted from overseas customers to recover plutonium and uranium for Mixed-Oxide (MOX) fuel fabrication and to separate fission products (FPs) for improving its management. The fuels are interim stored in the pond for approximately five years until their decay heat dissipates to safe levels for reprocessing to be undertaken or, the more recent proposal, permanent disposal in a geological repository. Due to Sellafield's coastline proximity, trace amounts of environmental constituents that originate from the sea-salt particles or aerosol droplets including sodium, chloride and sulphate, about 50ppm, have been accidentally introduced into the pond which pose corrosion concerns [1, 2].

Both the AGR and LWR spent fuels stored in the Receipt and Storage Pond are stored in stainless steel containers (Figure 1) to minimise leakage risk and provide criticality control. Specifically, the AGR fuel elements are encased in stainless steel 316L 'skips' whereas the LWRs are in Multi-Element Bottles (MEB) that are lined with neutron-absorbing boronated-aluminium plates or 'Boral' [2]. In addition to the container metals, the fuel cladding that maintains the structural integrity of the fuels containing FPs is made of austenitic stainless steel 20Cr/25Ni/Nb for the AGRs whereas Zircaloy or Zirconium Alloy for the LWRs. There has, therefore, been no dosage to the demineralised-water with corrosion inhibitors or other pH control measures because co-location of the metal mixes may risk complex electrochemical behaviour. The pond is currently maintained with high-quality demineralised-water in a reinforced concrete pool with water circulation to provide decay heat removal and filtration to ensure thorough mixing of freshly treated water returning from the demineralising chemical plant.

The recent Nuclear Decommissioning Authority (NDA) strategic plan has required extending both the AGR and LWR spent fuel in THORP's Receipt and Storage Pond for a further 80 years [2]. From THORP's spent fuel storage technical department standpoint, currently with about 20 years of operating experience, this strategy requires a safety case for long-term integrity of the fuel cladding against corrosion in the ponds, either through employing a potential corrosion inhibitor that

is compatible with both the AGR and LWR fuels and their containers or demonstrating the viability of demineralised-water as a long term storage solution [3]. On-going studies which include work by Herbert *et al.* [4] and Hands *et al.* [5, 6] have identified that nitrate-based corrosion inhibitor are compatible with both the AGR and LWR fuels, thus a potentially viable long term storage solution. Note that the *AGR Storage Pond* (not in THORP) that stores only the AGR spent fuel currently employs caustic soda (NaOH) at pH 11.5 as corrosion inhibitor that has successfully controlled austenitic stainless steel corrosion – not an option, however, for the *Receipt and Storage Pond* because caustic soda is corrosive to aluminium in the LWR's MEB via the dissolution reaction $Al(s)+NaOH(aq)\rightarrow Al(OH)^{4-}(aq)+H_2(g)$. Whilst empirical data showed that the use of both nitrate and caustic soda corrosion inhibitor can arrest AGR fuel cladding corrosion (see work by Herbert *et al.* [4] and Hands *et al.* [5, 6]), the microstructures and mechanisms that underpin this corrosion control or behaviour have not been clarified. This thesis investigates the latter to contribute to informing the long-term aqueous corrosion control, monitoring practice or storage decisions (e.g. dry storage in geological repository) of the AGR spent fuel.

As a general overview, this investigation involves sourcing an as-manufactured AGR fuel cladding from Sellafield Ltd as the raw material for experimentation. The associated experiments have been carried out in a non-irradiative environment with the advanced microstructure characterisation capabilities in the Materials Department of Imperial College London under the aims outlined in Work Package 3 (WP3) of the Decommissioning, Immobilisation and Management of Nuclear waste for Disposal (DIAMOND) Universities research consortium working in collaboration with industry supervisers from THORP Technical Department, Sellafield Ltd. The sourced cladding was subjected to temperature processing between 400 and 800°C that mimics the gradient or hot-spots along the cladding's one metre length and was subsequently tested for corrosion susceptibility at low chloride concentrations (0.001M) close to that measured in the demineralised-water pond. The relationship between corrosion susceptibility and the variety of microstructures and secondary phase size and distribution that renders it corrosion susceptible, including corrosion morphologies and their aspect ratios and grain and grain boundary chemical compositions, are established in this thesis.

LWR fuel elements (~5m long) with Zircaloy fuel cladding

AGR fuel elements (~1m long) with austenitic 20Cr/25Ni/Nb stainless steel fuel cladding in AGR's 'skips' made of stainless steel 316L

LWR's Multi-Element Bottles made of aluminium alloy

Demineralised-water Pond Storage

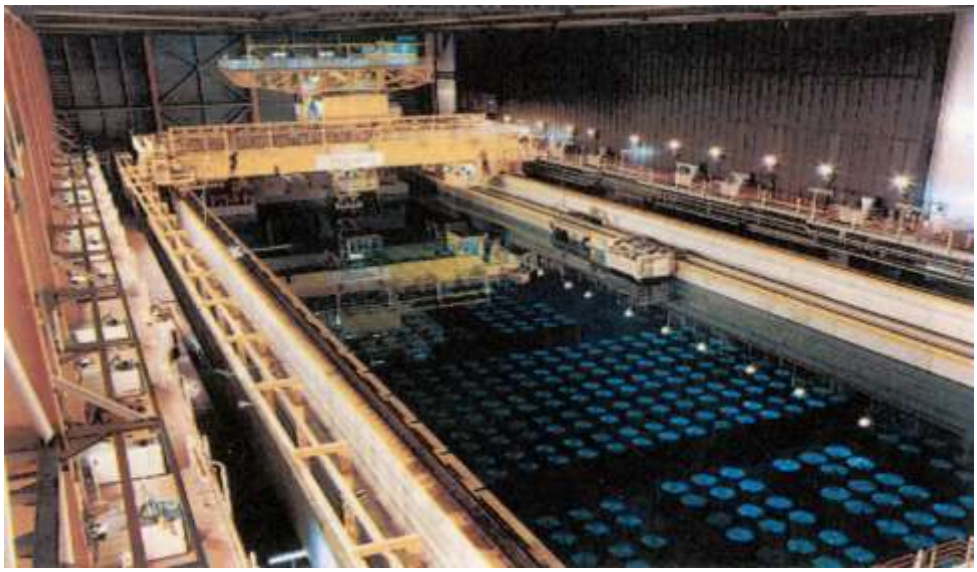

Figure 1 – Spent AGR fuel storage in THORP Receipt and Storage Pond

1.2 Research Objectives

The experimental approach for investigating the relations between microstructure and secondary phases of the AGR fuel cladding and its associated corrosion behaviour is schematically illustrated in Figure 2. The specific research objectives are:

I. Identification from the literature of the AGR fuel cladding temperature processing conditions and in the reactor as well as storage conditions in the demineralised-water pond to simulate laboratory conditions that mimics *in-situ* corrosion environment.

II. Production of a varied microstructure of the as-sourced AGR fuel cladding specimens that have been individually thermally-aged at discrete temperatures of 400, 500, 600, 700 and 800 °C for 24, 48, 96 and 192 hours and fabricated as electrodes. The thermal aging employed simulates the temperature range across the eight AGR fuel elements, stacked that form a stringer in AGR reactors.

III. Establishment of the effect of chloride concentrations on AGR fuel cladding corrosion through corrosion potential quantification, using the anodic polarisation method, of the thermally-aged specimens (fabricated as electrodes) in both 0.001M and 0.1 M sodium chloride (NaCl) electrolyte.

IV. Characterisation of the *surface* corrosion morphology of the post-polarised electrodes by Scanning Electron Microscopy (SEM).

V. Characterisation of the *subsurface* corrosion morphology of the post-polarised electrodes; specifically Focused Ion Beam (FIB) cross-sections were acquired from subsurface corrosion morphologies of interest and subsequently characterised by Transmission Electron Microscopy (TEM) for chemical composition of the austenite grains, grain boundaries and secondary phases using Energy Dispersive X-ray Spectroscopy (EDS).

VI. Development of a suitable etchant for revealing in the SEM the physical distribution of the austenite grains, grain boundaries and secondary phases that are varied due to thermal-aging. This includes development of an approach for quantifying the distribution of secondary phases by image processing.

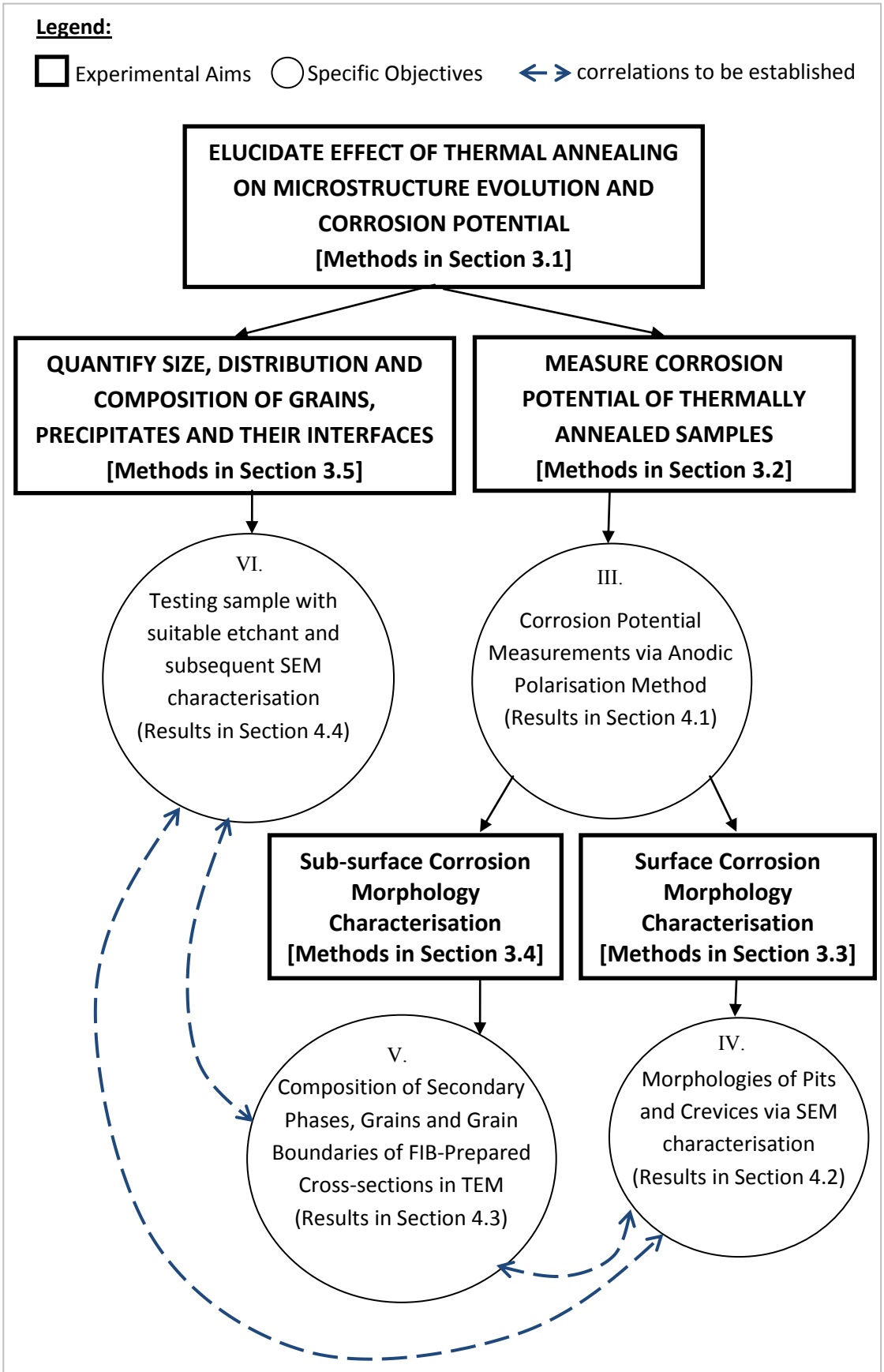

Figure 2 – Schematic illustration of experimental approach

1.3 Organisation of Thesis

This thesis is organised in seven chapters. *Chapter 1.0 Introduction* herein describes the research problem, objectives of the study and structure of the thesis. *Chapter 2.0 Literature Review* retrieved literature relating to three key areas: i) development, lifecycle and metallurgical properties of the AGR fuel cladding, ii) effects of radiation damage and high-temperature oxidation on the fuel cladding, and iii) metal corrosion processes that are relevant to the AGR fuel cladding drawn from corrosion studies of other materials. C*hapter 3.0 Methods* describes the specific characterisation techniques, for example electrode fabrication from the thermally-aged cladding specimens and a detailed description of the anodic polarisation method employed for their corrosion tests, and targeted measurements which were employed to achieve the research objectives above outlined. *Chapter 4.0 Results and Discussion* links the critical microstructural factors for AGR fuel cladding corrosion susceptibility, which includes results from the corrosion potential measurements, surface and subsurface corrosion morphologies and physical microstructural features revealed by the etched electrodes. In *Chapter 5.0 Summary* the relevance of study for the long-term corrosion control, monitoring and storage decisions of the AGR fuel cladding are discussed. *Chapter 6.0 Conclusions and Future Work* underlines the key strengths and contributions specific to this study and to corrosion science in general and suggests opportunities for future experiments that have led from the conclusions. *Chapter 7.0 References* provides a reference list to the Literature Review and Discussion sections. An *Appendix* concerning the image processing algorithms developed for determining the electrode surface area in the corrosion potential measurements (used in normalisation of the measured current) is included.

2.0 Literature Review

2.1 Overview of Advanced Gas-Cooled Reactor (AGR) Fuel Cladding

Within a nuclear fuel element *fuel cladding* is the component that encapsulates the *nuclear fuels.* The fuel cladding is made of rigid materials, commonly stainless steel or other alloys that possess relatively high structural strength, in order to maintain the geometry of the nuclear fuels against excessive swelling [7, 8] and contain internal gas pressure. Swelling or buckling of nuclear fuels is a result of neutron irradiation that is principally attributed to the accumulation of three primary fission gases: helium from (n,α) decay reactions and krypton-85 (Kr-85) and xenon-133 (Xe-133) from fission reactions. Figure 3a shows a fission gas 'bubble' that

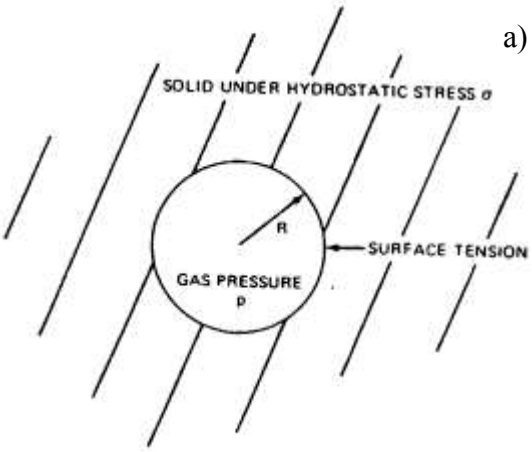

a) volume of fission gas molecule ($4\pi r^3/3$, r = radius) exerting pressure (p) on the fuel matrix

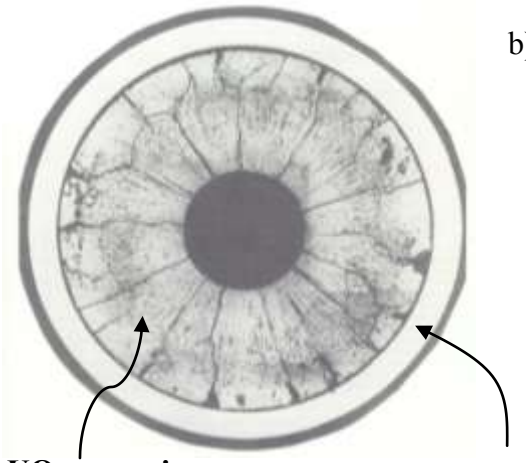

b) cross-section of nuclear fuel and cladding, adapted from Glasgow *et al.* [7]

UO_2-ceramic Nuclear Fuel

Fuel Cladding

Figure 3 – Nano and macro–scale depiction of uranium dioxide UO_2 nuclear fuel swelling.

exerts stresses on the adjacent solid in the nuclear fuel matrix. Continuous irradiation promotes coalescence of the initial bubbles to form larger bubbles that, due to the volume they occupy, cause considerable build-up of radial cracks in the fuel and stresses to the internal walls of the cladding [7]. Note that the hollow space in the fuel centre (Figure 3b) is designed to accommodate fission gases. In certain fuel element designs, both ends of the fuel incorporate additional free spaces called a 'plenum' for this purpose. Figure 4 depicts the mechanical impact of fuel swelling on the cladding which includes pellet-clad interactions and regions of stress concentration along the length of the cladding. The primary objective of the fuel cladding is, therefore, to provide adequate containment of the fuel against rupture that might lead to escape of FPs to the environment.

Conforming to the 'strong' cladding requirement, the AGR employs an austenitic stainless steel cladding, around the 4% enriched uranium dioxide (UO_2) fuel pellets, that has a nominal alloy composition of 20%wt Cr and 25%wt Ni stabilised with 0.7%wt Nb. Commonly known as the 20/25/Nb steel, Figure 5 illustrates the metal possesses one of the best high-temperature mechanical performances indicated by its excellent 1000-hour rupture strength [9].

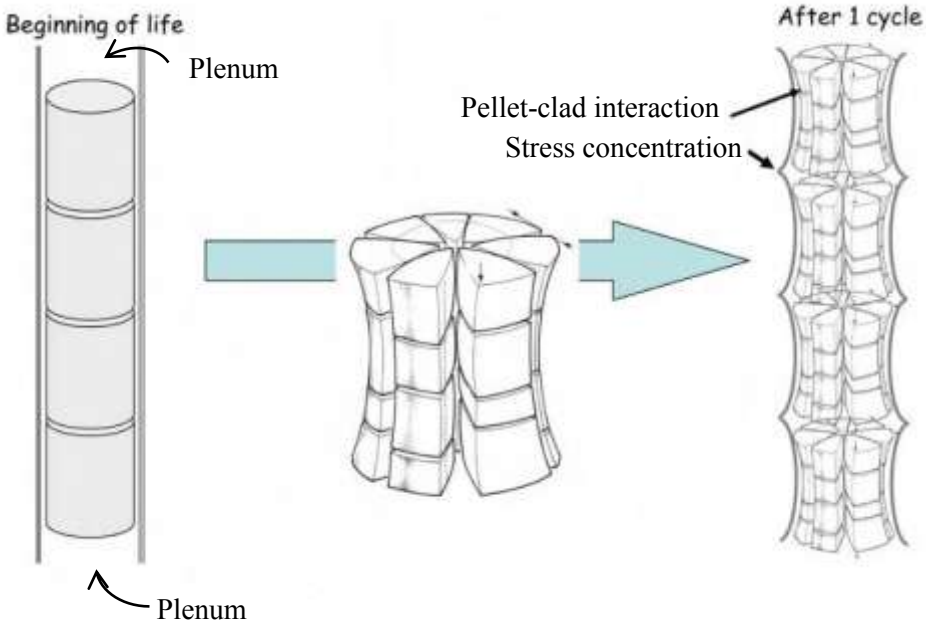

Figure 4 – Effects of fuel swelling on cladding, adapted from Olander [34]

Figure 6a shows an AGR fuel cladding. It measures one metre long by one-and-a-half centimetres diameter with 0.38 millimetres (mm) wall thickness. There are circumferential threads that are 0.31 mm tall at every 2.5 mm pitch to improve heat transfer with the circulating carbon dioxide (CO_2) gas coolant. The cladding encapsulates sixty-four UO_2 fuel pellets (Figure 6b), each measuring 13 mm tall, 13 mm outer diameter and 1.5 mm diameter at the hollow region at the centre of the fuel pellet that are intended for fission gas accommodation and reduce fuel peak temperature. The fuel pellets that are contained and secured within the fuel cladding are referred as a unit of *fuel pin.* Figure 6c shows that a unit of AGR *fuel element* consists of thirty-six fuel pins which are secured by metal braces (also 20Cr/25Ni/Nb steel) which maintain the fuel pins-element geometry [10]. Surrounding the fuel pins are the neutron-moderating graphite sleeves. The fuel element is readily employable by the AGR reactor core for on-load refuelling without powering-down.

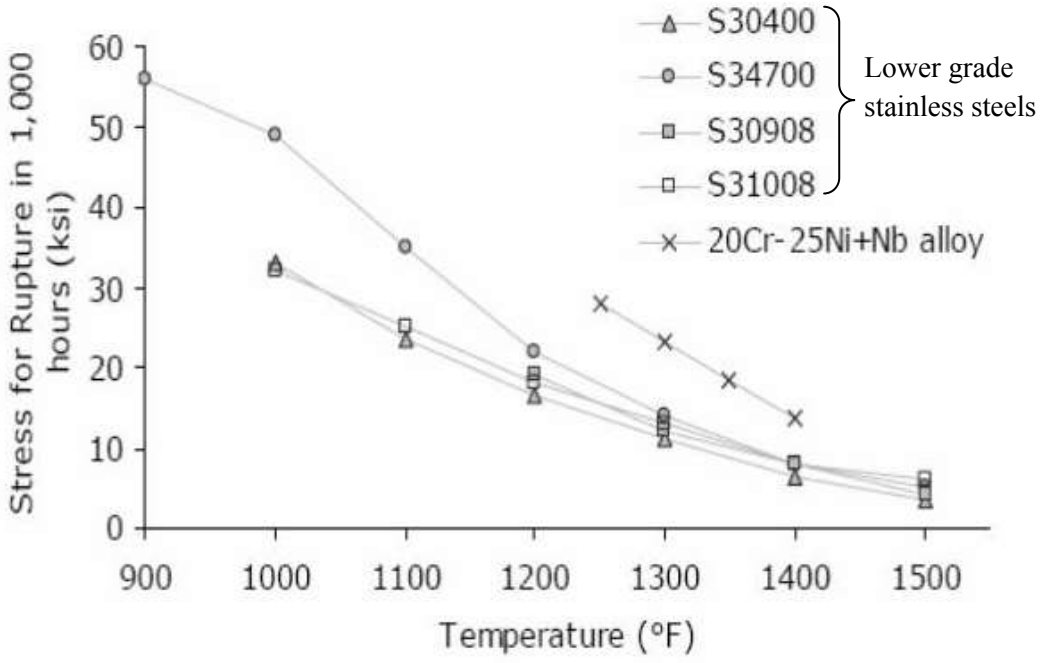

Figure 5 – 1000-hour rupture strength of selected austenitic stainless steels, adapted from ATI Allegheny Ludlum Brochure [9]

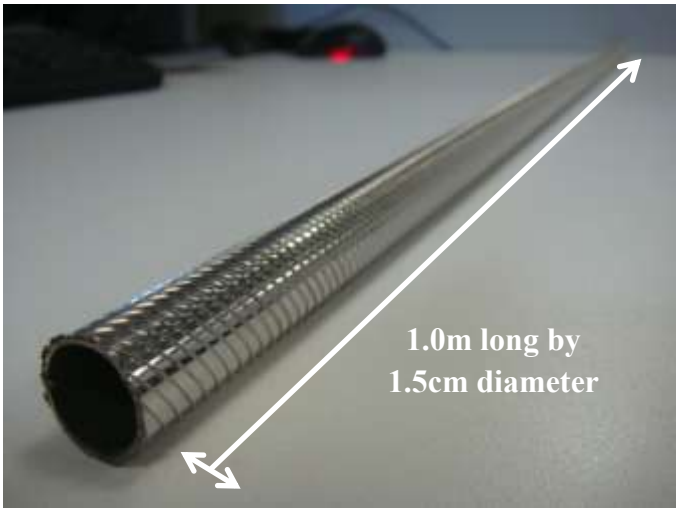

a) AGR fuel cladding and dimension

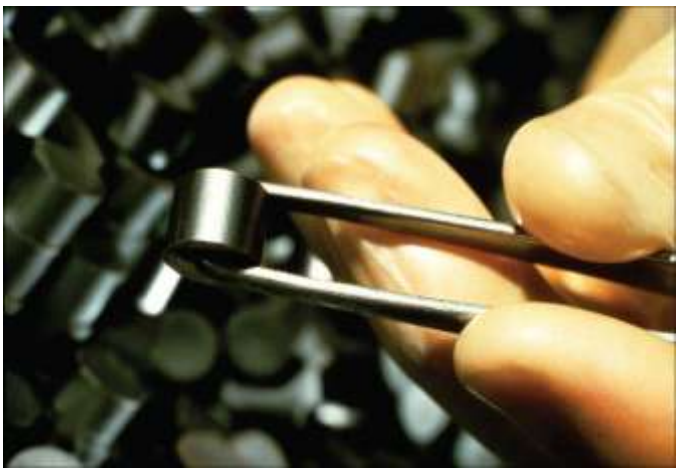

b) AGR's 4%-enriched UO_2 fuel pellet

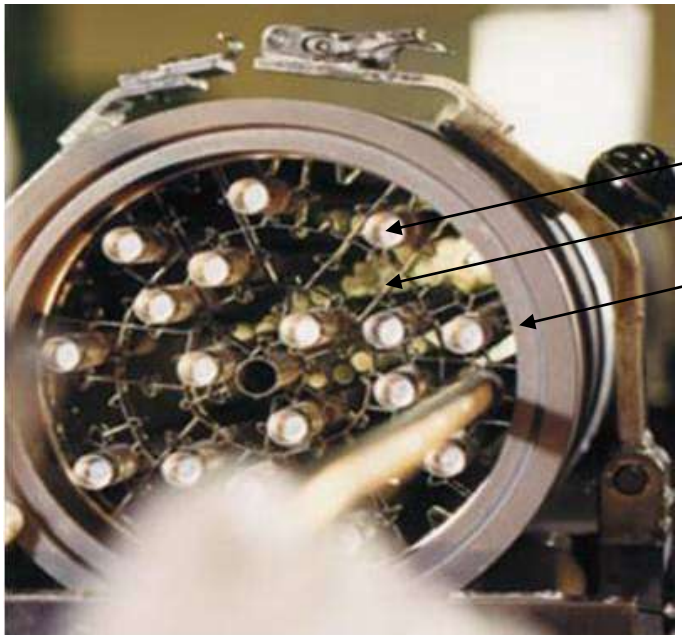

c) AGR fuel element

Figure 6 – Advanced gas-cooled reactor (AGR) fuel cladding (a), oxide fuel pellets (b) and fuel element (c). Figures adapted from Westinghouse Electric Company Brochure [10]

The fuel cladding is not only subjected to the internal stresses that arise from fuel pellet swelling, but also, directly, to a flux of thermal neutrons of ~10^{12} neutrons/m^2 [11] and an axial temperature variation between 400°C (bottom of stringer) to as high as 800°C (mid-stringer) in a circulation of CO_2-coolant at a pressure of 45.2 bar [12]. In broad terms, exposure to these conditions adversely affects the fuel cladding including causing degradation in mechanical performance (e.g., helium embrittlement), degradation in thermal properties (e.g., formation of gas bubbles which disrupt the heat transfer), dimensional changes (e.g., creep and thermal expansion due to radiation damage), and corrosion susceptibility (e.g., intergranular corrosion caused by grain boundary chromium depletion).

Parallel to the thesis' objectives this literature review focuses on the factors which influence the corrosion susceptibility of fuel cladding. Section 2.2 examines the metallurgical basis of the fuel cladding specific to the AGRs. Specifically, the formation of the primary austenitic microstructure, its grain boundaries and the niobium-based secondary phases in the cladding are elucidated, since one of the causes of corrosion is believed to be the presence and size of the secondary phases, for instance around manganese-sulphide inclusions [13-15]. Section 2.3 examines the relation between the fuel cladding and the individual components surrounded by it, i.e., the nuclear fuels, coolant and moderator, that may lead to corrosion susceptible conditions. In respect to the pellet-clad interactions and regions of stress concentration along the length of the cladding previously mentioned, the CO_2 oxidation and temperature cycling of the cladding results in surface inhomogeneities that may become potential corrosion sites [16, 17]. Section 2.4 reviews the direct effects of radiation on the cladding. It has been established that phenomena such as grain boundary chromium depletion [18, 19] and the hydrolysis of water by α, β, and γ emissions [11] are correlated to corrosion susceptibility. Lastly, section 2.5 reviews the manifestation, mechanisms and environmental factors that pertain to the wet storage of the spent AGR fuel cladding.

To summarise and as a guiding post Figure 7 illustrates an overview of the critical factors that affect the AGR fuel cladding corrosion which is discussed in the literature review.

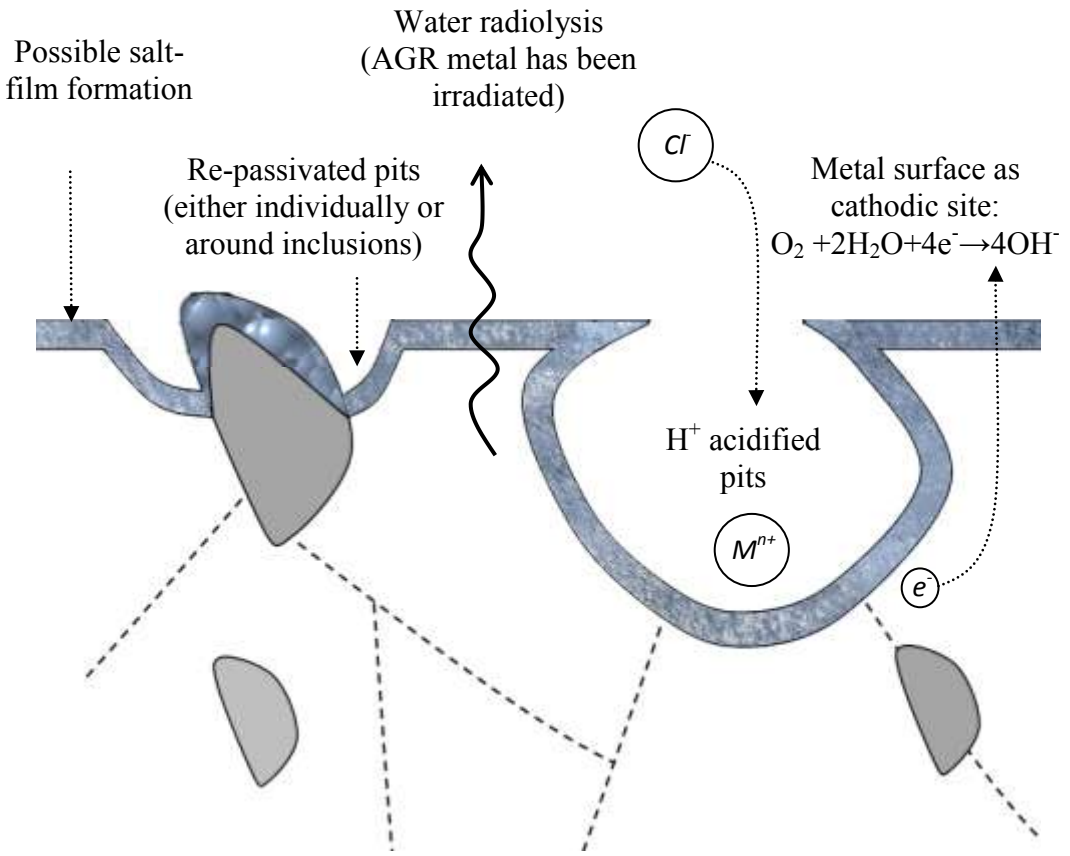

Legend:

- Formation of secondary phases in cladding metal
- Grain boundaries between austenite grains, potentially chromium depleted.
- Salt film formation
- Cl^- Chloride from the environment in the cooling ponds
- M^{n+} Dissolved metal ion from the solid. May exist as intermediate complexes
- e^- Transfer of electrons to cathodic sites, usually at the metal surface where O_2 is available
- Water radiolysis because the AGR metal has been irradiated

Figure 7 – Metal cross-section illustration of critical factors affecting AGR fuel cladding corrosion

2.2 *Metallurgical Properties of AGR Fuel Cladding*

The physical properties of the AGR fuel cladding, austenitic stainless steel with a nominal alloy composition of 20%wt Cr and 25%wt Ni stabilised with 0.7%wt Nb, are summarised in Table 1 (data adapted from Waddington and Jones [20]). The cladding possesses a melting temperature of about 1390°C, a relatively high value compared to, for example, zinc alloys that fully melt at 477°C [21]. Its density of 8.0 Mgm^{-3} is close to that of iron (7.87 Mgm^{-3}). The specific heat of 628 J/kg.K is a relatively low value compared to, for example, quartz (SiO_2) which has a high specific heat capacity of 1000 J/kg.K [22], which indicates that the fission heat from the fuel pellets can be more efficiently extracted through the fuel cladding into the circulating CO_2 coolant. The thermal expansion of the cladding given by the equation and constants in row 6 of Table 1 is a measure of thermal strain that the metal potentially develops due to the cladding's expansion and contraction over the

Table 1 – Physical properties of AGR fuel cladding [20]

Properties	Values	
Typical alloy composition (wt%)	chromium (Cr) – 20.12 nickel (Ni) – 25 niobium (Nb) – 0.7 silicon (Si) – 0.57 manganese (Mn) – 0.62	carbon (C) – 0.049 sulphur (S) – 0.004 tantalum (Ta) – <0.05 phosphorus (P) – 0.006 nitrogen (N) – 0.016 iron (Fe) – balance
Melting temperature	1390°C (solidus). 1460°C (liquidus)	
Atomic volume	$1.15 \times 10^{-29}\ m^3$	
Density	8.01 Mgm^{-3} (25°C)	
Specific heat	628 J/kg.K (750°C)	
Thermal expansion	$L_T=L_0(1+\alpha T+\beta T^2)$, $\alpha=16.0 \times 10^{-6}$, $\beta=2.97 \times 10^{-9}$	
Thermal conductivity	20.09 W/m.K (500°C), 24.28 W/m.K (750°C)	
Emissivity	0.4 (surface oxidized in CO_2)	
Thermal Neutron Absorption Cross-Sections	3.22 barns (averaged across all alloying elements)	

course of temperature cycling on power adjustments in the reactor core. At an arbitrary temperature of 600°C the cladding is predicted to elongate about 1.5% from its original length. Compared to zinc alloys, for example, which at 600°C elongates by about 6% of its original length [23], the cladding metal possesses better thermal stability. Its thermal conductivity value of about 25 W/m.K, intermediate between high thermal conductivity materials such as aluminium (247 W/m.K) and copper (398 W/m.K) and insulator materials such as quartz (3 W/m.K) [21], adequately transfers the fission heat from the fuel pellet to the CO_2 coolant. The cladding has an average *thermal neutron absorption cross section* (σ_a) of about 3.22 barns. The term *cross section* is synonymous with *probability,* i.e. the probability of a thermal neutron being absorbed by the cladding, if not otherwise fissioned (σ_f) or scattered (σ_s). In general, elements that possess low σ_a values are desirable as construction materials for nuclear applications because neutron losses due to absorption by the surrounding system are minimised. The element zirconium, for instance, possesses one of the lowest σ_a values of only 0.18 barns hence it is an important element in structural materials for water-cooled reactors when water itself is a neutron absorber [21]. Table 2 is a compilation of physical properties of several common metal elements for nuclear application which compares the σ_a values of the AGR fuel cladding's individual alloying elements.

The cladding contains about 20%wt Cr and 25%wt Ni which is relatively high compared to other stainless steels. The alloy composition is intended to primarily produce austenitic grains which are desired to retain its physical and mechanical properties up to temperatures of approximately 1000 °C [21]. Figure 8 shows the Schaffler diagram which estimates the metallurgical phases present in stainless steels based on their chromium and nickel contents. It is shown that the austenite microstructure is promoted by nickel (e.g., no nickel no austenite), also known as an austenite stabiliser, in contrast to chromium which promotes the ferrite phase. The austenite grains are a solid solution of nickel and chromium solute atoms that are homogeneously and randomly distributed among the solvent atoms iron in the face-centred cubic lattice (γ) without clusters of separate phases.

Table 2 – Physical properties of important alloying elements for nuclear applications [23]

Element	Al	Be	Cr	Cu	Fe	Mg	Mo	Ni	Nb	Ta	Ti	Te	Zr
Density, (g/m^3)	2.67	1.85	7.19	8.96	7.87	1.74	10.22	8.90	8.57	16.60	4.51	19.30	6.50
Atomic Weight	26.98	9.01	52.00	63.55	55.85	24.31	95.94	58.69	92.91	180.9	47.87	183.8	91.92
Thermal Neutron Absorption Cross-Section (barns)	0.23	0.01	2.90	3.70	2.50	0.06	2.50	4.60	1.10	21.00	5.60	19.00	0.18
Thermal Neutron Scattering Cross-Section (barns)	1.50	7.63	3.49	8.03	11.62	3.71	5.71	18.50	6.26	6.01	4.35	4.60	6.46
Melting Temp. (°C)	655	-	-	1080	1535	-	2610	1315	2470	2995	1683	3410	1852
Thermal Conductivity @25°C (W/m.K)	247	210	67	398	80.4	155	142	82.9	52.3	54.4	11.4	160	21.1
Tensile Strength (MPa)	50	400	83	209	265	90	600	317	585	-	-	150	-

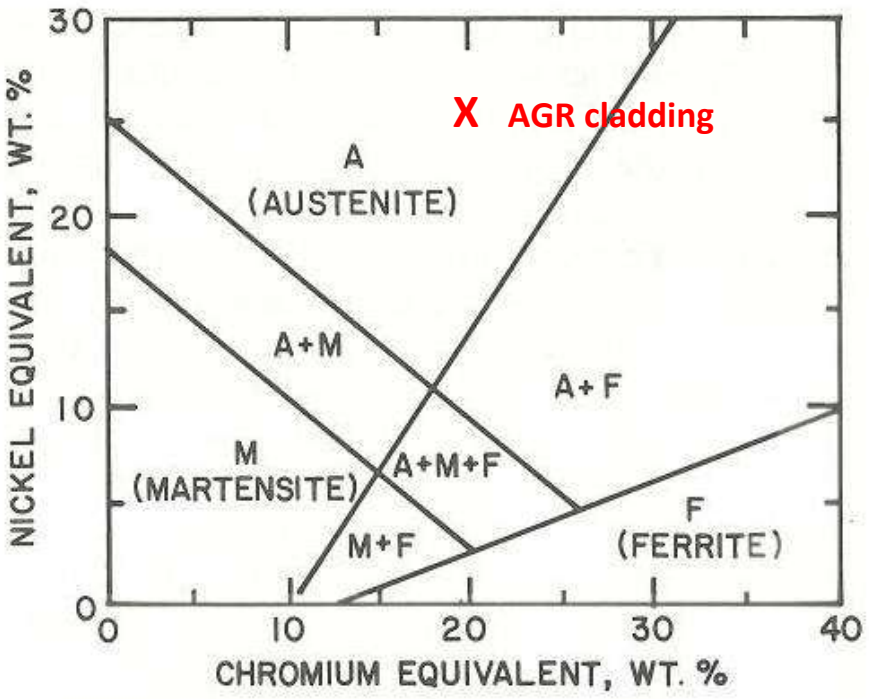

Figure 8 – Schaffler diagram for microstructure prediction in solid solution based on nickel and chromium concentrations, adapted from Sedriks [53]

The cladding contains 20 %wt Cr which gives the metal its remarkable corrosion and oxidation resistance. Generally found in iron that is alloyed above 12 %wt Cr, these qualities are attributed to the spontaneous formation of a ~2 – 3nm thick chromium-oxide film on exposure to the atmosphere. Also referred to as the passive film these protective scales formed on the outermost layer of the cladding's surface prevent oxidation of the structural alloy beneath it. An Ellingham diagram (Figure 9) shows that the potential for chromium-oxide (Cr_2O_3) formation is higher than that of the iron oxide (FeO) indicative of its lower ΔG or Gibbs Free Energy value [24]. In essence a process or formation that has a comparatively lower ΔG value indicates that it is more likely to occur. With regards to the passive film one of the most challenging issues in corrosion science is in elucidating the mechanisms and conditions that lead to its breakdown which subsequently results in iron dissolution.

Niobium, as a minor alloying element of about 0.7 %wt, serves two roles in the cladding: first 'stabilising' its austenitic microstructure against a condition called

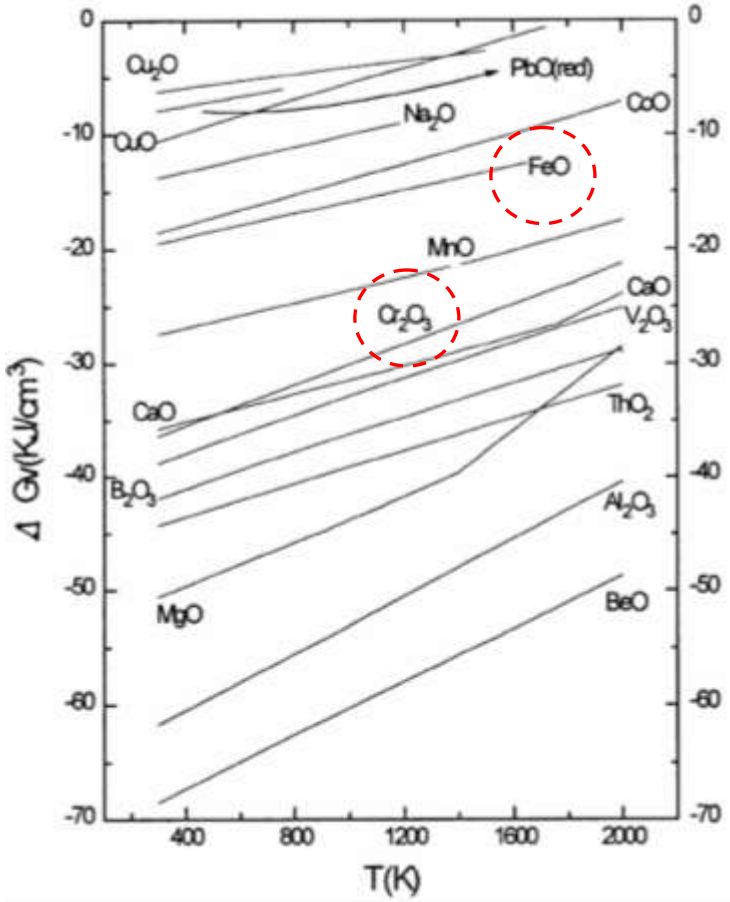

Figure 9 – Ellingham diagram for oxidation potential by metallic elements, adapted from He *et al.* [24]

thermal sensitisation and second, improving the creep and structural strength of the fuel cladding through precipitation hardening.

Thermal sensitisation is characterised by the precipitation of chromium by the free carbon atoms in the metal's matrix to form chromium carbides ($M_{23}C_6$, M denotes chromium predominantly but also some iron) which primarily occurs along the grain boundaries at elevated temperatures between 400 to 800°C [25]. Figure 10a shows that chromium from the grain boundary is precipitated as $M_{23}C_6$, raising intergranular corrosion concerns. From the steelmaking perspective, 'stabilising' the metal refers to trapping the free carbon atoms by stabilising elements such as niobium, tantalum and titanium [23]. Note that free carbon always exists in the lattices of bulk iron matrices, about 2 to 4wt% in carbon steel [26]. Even though the carbon concentration in the cladding has been specifically limited to about 0.049 %wt (composition indicated in Table 1), Evans *et al.* [16, 27] and Millward *et*

al. [17, 27, 28] have shown that high temperature oxidation by CO_2 coolant may introduce additional carbon to the cladding. In the event of increased carbon contents the potential for thermal sensitisation in the cladding's austenite lattice is also increased. Figure 10b shows that at carbon contents above 0.03 %wt and temperatures below 700°C the carbon atoms have limited solubility in the austenite face-centred cubic lattice and likely precipitate out as $M_{23}C_6$. Among the potential stabilising elements are niobium, titanium and tantalum which trap carbon as NbC, TiC, and TaC. These may thus form at the expense of $Cr_{23}C_6$ as indicated by their lower ΔG values shown in the Ellingham diagram in Figure 11. However,

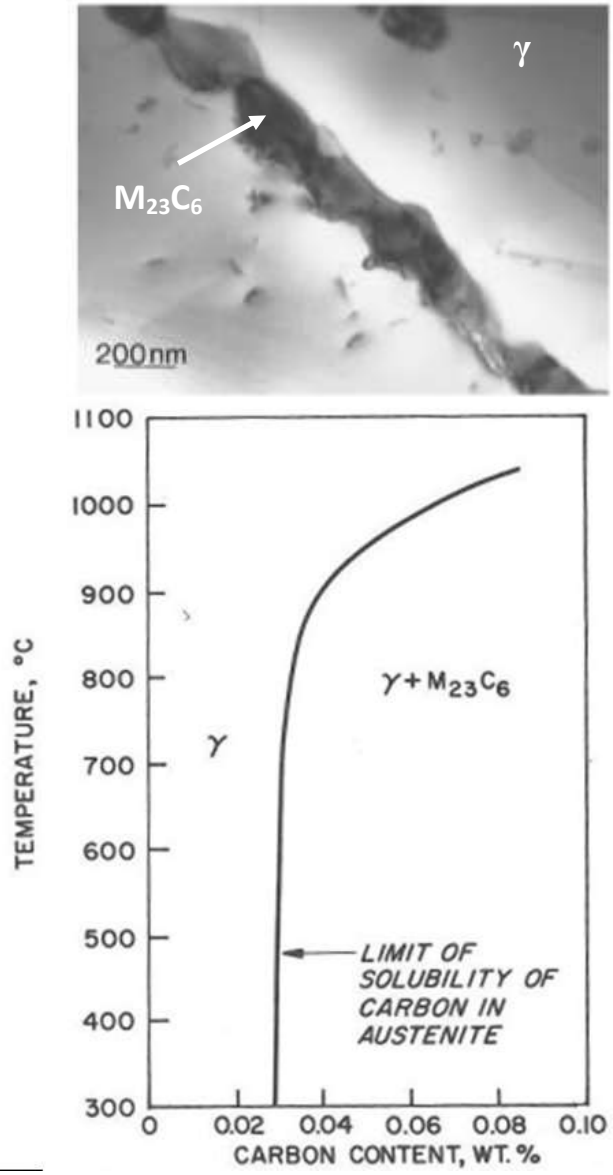

a) precipitation of chromium carbide $M_{23}C_6$, adapted from Sourmail [25]

b) solubility of carbon in austenite, adapted from Sedriks [53]

Figure 10 – Limit of solubility of carbon in austenite and precipitation of chromium carbide at the grain boundaries

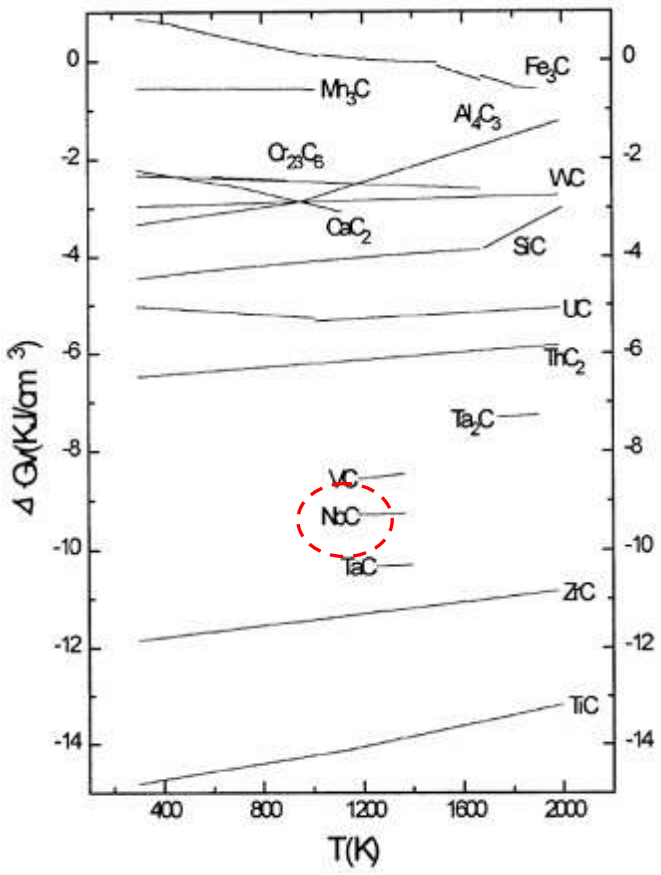

Figure 11 – Ellingham diagram for carbide formation potential by metallic elements, adapted from He *et. al.* [24]

niobium is invariably used in nuclear applications due to its low thermal neutron capture cross-section (1.1 barns) as compared to titanium and tantalum which have higher cross-sections (5.6 and 21.0 respectively, Table 2). Addition of niobium equal to 10 times the carbon content of the steel is deemed necessary to prevent $M_{23}C_6$ precipitation [23]. On a separate but related note, grain boundary chromium depletion may also be caused by the radiation-induced segregation phenomenon which is reviewed in section 2.4.

Creep, on the other hand, is the tendency of a solid material to become permanently deformed after long periods of exposure to stress levels that are below the yield strength of the material. Creep strength of a solid material is improved by a phenomena and steel making practice called precipitation hardening. Precipitation hardening is 'the hardening in metals caused by the precipitation of a constituent from a super-saturated solid solution [21]. Figure 12 shows a micrograph which

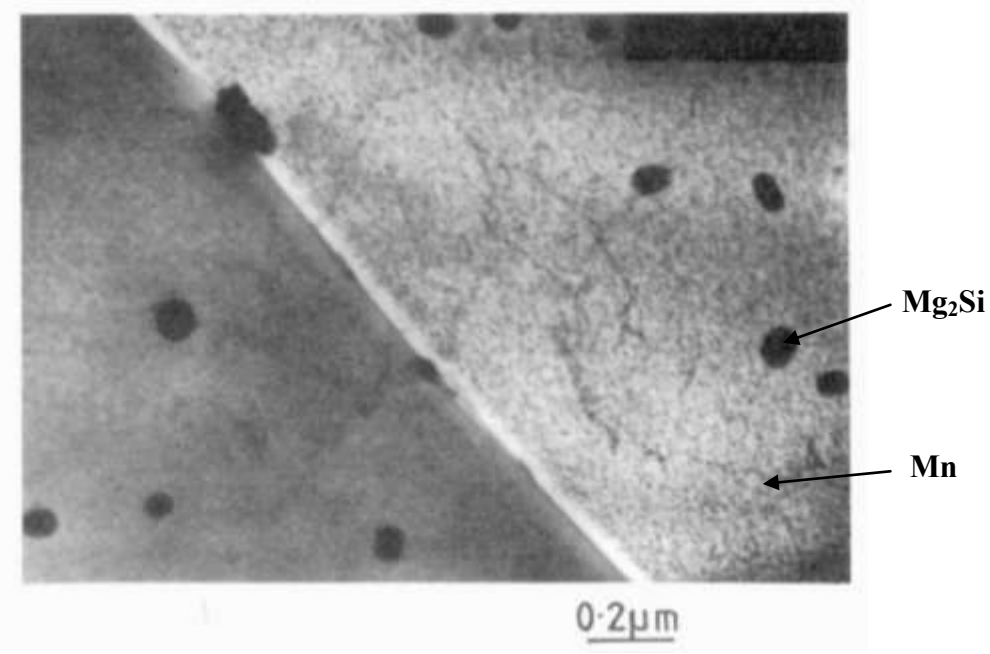

Figure 12 – Dispersion of fine Mg_2Si secondary phases in a precipitation-hardened Mn-metal, adapted from Martin [29]

illustrates precipitation hardening by the finely dispersed constituent Mg_2Si (a secondary phase) in the manganese-matrix. These constituents gives the metal remarkable creep strengthening by trapping the dislocations and voids in its lattice [29].

The role of niobium in the precipitation strengthening of the steel can be assimilated from the ideas of Merica and Merica *et al.* [30, 31]. Merica, one of the pioneering investigators of the phenomenon, first described precipitation strengthening in Duralumin, an alloy of aluminium containing about 5 %wt of copper and magnesium that is precipitation-hardened by $CuAl_2$. Of relevance to the AGR fuel cladding, the solute atoms Nb can absorb into the atomic lattice, i.e., solid solution, of the austenite. Its solubility, however, varies considerably with temperature. At temperatures near to its melting point of 1390°C which occurs in practical steelmaking the austenite solid solution possesses the highest solubility where most of the Nb is absorbed in its lattice. At low temperatures, however, the solubility of Nb in the metal lattice is decreased markedly. Therefore, upon drastic cooling or quenching, the excess Nb is precipitated as secondary phases, usually NbC carbide, in the supersaturated solid solution. It is the dispersion of these NbC

carbides which give the initial structural strength and creep resistance of the steel. To enhancement these initial properties, the precipitation hardening technique specifically involves a final heat aging step at intermediate temperature which is intended to optimise the size and distribution of the NbC carbides that further improves its creep and structural strength. Table 3 lists the types of secondary phases of about 0.5 μm that are randomly distributed in the AGR fuel cladding lattice which has a uniform grain size of ~25 μm [20].

Table 3 – Precipitate formation in AGR fuel cladding

1. Processing route for AGR Fuel Cladding [20]:

Stage	Process
1	Anneal thick-walled tube for 5 min at 1025°C
2	Cold draw ~25%
3	Machine ribs on tube
4	Load pellets and weld on end caps
5	Hydraulically pressurise onto the fuel
6	Anneal 930°C for 1h

2. Types of Precipitate Formation [20]:

Secondary Phases	Crystal State	Lattice Parameter, nm	
		a	c
Nb(C,N)	Cubic	a=0.443	-
$M_6(C,N)$	Cubic	a=1.125	-
$M_{23}(C,N)_6$	Cubic	a=1.064	-
Fe_2Nb	Hex	a=0.483	c=0.788
Fe-Cr (σ-phase)	Hex	a=0.879	c=0.454
$Cr_2Nb_2(C,N)_2$ (Z-phase)	Hex	a=0.303	c=0.739

*M indicates alloying elements other than Fe, e.g. Ni or Cr

2.3 Components Adjacet AGR Fuel Cladding: Fuels, Coolant and Moderator

This section examines the relations between the AGR fuel cladding and its adjacent components which include the 4% enriched uranium dioxide (UO_2) nuclear fuel pellets, carbon dioxide (CO_2) coolant fluid and the graphite moderator. The cladding's interactions with the latter impacts its metallurgical state and in turn its corrosion susceptibility. In broad terms, nuclear fuels are responsible for sustaining the fission chain reactions whereas the cladding retains the FPs and other radioactive species so preventing their escape to the environment. The moderator governs the type of fission physics occurring whereas the coolant absorbs and transports its heat to the power generation systems. A review of these individual components adjacent to the AGR fuel cladding highlights the underlying causes of issues such as pellet-clad interactions and oxidation of the cladding by CO_2 which impacts corrosion. In wider terms, these issues are not only confronted in AGRs but also in the majority of nuclear reactors operating today.

From the developmental perspective AGRs are second generation reactor amongst the others that Britain has explored, as the compilation in Table 4 shows. It is an improvement from its predecessor, the first generation MAGNOX reactor [32]. Both are CO_2-cooled and graphite moderated. One of their major differences lies in the nuclear fuels and fuel cladding that they employ; the AGR uses a 4% enriched UO_2 fuels in an austenitic stainless steel cladding whereas the MAGNOX uses natural, un-enriched uranium metal fuels that are clad in a non-oxidizing magnesium alloy as depicted in Figure 13. The first MAGNOX reactor, Calder Hall station built in Sellafield in 1956, is derived from the research prototype PIPPA (Pressurized Pile for Producing Power and Plutonium) in Harwell that also produces plutonium [33]. This notion traces to the historical Windscale Plutonium Pile which solely produces plutonium for military uses and not electricity. All MAGNOXs' subsequent to Calder Hall (240 MWe) are optimised for electricity production until the last unit, Wylfa, whose power output approached ~800 MWe. The subsequent generations of AGRs achieve power output of up to ~1000 MWe and are scheduled to continue around year 2030 after which they are subjected to decommissioning. The future third generation reactors are the highly-optimised version of the second generations (mostly PWRs) based on operating experience

Table 4 – Nuclear power development in the United Kingdom

Reactor Type	Reactor Name	Key Features
Plutonium Pile	GLEEP (research) BEPO (research) Windscale	Plutonium-producing only. No conversion to electricity.
Fast Breeder Reactor (FBR)	ZEPHYR (research) ZEUS (research) DMTR (research) ZEBRA (research) Dounreay (research) Dounreay PFR (prototype)	Research only. One of the inherent problems is corrosive coolant. French PHENIX and SUPERPHENIX were commercially operated.
High Temperature AGR (HTAGR)	Dragon (research)	Decommissioned.
Steam Generating Heavy Water Reactor (SGHWR)	Winfrith Heath	Successful operation. Decommissioned.
Magnox	PIPPA (research) Calder Hall Chapelcross Berkeley Bradwell Hunterston A Hinkley Pt A Trawsfynydd Dungeness A Sizewell A Oldbury Wylfa	First generation reactors. First built: Calder Hall (1956) Last built: Wylfa (1971) Power output: ~500 MWe
Advanced Gas-Cooled Reactor (AGR)	Windscale (prototype) Hinkley Pt B Hunterston B Dungeness B Heysham 1 Hartlepool Torness Heysham 2	Second generation reactors. First built: Hinkley Pt B (1976) Last built: Heysham 2 (1988) Power output: ~1000 MWe
Pressurised Water Reactor (PWR)	LEO (research) Sizewell B	American design. UK possesses one commercial unit.
Fusion Research	ZETA (research) JET (research)	Fusion reactor.

a) MAGNOX fuel: natural uranium metal 'billet', adapted from BNFL Oxide Fuel Brochure [32]

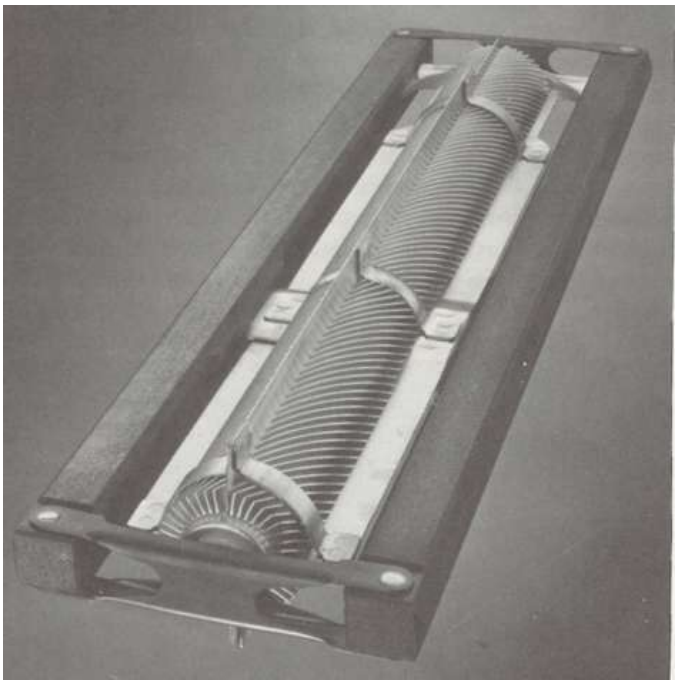

b) MAGNOX cladding: magnesium alloy, adapted from Frost [37]

Figure 13 – MAGNOX uranium metal fuel and magnesium alloy fuel cladding

whereas the fourth generations reactors (so called Gen-IV) are the commercialisation of Fast Breeder Reactors (FBR) and others [34].

2.3.1 Fuel Forms

A nuclear reactor essentially taps the heat energy that is amassed from the fission chain reactions of the fissile isotopes. There are three primary fissile isotopes, that is: uranium-233 (U-233), uranium-235 (U-235) and plutonium-239 (Pu-239) that spontaneously fission on neutron absorption. Only U-235 occurs naturally in a small abundance of 0.7%wt as found in the ore and the rest if natural uranium is U-238. U-233 and Pu-239 are artificial fissile isotopes that are derived from the transmutation of thorium-232 (Th-232) and U-238 respectively. The fissile isotopes, either individually or in combination and at particular enrichment level, are

fabricated into suitable fuel matrices or forms, commonly: metals, ceramics, and ceramic-metal fuels (dispersion of ceramic fuels in metal matrices).

The AGR employs uranium oxide fuels, the ceramics category, in which the fissile U-235 content is enriched to 4 %wt by absolute atom fraction of U. Oxide fuel pellets are produced through the Integrated Dry Route (IDR) process at Springfields situated in the north of England by mixing the enriched-UO_2 powder with binder and lubricant materials, granulating to form free-flowing particles, compacting in an automatic press, heating to remove the binder and lubricant, sintering in a controlled atmosphere, and grinding to a final diameter [32]. In general, a combination of UO_2 and plutonium-oxide (PuO_2) powders may be sintered together such as in MOX fuel for LWR [34]. In addition, the enrichment level can be acquired at any purity, up to 99%. For instance FBRs employ PuO_2 fuels in which Pu-239 is enriched up to 20% [35].

Oxide fuels are generally sought for their radiation stability. They do not swell as much as metal fuels, so posing reduced risk of fuel rupture. As ceramic fuels are manufactured by sintering techniques their porosity can be tailored to accommodate the fission gases. The unit cell of UO_2 has a face-centred cubic packing of the large U^{4+} cations in a CaF_2 type structure (space group Fm3m); this leaves space at the cell centre that can accommodate FPs so contributing to its radiation stability [21, 36]. Drawbacks are, however, its low thermal conductivity and fission cross-section (σ_f) compared to other fuel types. Table 5 compares the

Table 5 – Physical properties of metals and oxide fuels [37]

Property	**U-Metal**[†]	**UO_2**	**UC**	**UN**
Density, g/cm^3	19.12	10.96	13.61	14.32
Melting Temp., °C	1130	2865	2507	2762
Thermal Conductivity, W/m.K	350 (400°C)	30 (1000°C)	216 (1000°C)	200 (750°C)
Thermal neutron fission cross-section (σ_f), barns	4.18	0.102	0.137	0.143

[†]Allotropic metal: orthorhombic (<663 °C), tetragonal (663-770 °C) and body-centred cubic (770-1130 °C).

physical properties of uranium metal and ceramic fuels and indicates that the metal's thermal conductivity and σ_f of 350 W/m.K and 4.18 barns respectively are considerably higher than the ceramic values. Other variations of ceramic fuels that have more desirable range of physical properties for nuclear application such as the uranium carbides (UC) and uranium nitrides (UN) have also been developed [37].

Uranium metal fuels, on the other hand, were adopted in early reactors for their workability, high thermal conductivity, reprocessability and because no fuel enrichment is necessary for sustaining a chain reaction. Reprocessability refers to the use of electrochemical techniques to separate and concentrate the spent uranium, plutonium and minor actinides (MAs), benefitting waste management and nuclear proliferation aspects [33]. Contrary to ceramic fuels, however, metal fuels have low deformation stability which is associated with its allotropic nature. The metal assumes three crystalline forms: orthorhombic α-U which is stable up to 663 °C, tetragonal β-U up to 770 °C and body-centred-cubic γ-U up to its melting temperature of 1130 °C. This suggests that the reactor operating temperatures, thus power output, must be maintained below 663°C within the range of the α-U phase thereby avoiding the dimensional changes associated with phase transitions. In addition, thermal cycling has been shown to cause anisotropic irradiation growth under irradiation, i.e., the metal crystal elongates in the *a*-direction and shrinks in the *c*-direction, where the metallic fuel can exhibit substantial growth to more than 60% of its original length [36]. On a related note, the fission gasses which are insoluble in uranium metal also contribute to the dimensional growth in metallic fuels.

Another potentially viable fuel form is a composite of ceramic and metal or materials that are inert to irradiation effects. In essence, the fuel consists of fuel-bearing ceramic particles that are dispersed in a stainless steel or inert matrix. Figure 14a adopted from Frost [37] shows the cross-section of a typical UO_2-steel composite fuels. The ceramic fuel particles are tailored with fine internal structures which contain adequate porosity to account for fission gas accommodation. The steel matrix surrounds the hot ceramic fuel particles and conducts its heat. As the fuel particles are isolated a substantial volume of the steel matrix remains unchanged and undamaged by the FPs thus minimising fuel swelling. The challenges of composite fuels are largely maximising the fuel fraction and achieve uniform fuel dispersion.

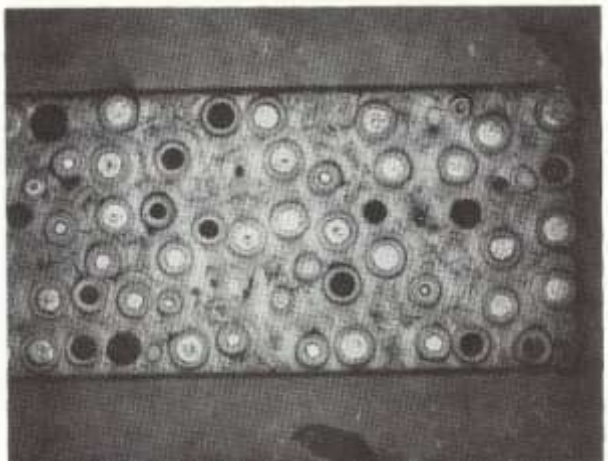

a) Dispersion of ceramic fuel in metal matrices. Metal distance between ceramic fuel particles should ideally be greater than FPs recoil distance of ~10μm

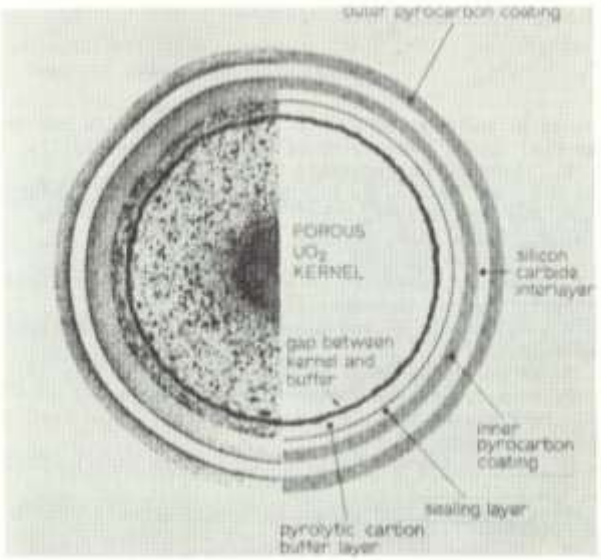

b) Internal structure of the ceramic fuel particles (~50 – 500μm diameter)

Figure 14 – Fuel bearing particles dispersed in metallic matrices, adapted from Frost [37]

2.3.2 Coolant

The circulation of coolant fluid in nuclear reactors is intended to absorb and transport the abundant heat generated within the nuclear fuel to the power generation system. In the fission reaction pathway U-235→Cs-144+Br-90+*n* for example, the fissile isotope U-235, fission fragments Cs-144 and Br-90 and prompt neutron *n* have atomic mass units (*u*) of 235.0439222*u*, 143.9320274*u*, 89.9306350*u* and 1.008664*u* respectively; the 0.1725958*u* mass differences from Einstein's mass-energy conservation equation $E=mc^2$ (c^2 taken as 931.502 MeV.u^{-1}) equates to a conserved heat energy (E) of roughly 168 MeV. Table 6 shows the average energy per-fission of several common fissile isotopes that accounts for all fission reaction

pathways [38]. Considering U-235 which have the latter value of 201.7±0.6 MeV, the criticality of one mole or 235 grams of this substance which contains an Avogadro number of fissile atoms theoretically yields about 10^{26} MeV or 4500 MWh of energy, equalling better than burning 10000 tons of coal [39]. This justifies nuclear electricity as a truly viable alternative amongst the basket of ways forward to meet both electricity demand and carbon targets.

The fission heat from the AGR's oxide fuels are extracted by a circulating CO_2-coolant at 45.2 bar pressure. The principal attractiveness of gas-cooling is the natural convection that it affords, i.e., warmer gas draws out from the core and cooler gas draws in by convection. For this reason gas-cooled reactors are inherently safer than water reactors in the advent of loss of coolant circulation due to pump damage or loss of power supply [33]. In addition, gas-cooled reactor cores are not as reactive as water-cooled reactors which need to account for the extra neutron absorption by the water. In the event of water cut-off, the water boils to steam which is 100 times less dense than water thus not absorbing neutrons but causing a surge of neutron flux that increases the core's temperature sufficiently for melting to occur. In the recent incident involving the Fukushima Daiichi nuclear power plants (NPP) in Japan, for example, the magnitude-9.0 earthquake on 11 March 2011 caused the cooling system to fail. At some point the falling water levels must have left the fuel exposed leading to the core meltdown. Apart from the water-cooled Sizewell B which is a PWR, all the reactors designed in the UK are gas-cooled.

Table 6 – Fission isotopes, energies and thermal fission cross-sections

Isotope	Energy (MeV/fission)	Thermal Neutron Fission Cross-section (barns)
Th-232	196.2 ± 1.1	-
U-233	199.0 ± 1.1	527
U-235	201.7 ± 0.6	584
U-238	208.5 ± 1.1	-
Pu-239	210.7 ± 1.2	746
Pu-241	213.8 ± 1.0	1025

The fuel cladding is constantly exposed to oxidation by the circulating CO_2 atmosphere in the reactor core. CO_2 has the advantage of not having a liquid-gas phase change under reactor operating or accident conditions. Millward *et al.* [17, 27, 28] show that CO_2 circulation can cause 'solid carbonaceous filaments with turbostatic packing' on the surface of the unirradiated 20Cr/25Ni/Nb metal on exposure to CO_2, CO and C_2H_4 gas mixtures at 550°C for various durations. Due to prolonged temperature cycling these scales may mechanically spall-off the cladding's surface. Commonly referred to as spallation, this condition is characterised by the surface scales rupture caused by the circulating coolant fluid turbulence, internal stresses from fuel pellet swelling and repeated temperature cycling which because of differences in contraction rates between the metal cladding and the scale. The spalled-scales become a dust source in the circulating coolant fluid which may mechanically impact on the cladding surface. In fact, spallation results in severe surface irregularities where pits up to 40μm deep (about 10% of the 0.38mm wall thickness) have been measured [20, 40] and they may potentially become sites for accommodation of corrosive agents for corrosion initiation.

This section concludes with Table 7 which compares the physical properties of the CO_2-coolant with several other coolant fluid candidates that are considered for the new nuclear build initiatives [41]. In essence, future reactors are designed to achieve high burn-up and temperatures in order to maximise electricity production. For these purposes, the physical properties demanded of the coolant fluid are high density, thermal conductivity and specific heat. The sodium-fluid of composition 30NaCl/20KCl/50$MgCl_2$ and lead (Pb) mixture, for example, have boiling temperatures of 1737 °C and 2500 °C respectively which protects the reactor core from meltdown and stores large amounts of decay heat during transients. In particular, the lead-coolant's density that approaches 10000 $kg.m^{-3}$ is remarkable. The challenges that are faced with these advanced coolant fluids, however, include their corrosive behaviour that affects the piping system and meeting the high pumping power requirements to sustain the required coolant flow rates [41]. The historical Windscale Plutonium Pile which was constructed to manufacture weapons-grade Pu simply utilised air as its coolant (Figure 15).

a) Air cooled chimneys of the Windscale Plutonium Pile

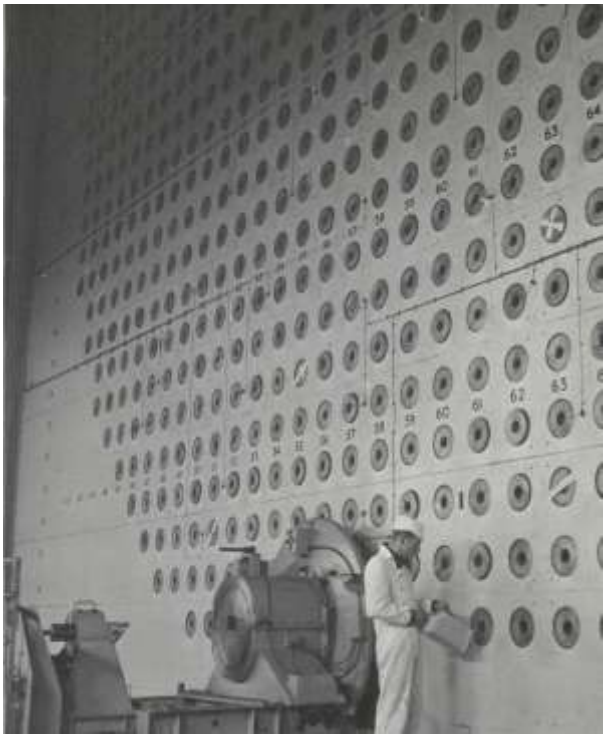

b) Charge Face where uranium fuel 'cartridges' are inserted to undertake transmutation U-238+n→Pu-239

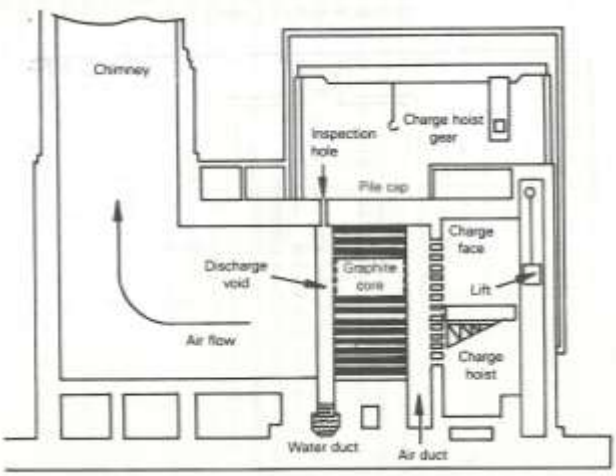

c) A section through the pile showing air cooling

Figure 15 – Air-cooled Windscale Plutonium Pile, adapted from Pocock [33]

Table 7 – Comparison of coolant fluid for nuclear reactors [41]

Properties	Lead (Pb)	Sodium (Na)	Sodium (30NaCl:20KCl:50$MgCl_2$)	CO_2 (Sat'd)	Water
Boiling Temp. (°C)	1737.0	892.0	2500.0	-78.0	100.0
Melting Temp. (°C)	327.4	97.8	396.0	-58.0	0.0
Density@700°C (kg/m^3)	10242	780	1715	104	1000
Thermal Conductivity (W/m.K) @750°C	17.700	59.100	0.390	0.072	0.600
Specific Heat (J/Kg.K)	147.0	1276.0	1004.0	1267.9	4.2

2.3.3 Neutron Moderation

Nuclear fission reactors are classified into two kinds based on the neutron energy spectrum that they are designed to operate with – either fast or thermal. The AGR is a thermal reactor whose characteristics of radiation damage and potential for carbide formation, hence their corrosion behaviour during latter wet storage, are fundamentally different from the fast reactors. A thermal reactor employs a neutron moderator to attenuate the prompt neutron (interchangeably referred to as fast or fission neutrons) kinetic energies of approximately 1.0×10^6 eV to about 0.025 eV where the 'slowed' neutrons are in thermal equilibrium with the atoms of the moderator material [38]. The thermal neutron energy of 0.025 eV is derived from the equation $v = \sqrt{\frac{2k_BT}{m}}$ which parameters neutron mass $m = 1.675 \times 10^{-27}$ kg, Boltzmann's constant $k_B = 8.617 \times 10^{-5}$ eV.K^{-1} and room temperature $T = 300$°K yields the most probable neutron velocity (v) of 2200 ms^{-1}; at this velocity the thermal neutron energy (E) from the equation $E=0.5mv^2$ computes as 0.025 eV. Figure 16 shows that the fission cross-section (σ_f) of U-235 for the thermal neutrons is 584.4 barns which is much higher than that of the fast neutrons at 1.136 barns [42].

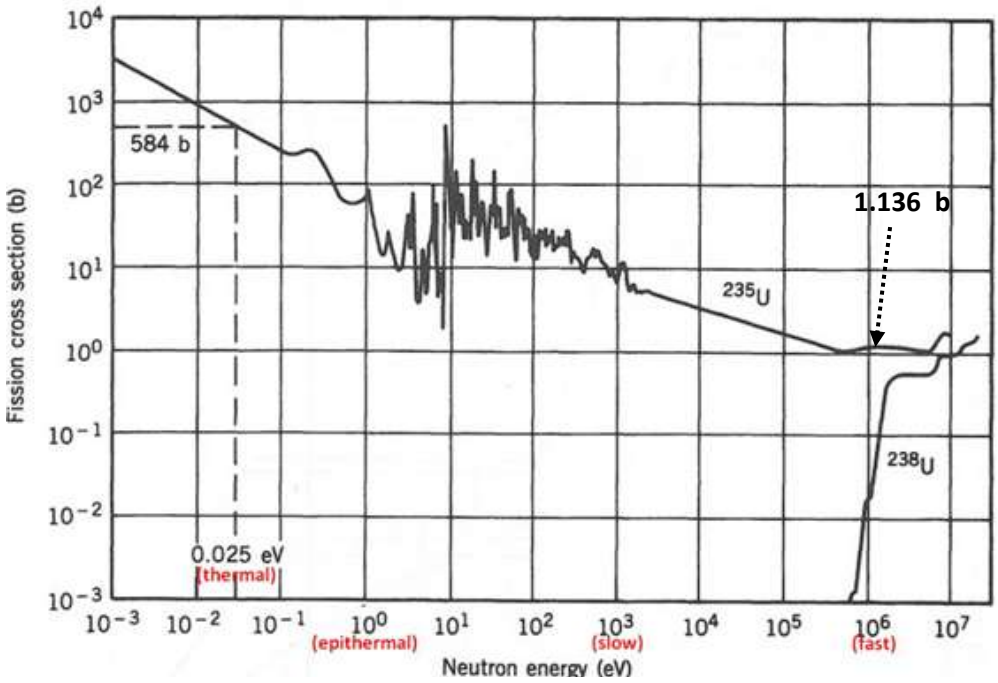

Figure 16 – Variation of fission cross-section over neutron energy spectrum, adapted from Hill [39]

At the atomic scale, the low fission cross-section of the fast neutrons, i.e., 1.136 barns, is due to the *elastic scattering* phenomenon; the fast neutron that encounters a U-235 molecule simply bounces off its target due to its high incident energy, with only a small chance of colliding with high impact if the target lies directly in its path. In contrast, the slowed neutrons have a relatively high fission cross-section, i.e., 584.4 barns, because they are likely to participate in the *inelastic scattering* phenomenon; the imparting neutron binds to the target fissile material U-235 thus inducing fission reactions.

AGRs employ graphite as the moderator, amongst other materials which include water, heavywater, and beryllium. Table 8 summarises their physical properties. Good moderating media should have small neutron absorption cross-section and high scattering cross-section [36]. The small neutron absorption cross section dictates the low neutron losses through absorption by the system whereas the high scattering cross section promotes 'slowing down' as each neutron collision with the moderator materials absorbs a proportion of its energy until a thermal equilibrium is reached. Beryllium has good slowing-down ability indicated by its scattering cross-section of 11.86 barns but is less used because of its toxicity, brittleness and difficulty in processing [36]. Water has one of the largest scattering cross-sections of 41.01 barns but, paradoxically, has the highest absorption cross-sections of 0.664 barns which means the neutrons scattered are absorbed.

Table 8 – Physical properties of neutron-moderating materials [36]

Moderator	**Be (metal)**	**BeO (oxide)**	**Graphite**	**H_2O**	**D_2O**
Density (g/m^3)	1.85	2.8	1.6	1.00	1.10
Atomic Weight	9.01	25.01	12.01	18.02	20.03
Thermal Neutron Absorption Cross Section, (barns)	0.01	0.01	0.0045	0.664	0.00114
Thermal Neutron Scattering Cross Section, (barns)	7.63	11.86	5.551	41.01	3.82
Melting Temperature (°C)	1282	2550	3650	0	0

On a related note, nuclear graphite poses a problem due to its Wigner energy. Graphite, if operated below a certain temperature, exhibits a substantial increase in the potential energy in its lattice structure due to the displacement of graphitic atoms by the bombarding neutrons. This potential energy, if unreleased, leads to remarkable dimensional distortion but it can simply be annealed-out by heating the graphite at a higher temperature. The Windscale incident in 1957 was a fire caused by the unexpectedly large un-released Wigner stored in its graphite core whilst performing annealing operation to remove the Wigner energy [33].

2.4 Effects of Radiation Fields on AGR Fuel Cladding Corrosion

The radiation field adversely impacts on the corrosion performance of the AGR fuel cladding in several ways. In addition to the stresses from fuel pellet swelling and thermal cycling in CO_2 oxidation there are two further ways in which the radiation fields directly impact fuel cladding corrosion: grain boundary chromium depletion and the radiolysis of water. Grain boundary chromium depletion is a condition characterised by the segregation of alloying elements from the grain boundaries due to radiation-induced segregation phenomena [18, 19]. A chromium-depleted site loses the ability to form the protective chromium-oxide scales at the particular grain boundary which then becomes susceptible to attack by corrosive agents such as chloride. Radiolysis of water, on the other hand, is caused by emissions of α, β, and γ radiation by the 'hot' fuel pellets which hydrolyses the layer of water immediately adjacent to the cladding's surface [11, 43]. The enhanced water radiolysis dissociation products, for example H^+ and OH^-, result in acidic or alkaline conditions depending on the type of metal and electrolyte solution which accelerates corrosion processes. This section reviews both phenomena.

2.4.1 Grain Boundary Chromium Depletion

Grain boundary chromium depletion has been experimentally observed in cladding materials that are retrieved from the spent fuels. Norris and *et al.* [18] measured the extent of alloying element segregation in the irradiated AGR fuel cladding using field emission gun (FEG) EDS chemical analysis in the TEM on thin specimens sourced from the Hinkley Point-B reactor [18, 44]. Both samples from the 410°C and 440°C batches of fuel cladding (Figure 17) exhibit appreciable alloying element segregation at the grain boundaries. Chromium decreased from its initial concentration of 20%wt to less than 10%wt, iron was decreased from 55%wt to less than 40%wt whereas nickel was enriched from 25%wt to 45%wt. The higher temperature 440°C sample exhibited wider, enhanced grain boundary damage distances of about 50 nm compared to the lower temperature 410°C sample of about 20 nm. Note that silicon was also significantly enriched at the grain boundaries.

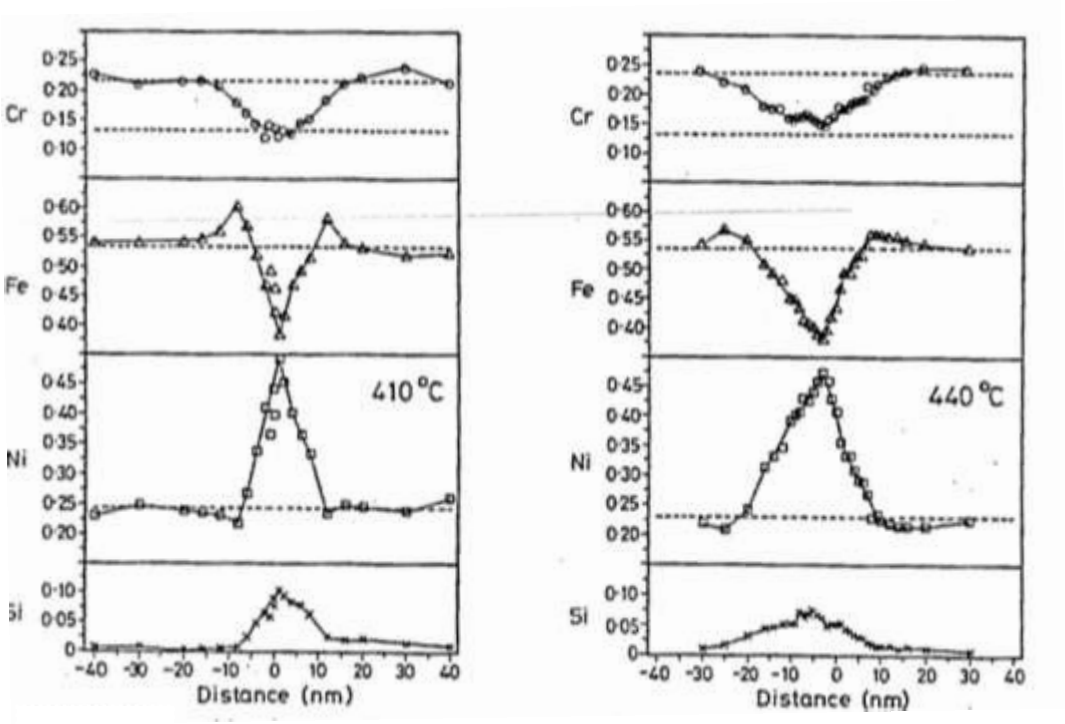

Figure 17 – Segregation of alloying elements at the grain boundaries, adapted from Norris *et al.* [18]

The radiation-induced segregation (RIS) phenomenon has been explained by the inverse-Kirkendall mechanism [45-47]. Initially, neutron irradiation induces a cascade of displacement defects in the bulk microstructure of the fuel cladding. Figure 18 illustrates the types of displacement defects which include the vacancy, self- interstitial atom, and substitutional impurity atoms. A vacancy is created when an incident neutron displaces a regular lattice atom leaving a 'vacancy' whereas the interstitial is the displaced atom itself. If the incident neutron is a prompt neutron or a primary knock-on atom (PKA), a cascade of displacement defects continues to occur until its energy dissipates. A vacancy and an interstitial pair are known as a Frenkel-pair [48]. Frenkel-pairs are mobile so that they may migrate through the lattice and interact with other Frenkel-pairs or solute atoms in the lattice, leading to increased concentration of defects (e.g., dislocations) especially at the grain boundaries where they annihilate. The substitutional impurity atoms, on the other hand, are fission fragments that result from the fission or transmutation of the alloying elements in the cladding. Subsequently, the inverse-Kirkendall mechanism proposed that each type of alloying element interacts with these displacement defects

a) Generation of point defects by primary knock-on neutrons

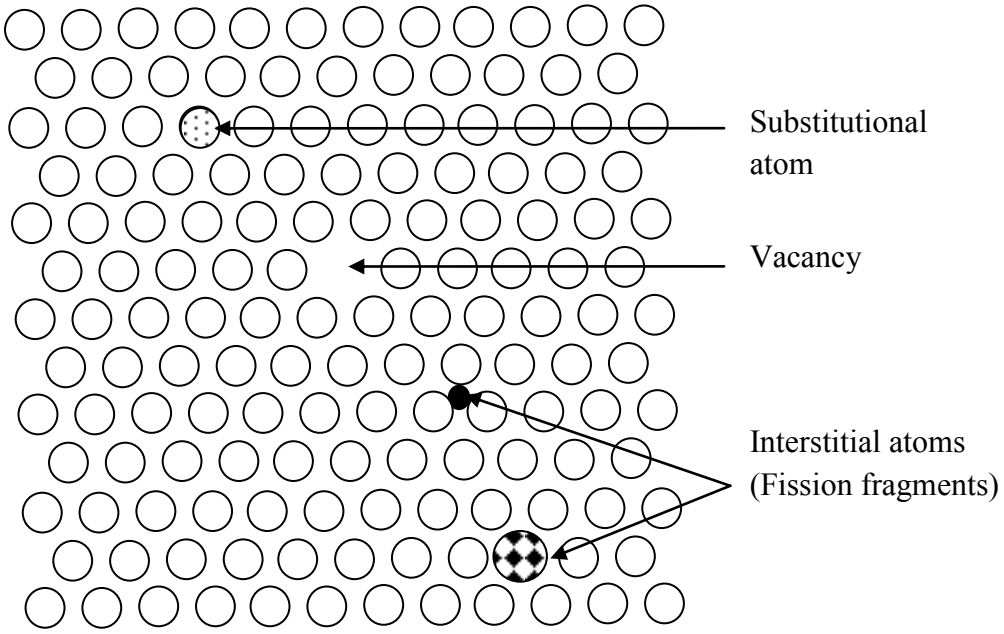

b) Preferential segregation of chemical species to sink (annihilation of vacancies at grain boundaries and dislocations) due to their different size and diffusivity, adapted from Smallman [56]

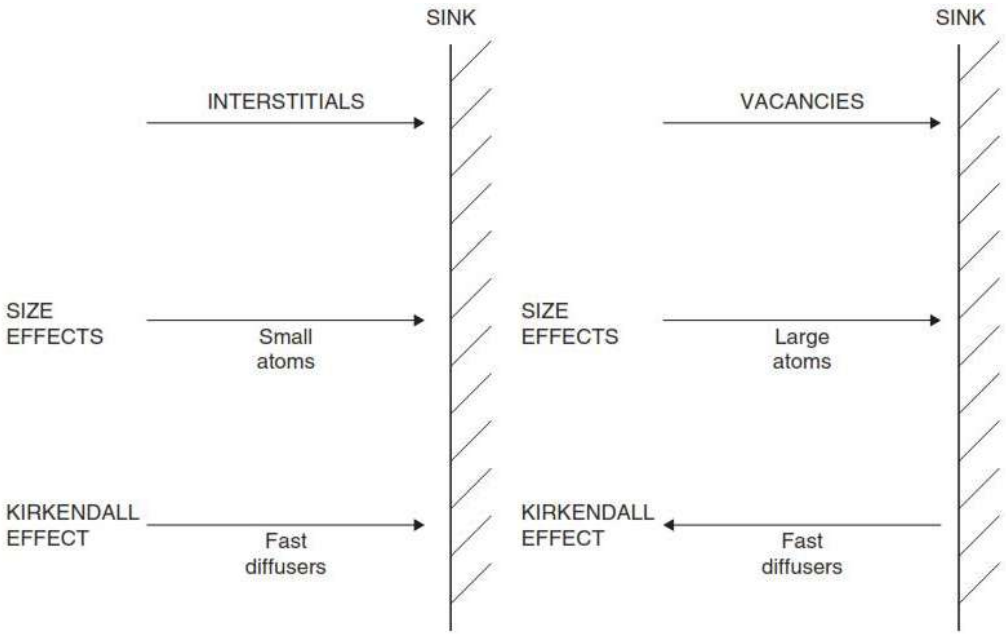

Figure 18 – Effect of neutron irradiation on metallic lattice that leads to radiation-induced segregation

at different rates due to their different diffusivity and size [45-47, 49]. Consider the alloying elements in the AGR fuel cladding have diffusivity (D) in the order $D_{Cr}>D_{Fe}>D_{Ni}$ and silicon has the smallest size. Figure 18b illustrates schematically that silicon (the small solute atom) is drawn into the sink, frequently the grain boundaries which the vacancy annihilates, but leaves behind its own vacancy (non radiation-induced) where the faster-diffusing solute chromium and iron move towards as an 'inverse flux' away from the grain boundary at the expense of nickel [46].

2.4.2 Radiolysis of water

Radiolysis of water concerns the emission of α, β, and γ radiation from the 'hot' fuel pellets that produce free radicals from the water molecules immediately adjacent to the cladding's surface [11, 43], increasing the metals corrosion susceptibility. An example of water decomposition by radiolysis is adopted from Stobbs and Swallow [11]: $4.5\ H_2O \rightarrow 3.7H^+ + 2.9OH^- + 0.4H_2 + 0.8H_2O_2$. A more complete range of water radiolysis products includes: H_2, O_2, O_2^-, HO_2, O_2 [43, 50]. Their concentrations, typically on the order of 10^{-10} to 10^{-8} molar and with lifetimes of micro- to nano-seconds, could differ substantially along the length of the fuel cladding since radiolysis yield depends on the neutron flux [50].

Once formed the radiolysis products may undergo further chemical reactions amongst themselves and participate in electrochemical reactions leading to corrosion. Table 9 shows the elementary electrochemical reactions and their rate constants. The anodic and cathodic (redox) reactions on the metal surface or at a locally-active site occur at different rates, in addition to the concentrations of the radiolysis yield being different. Consequently the potential for electrochemical reaction increases in the presence of radiolysis products; Wyllie *et al.* [51] have shown that the open circuit potentials (OCP, a condition where anodic and cathodic potential occurs at the same rate) of stainless steel 316 shifts to a lower value which is less noble from the starting materials. On a related note, the production of volatile species which include O_2 and H_2 may represent a combustion hazard [50].

Table 9 – Elementary equations and rate constants of water radiolysis [51]

Reaction	Rate Constant (s^{-1})
$e^- + H_2O = H + OH^-$	$2.4x10^{10}$
$e^- + OH = OH^-$	$3.0x10^{10}$
$H + H = H_2$	$1.0x10^{10}$
$e^- + HO_2 = HO_2^-$	$2.0x10^{10}$
$OH + OH = H_2O_2$	$4.5x10^{9}$
$H + OH = H_2O$	$2.4x10^{10}$
$H + O_2 = HO_2$	$1.0x10^{9}$
$OH^- + H_2O_2 = HO_2^- + H_2O$	$1.0x10^{8}$
$HO_2 = O_2^- + H^+$	$8.0x10^{5}$

Although radiolysis varies along the length of AGR fuel pins, the variation is much smaller than for LWR elements. Radiolysis is primarily caused by gamma radiation from the fuel and beta radiation from cladding. Post irradiation spontaneous neutron emissions are comparatively small. So axial radiolysis, and hence peroxide concentration, varies with local burnup (which in turn is related to time averaged neutron flux the fuel experienced in the reactor).

2.5 Corrosion of AGR Fuel Cladding

Once AGR fuels have reached a certain level of burn-up where they are no longer able to sustain chain reactions, they are discharged from the reactor core and wet-stored. Wet storage of the spent fuels can be divided in two sequences. First, the discharged AGR fuels are immediately stored in a pool of boric acid that is neutralized to pH 7 by caustic soda (NaOH) adjacent to the reactor. The element boron possesses one of the highest neutron absorption cross-sections (34400±30, Table 8) and so is an excellent neutron absorber. After a period of approximately 6 months [2], the spent fuels are transferred to the interim storage alkaline pond situated away from the reactor which is maintained with NaOH at pH 11.5 stabilisation condition. The pool is fabricated from reinforced concrete with water circulation to provide cooling so avoiding local temperature variations and filtration to ensure thorough mixing of freshly treated water returning from the chemical plant. The spent fuel remains here for several years pending reprocessing or, the more recent stance, permanent disposal in a geological repository [2]. Corrosion control of the spent AGR fuel in the alkaline ponds is critical for its long-term stability [2, 52]. This section reviews the critical factors affecting AGR corrosion processes.

When reprocessing is scheduled, the spent fuel is transferred to THORP. The recoverable materials include the remaining uranium-235 (< 0.7%wt) and the transmuted plutonium-239 for MOX fuel fabrication and long-lived fission fragments that can potentially be incorporated into fast reactor fuels for transmutation into short-lived ones. In the THORP facility, the spent AGR fuels are stored in a neutral pool of demineralised-water that is maintained at pH 7 and 25°C. As the pond also contains LWR fuels that were acquired from overseas spent fuel reprocessing contracts, the NaOH pH control with which the aluminium-based MEB may react cannot be used. The AGR fuel becomes vulnerable to corrosion without the NaOH inhibitor protection, having been subjected to radiation damage and in the presence of chloride anions (about 30 ppm) [2]. Due to Sellafield's proximity to the sea, trace concentrations of sea minerals predominantly chloride, sodium and sulphate may deposit into the ponds due to gravitational deposition of large (>15μm) sea-salt droplets.

In its broadest sense metal corrosion is one of the earth's most perplexing problems, costing billions of pounds to remedy in the utilities and manufacturing industry [53]. The AGR fuel cladding corrosion have shown to manifest in various forms which include surface rusts and subsurface-growing pits, crevices and inter-granular dissolution that over time progress to materials failure [2]. At the nanometre scale the strongly bound metal-metal atoms have disintegrated as free, unbound metal ions into the environment. The mechanisms by which this phenomenon may occur have been considered through several electrochemical reaction pathways [8, 54, 55] whose kinetics for metal dissolution is affected by the metal's quality, environmental conditions and the characteristic interface layer that forms between the latter, as schematically shown in Figure 19.

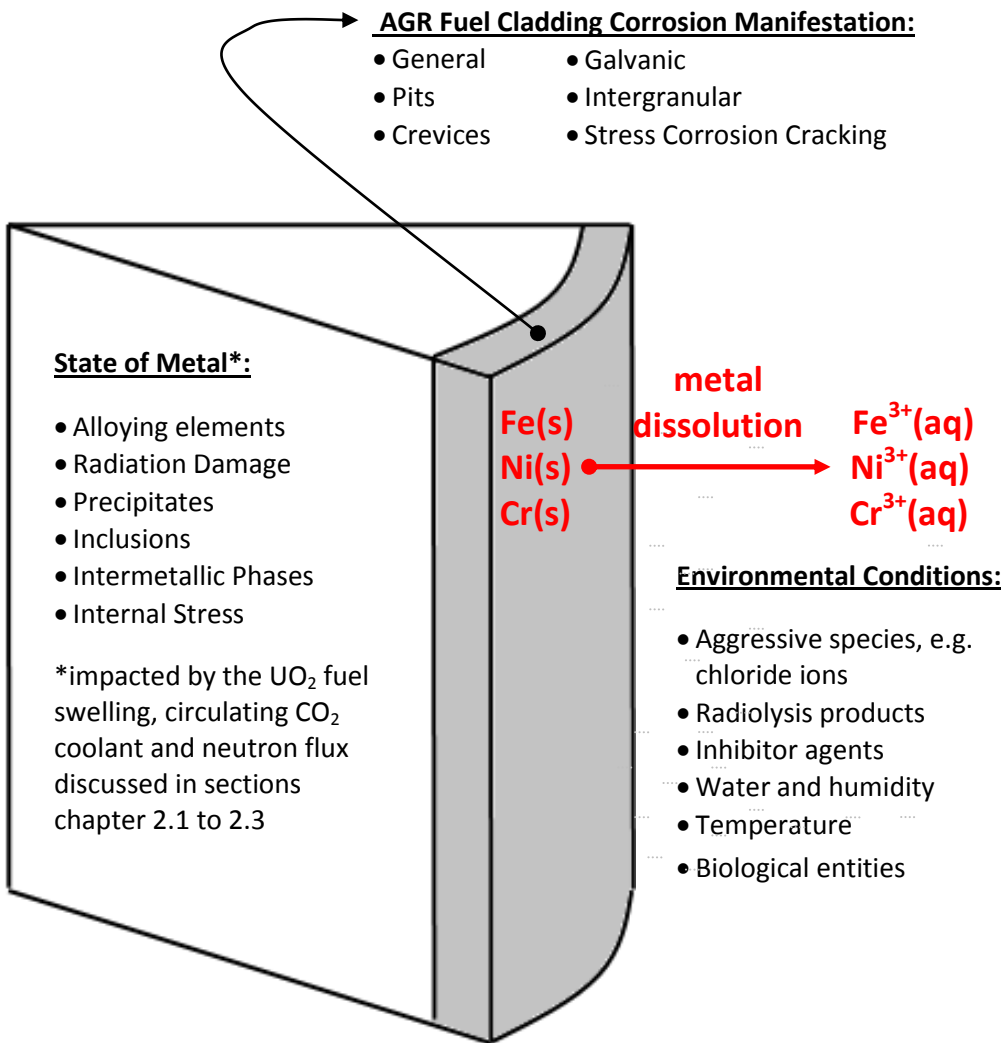

Figure 19 – Critical factors of AGR corrosion processes

Metals are traditionally improved by adding alloying elements and using modern steel-making techniques. A metal with chromium (Cr) contents above 12 %wt, for example, is corrosion resistant because chromium oxidises spontaneously in the atmosphere to form a surface-adherent chromium-oxide (Cr_2O_3) scale that protects the metal beneath [56]. Under neutron irradiation, however, this corrosion resistance degrades substantially due to irradiation-induced changes to its metallurgical properties which include precipitation of free chromium into a newly-formed secondary phase, incorporation of free chromium into the growth of existing secondary phases, and chromium depletion at the grain boundaries due to alloying element segregation [25, 48, 57]. Environmental conditions, on the other hand, promote metal dissolution by acting as the medium which carries charge from the dissolving metal (anode), i.e., electrons from the iron corrosion reaction $Fe(s) \rightarrow Fe^{3+}(aq)+3e$, to the next convenient adjacent site that is located at a cathodic potential in the electromotive scale. Natural environmental conditions such as elevated temperature, humidity, biological entities, and dissolved gas concentrations, notably in the presence of chloride, have been shown to escalate metal dissolution rates [40]. However, controlling environmental conditions such as by the use of corrosion inhibitors can slow and even stop corrosion reaction kinetics. Lastly, one of the crucial but puzzling considerations for metal corrosion is the exact mechanism of ion and electron transport processes underlying the nano-structures of the interface layer, which remains a significant knowledge gap in the field of corrosion science [53, 58].

2.5.1 Critical Factors Affecting AGR Corrosion Processes

There are three common classifications of localised corrosion problems in stainless steels: pitting, crevice and intergranular corrosion. Pitting corrosion (Figure 20a), as suggested by Frankel and Sridhar [59], is 'the localised metal dissolution on vulnerable surface area leading to the formation of cavities beneath the passive films'. Crevice corrosion (Figure 20b), according to DeForce and Pickering [60], is 'a form of localised corrosion in which a metal in contact with an aqueous solution dissolved within a crevice at a much greater rate than at other, crevice free surface' [60]. Example of crevices are metal *A*–metal *B* junctions, where *A* and *B* are separate metal components such as bolts, rivets, and gaskets, which over a service period may become sufficiently wide to permit the entry of corrodent ions but narrow enough to

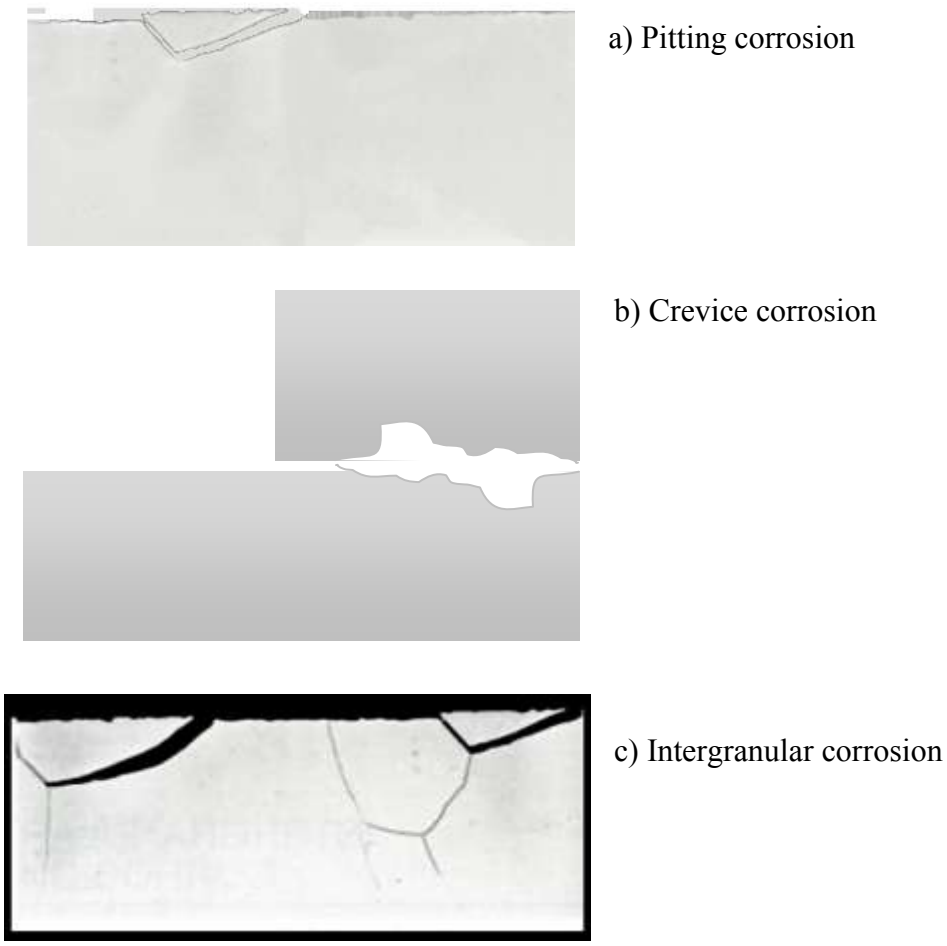

Figure 20 – Pitting, crevice and intergranular corrosion

ensure that the corrodent remains stagnant. Intergranular corrosion (Figure 20c), as defined in the ASM International Metals Handbook [21], is 'corrosion occurring preferentially at the grain boundaries, usually with slight or negligible attack on the adjacent grains'. This type of corrosion is penetrative to a certain depth within the subsurface grain boundaries and is an important propagation step preceding pitting or crevice corrosion. In the presence of stress, the latter can become intergranular stress corrosion cracking (IGSCC).

AGR fuel cladding is potentially susceptible to all three kinds of corrosion problems along its one metre length (Figure 6a). Pitting may occur at a local, electrochemically favourable site on the inhomogeneous fuel cladding surface that was oxidised by the CO_2 coolant. Crevices may be present at 'gaps' between the braces and the cladding (Figure 6c) in which the storage pond fluid may potentially access and remain stagnant to cause crevice corrosion. Intergranular corrosion arises because the cladding's grain boundaries are chromium-depleted due to radiation-induced segregation in the presence of stress field from the fuel pellet swelling (Section 2.1).

2.5.2 Metal Ion Hydrolysis and Acidification of Pits

The mechanisms that lead to the aforementioned corrosion problems are important. Of particular significance are the electrochemical reactions that cause the disintegration or dissolution of the strongly-bonded metal-metal atoms into the bulk electrolyte solution, i.e. $M(s) \rightarrow M^{n+}(aq) + e^-$ where M(s) is the bulk metal, $M^{n+}(aq)$ is the oxidised state of metal in the electrolyte solution with n being the oxidation number and e^- is the electron produced. Due to the direction of the latter reaction metal corrosion reactions are also referred to as anodic dissolution. Table 10 shows the anodic dissolution that pertains to the AGR fuel cladding alloy compositions and the corresponding standard cathodic reactions that take place simultaneously since the conditions of zero net current have to be satisfied. The cathodic reactions are reduction reactions that consume electrons.

Table 10 – Anodic and cathodic reactions on surface [53]

Anodic Reactions:	**Cathodic Reactions:**
$Fe(s) \rightarrow Fe^{2+}(aq) + 2e^-$	$O_2(g) + 2H_2O(aq) + 4e^- \rightarrow 4OH^-(aq)$
$Fe^{2+}(aq) \rightarrow Fe^{3+}(aq) + e^-$	$2H_2O(aq) + 2e^- \rightarrow H_2(g) + 2OH^-(aq)$
$Cr(s) \rightarrow Cr^{3+}(aq) + 3e^-$	
$Ni(s) \rightarrow Ni^{3+}(aq) + 3e^-$	
$H_2(g) \rightarrow 2H^+(aq) + 2e^-$	
$2H_2O(aq) \rightarrow O_2(g) + 4H^+(aq) + 4e^-$	

One of the basic models which partly describes the mechanisms of anodic dissolution is Galvele's uni-directional pit model [61, 62]. The initial stages of anodic dissolution, assumed to occur in the model, are initiated via some ambiguous conditions; perhaps due to slight imbalances in the electrolyte composition or an electrochemically unfavourable couple on the metal's surface. The anodic dissolution proceeds as the following:

- At its start metal dissolution may occur at the bottom of the pit, i.e. $M(s) \rightarrow M^{n+}(aq) + ne^-$.
- In the next steps the electrons (ne) that are produced are consumed for hydrolysis or cathodic reactions to maintain charge neutrality; this may include $O_2+2H_2O+4e^- \rightarrow 4OH^-$ or $M^{n+}+H_2O \rightarrow M(OH)^{n-1}+H^+$ that hydrolyses the water molecules and in which product H^+ indicates pit acidification.
- In addition, the free metal ions $M(OH)^{n-1}$ may readily attract the migration of free chloride (Cl^-) to the bottom of the pit and form metastable complexes such as $M(OH)^+Cl^-$. They are unstable constituents that undergo further hydrolysis reactions, i.e., $M(OH)^+Cl^-+H_2O \rightarrow MOH+H^++Cl^-$ that leads to the generation of more acidic regions at the bottom of the pit.

Exactly what types of metastable complexes formed, if they do form, is a contentious subject. Nonetheless, in this instance, it can be assumed that the aforementioned metal dissolution and hydrolysis activities generate a pit current density, denoted by *i*. Galvele showed that the product *i* and the depth of the pit *x*, as indicated in Figure 21, is a critical quantity which dictates whether a pit is active, in

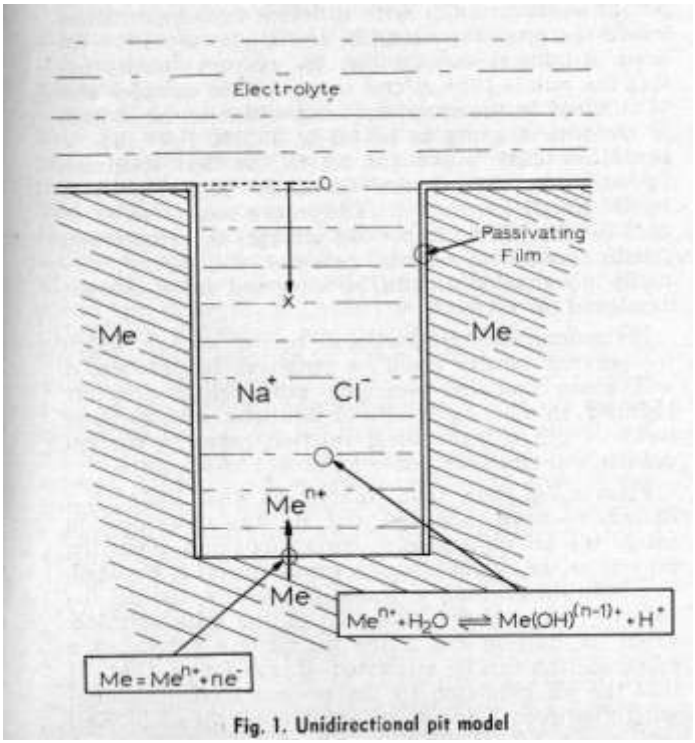

Figure 21 – Unidirectional pit model proposed by Galvele, adapted from Galvele [61]

which the self-sustaining propagation mechanism would continue to occur, or passive, in which the pit would cease to grow. In this way, the 'current will produce a time-dependent local concentration built up of metal cations, until steady state conditions are reached'.

In practical terms, however, anodic dissolution encompasses a wider, dynamic aspect that includes several other factors. For one, the rate or kinetics of anodic dissolution is mediated by the environment. The presence of anions such as chloride (Cl^-), sulphate (SO_4^{2-}), thiosulphate ($S_2O_3^{2-}$), dissolved oxygen (O_2), dissolved ozone (O_3) and certain microbes, in addition to thermodynamic factors such as temperature and fluid velocity in contact with the metal, accelerates the rate at which metal corrosion processes occur [63-66]. The anions or cations in the electrolyte solution are thought to influence the characteristics of the electrical double layer that is formed instantaneously at the metal's surface upon environment contact [67-70]. This double layer, which is an electrical field, in turn has the potential to break down the Cr_2O_3 passive film [71].

With regards to the passive-film breakdown the key questions concerning its initiation are: what mechanism does it undergo and where does the charge dissipate? The mechanisms of passive-breakdown, according to the review by Frankel [72], could be due to the theories of: penetration, adsorption and film-breaking. The penetration theory states that the high electric-field in the film assists transport of aggressive anions, e.g. chloride, *through* the passive film, though it contended that it was not always the case where chloride is found in the passive film. The adsorption theory suggests that passive-film breakdown is caused by the more competitively-adsorbed chloride ions than the oxygen, e.g, the oxygen in the chromium-oxide film. This theory, too, has reported inconsistency in experimental results. Lastly, the film-breaking theory considers that the 'passive-film is in a continual state of breakdown and repair'. The alteration to this steady state of breakdown and repair is affected by the presence of chloride-containing solution. Pertaining to the charge transfer processes, theoretically, the electrons from the dissolution process should be consumed by one of the cathodic reactions in Table 10. However, Gileadi *et al.* [73-75] have contended the traditional dissolution theory with the prospect that electrochemical reactions are strictly governed by ion transfer, not electrons.

Additionally, taking into account the role of inclusions in passive film breakdown, some observations suggest that corrosion evolution is manifested around secondary phases in the metal matrix. Figure 22a, adapted from Ryan *et al.* [13], showed corrosion processes that are occurring around a manganese sulphide (MnS) precipitate. Bohni *et al.* [15] showed that large precipitate sizes are detrimental to pitting corrosion. Figure 22b shows that inclusions of size greater than one micron possess a greater affinity for pitting indicative of the low pitting potential of just 400 mV (vs. saturated calomel electrode). The presence of inclusions or secondary phases potentially produces a galvanic effect between the inclusion itself and the bulk metal, promoting self-sustaining electron transfer processes due to their relative electromotive potentials.

Apart from inclusions, passive film breakdown has also been observed to involve a metal lacy cover [55, 66, 76]. Figure 23 shows that a lacy metal cover is characterised by a porous metallic cover on the metal surface under which a

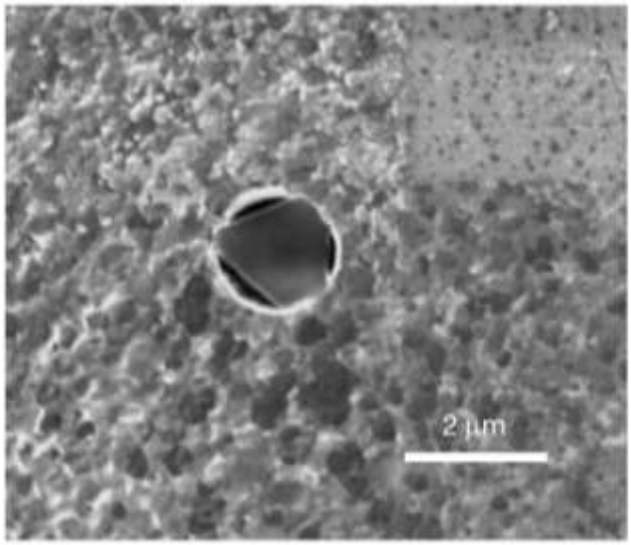

a) Voids around the MnS inclusion, adapted from Ryan *et al.* [13]

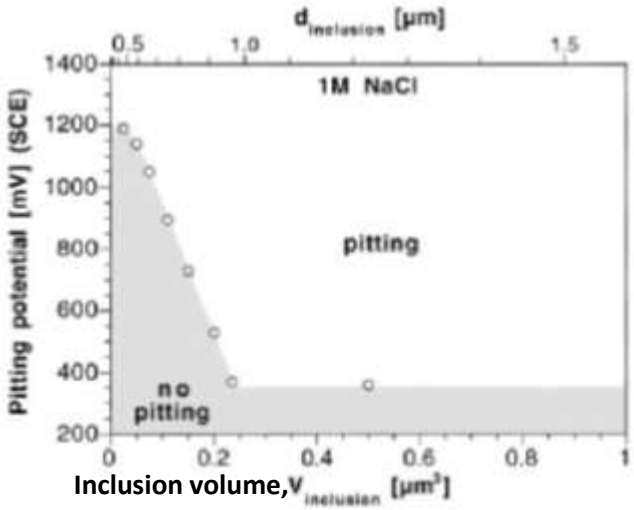

b) Correlation between pitting potential and inclusion size, adapted from Bohni *et al.* [15]

Figure 22 – Role of manganese sulphide inclusion in corrosion processes.

hemispherical-shaped pit is evolving or has stopped. Ernst *et al.* [55, 76] suggest that the evolution of the hemispherical pit is a mass transport process controlled by the concentration of the metal dissolution product, i.e. the metal-chloride cation, that forms between below 70% of its saturation concentration. The finely perforated lacy metal cover stabilises the corrosion evolution *initially* by acting as a diffusion barrier.

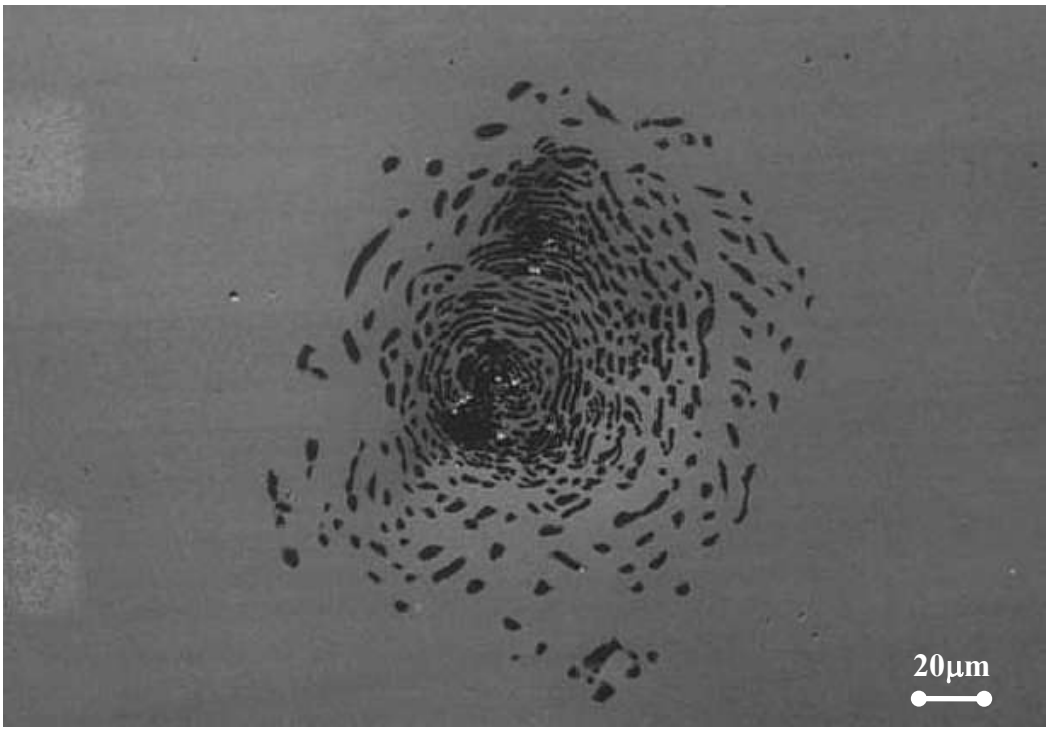

Figure 23 – Secondary Electron Image of a lacy metal cover, adapted from Ernst *et al.* [55]

3.0 Experimental Methods

This chapter detailed the experimental methodology that was adopted for characterising the effect of microstructure on the corrosion behaviour of the as-manufactured AGR fuel cladding sourced from Sellafield Ltd, Cumbria. Section 3.1 described the procedures for i) thermal-aging of the individual small-cut cladding specimens at discrete temperatures of 400, 500, 600, 700 and 800 °C for 24, 48, 96 and 192 hours to produce individual specimens of varied microstructure and ii) fabrication of the thermally-aged specimens as electrodes for corrosion measurements. Section 3.2 described the procedures for corrosion measurement – specifically the anodic polarisation method – that was employed to measure the corrosion potential of the electrodes (fabricated from thermally-aged specimens) in both 0.001M and 0.1 M sodium chloride (NaCl) electrolyte. Section 3.3 describes the procedures for *surface* corrosion morphology characterisation of the post-polarised electrodes by Scanning Electron Microscopy (SEM). Section 3.4, similarly, describes procedures for the *subsurface* corrosion morphology characterisation of the post-polarised electrodes. Specifically, the subsurface corrosion features are obtained using the Focused Ion Beam (FIB) instrument to acquire cross-sections above a corrosion site that is subsequently measured using Energy Dispersive X-ray Spectroscopy (EDS) in the TEM for its chemical composition of the austenite grains, grain boundaries and secondary phases. Section 3.5 detailed procedures for a series of etchant testing in order to evaluate the etchant most suitable to reveal under the SEM the physical distribution of the austenite grains, grain boundaries and secondary phases that have been varied due to thermal-aging. This includes development of an algorithm for quantifying the numbers and sizes of secondary phases by image processing and statistical analysis.

3.1 Heat Treatment and Electrode Preparation of As-sourced AGR Fuel Cladding

A unit of as-manufactured AGR fuel cladding rod which has been manufacturer-annealed (1050°C, 2 hours) was sourced from Sellafield Ltd, Cumbria. Figure 24a shows an AGR fuel cladding that resembles a hollow tube, allowing for the insertion of 64 13mm long and dia. uranium-dioxide (UO_2) fuel pellets. The fuel

cladding is austenitic stainless steel 20Cr/25Ni/Nb and measured 100.0cm long by 1.5cm dia. with 0.38mm wall thickness. Using a wire electro-discharge machine (EDM) cutter (GF AgieCharmilles; Model CUT20; North View, Coventry, CV2 2SJ) and a custom-made hexagonal jig to support the length of the cladding in the machine, the cladding was sectioned at every 1.5cm intervals producing a series of 'rings'. Each of these 'rings' was subsequently cross-sectioned into 8 1.5cm wide by 1.0cm long cut-samples (Figure 24b). The EDM utilises spark-cutting mechanisms and machining was carried out under water to minimise thermal stresses generated in the metal.

The cut-samples were heat-treated using a chamber furnace (Carbolite Furnaces; Model 1200 S/N: 4/91/559; Bamford, Sheffield, S30 2AU) equipped with a Eurotherm 120 thermostat. Heat treatment was performed on the cut-samples in order to produce a range of microstructure features for characterisation. The heat treatment involved the following preset temperatures and times: 400, 500, 600, 700 and 800°C and 24, 48, 96 and 192h. In the furnace chamber the cut-samples – in batches of five laid flat on a crucible (Figure 24c: inset) – were subjected to a heating ramp rate of 20°C/min to the preset heating temperature.

Each of these thermally-aged cut-samples was fabricated as working-electrodes in order for their corrosion properties to be tested using the anodic polarisation method described in section 3.2. Fabricating the samples as working-electrodes is essential to ensure that the three-electrode cell's alligator-clip (Figure 26a) is electrically-connected to a sample that is free from crevices and edge-inhomogeneities. The aim is to provide an electrically-connected sample surface that is homogeneous, well-polished and flat for the anodic polarisation testing. These attributes can be achieved via two steps. First, a short wire-extension that can be gripped by the alligator-clip was provided by a 0.2 mm diameter fine-wire (7/0.200mm PTFE sleeve; Belden OL15 8YJ) that is electrically-connected to the 'rib-free' surface of the cut-samples. To ensure electrical connection between the wire-extension and the sample, several layers of silver paint were applied to the contact-area and tested for zero-resistance using a voltmeter (ISO Tech Multimeter; Model IDM91E; RS Components Ltd., Northants, NN17 9RS) set at 20kΩ. Second, the cut-sample with the wire-extension intact was moulded into epoxy-resin (Struer Epofix Resin and Harderner Kit; Struers Ltd., Rotherham, S60 5BL) in a fume-hood.

a) As-sourced AGR fuel cladding

b) Cut-samples

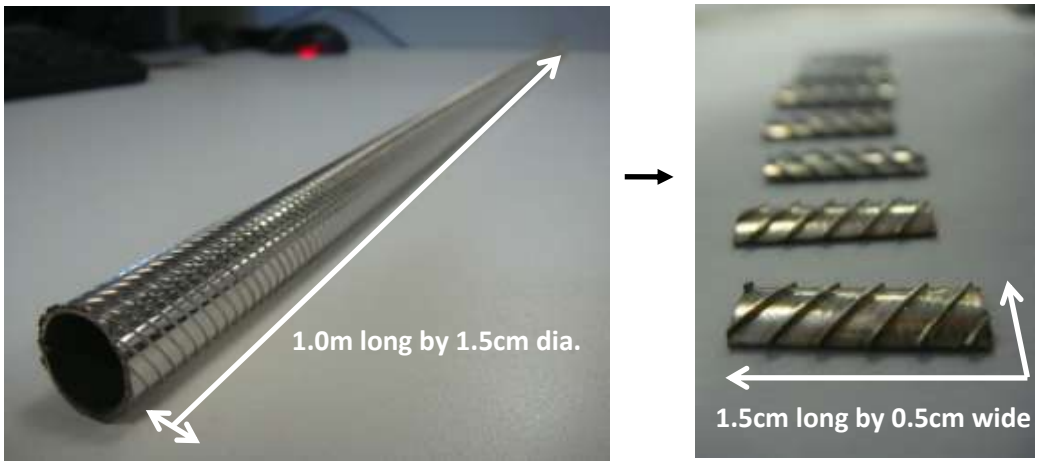

c) Heat treatment (inset: sample on crucible inside the oven)

d) Working electrode from thermally-aged samples

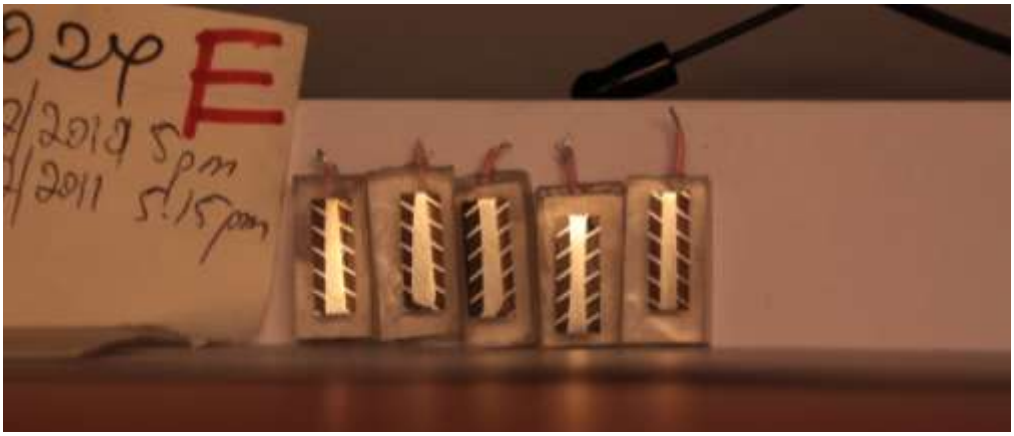

Figure 24 – Preparation of working-electrode from as-sourced AGR fuel cladding rod

Upon drying and hardening of the mould, this article has greatly enhanced general handle-ability considering the relatively small dimension of the freshly cut-samples (Figure 24b). The mould was mechanically ground (Struers ROTOR Polishing Unit; Struers Ltd., Rotherham, S60 5BL) with silicon carbide paper from coarse grit-size of 400 to fine grit-size 1200 followed by diamond polishing (diamond particles embedded in cloth laps) with 3µm abrasive particles and finished with 3µm particles. Each grinding and polishing step was performed for no less than three minutes at a rotary speed of 200 rpm. After final polishing the sample was re-checked for zero-resistance using the voltmeter and, if this was the case, categorically designated as a working-electrode of the heat-treatment in question. Figure 24d shows five working-electrodes from the 500°C 24h heat treatment.

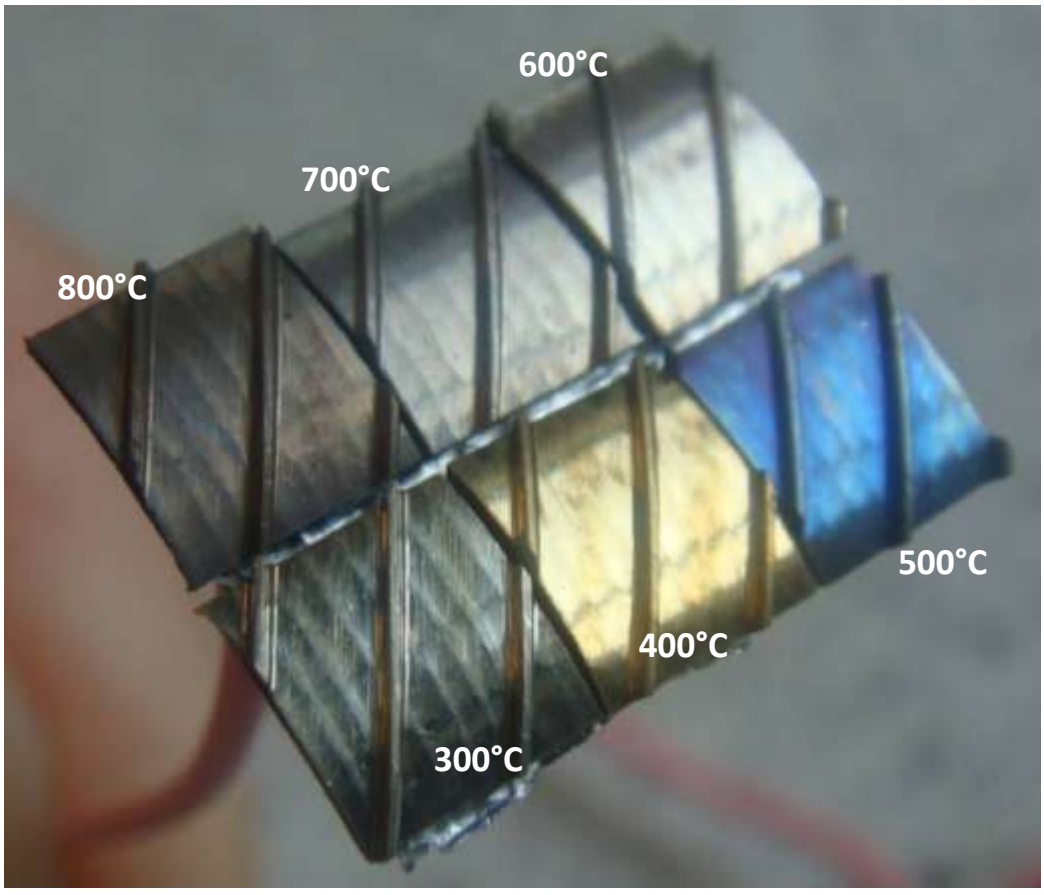

Figure 24b – Surface oxide layer of heat-treated specimens (2h) that was polished off for corrosion measurement of bulk microstructure.

3.2 Corrosion Measurements using Anodic Polarisation

The anodic polarisation method is an electrochemical technique commonly used to quantify a metal's potential for corrosion [63]. This method is employed to quantify the corrosion potential of the electrodes fabricated from the thermally-aged AGR fuel cladding cut-samples (section 3.1). In principal the electrode, submerged in an electrolyte solution, is applied a positive rate of increasing electrical potential and simultaneously measured its current evolution which is characteristic of the state of the sample and the type and concentration of the electrolyte solution.

The general experimental setup of the anodic polarisation method, which comprises the working electrode (WE), counter electrode (CE) and reference electrode (RE), is schematically illustrated in Figure 25. Note that the electrodes are submersed in the electrolyte solution and are connected terminals of a potentiostat device. Regarding the terminal connections, a sample of interest is always connected to the WE terminal. Upon submersion in the electrolyte, an electrical double layer forms spontaneously on the sample surface where the potential drop across the layer gives rise to the WE's electrochemical potential, V_{WE}. The absolute value of V_{WE}, however, cannot be determined standalone but, rather, is measured against the potential of a RE that acts as an arbitrary zero potential value. Commonly used RE terminals include the silver/silver-chloride (Ag|AgCl) electrode which contains metal silver submersed in silver chloride solution, saturated calomel electrode or the standard hydrogen electrodes. As is expected, the unique double layer that forms gives rise to the RE's electrochemical potential, V_{RE}. A voltmeter between the WE and RE terminal measures the voltage or potential difference between V_{WE} and V_{RE}. The voltmeter is read as V_{WE} in reference to V_{RE} and commonly reported in the notation *volts (V) versus Ag|AgCl*. At rest condition with no external current applied, the natural value of V_{WE} is referred as the open circuit potential (OCP). Lastly, the CE terminal is connected with an inert metal, usually platinum, which only plays a role in completing the cell's current flow in the test solution.

A potentiostat device through a user-interface computer program is used to alter the potential of V_{WE} to either above or below its OCP. In anodic polarisation studies, V_{WE} is incrementally increased from its OCP towards the noble direction (contrary to metal deposition studies in which V_{WE} is decreased from its OCP values) [77]. The potentiostat controls the V_{WE} values by altering the V_{RE} and subsequently

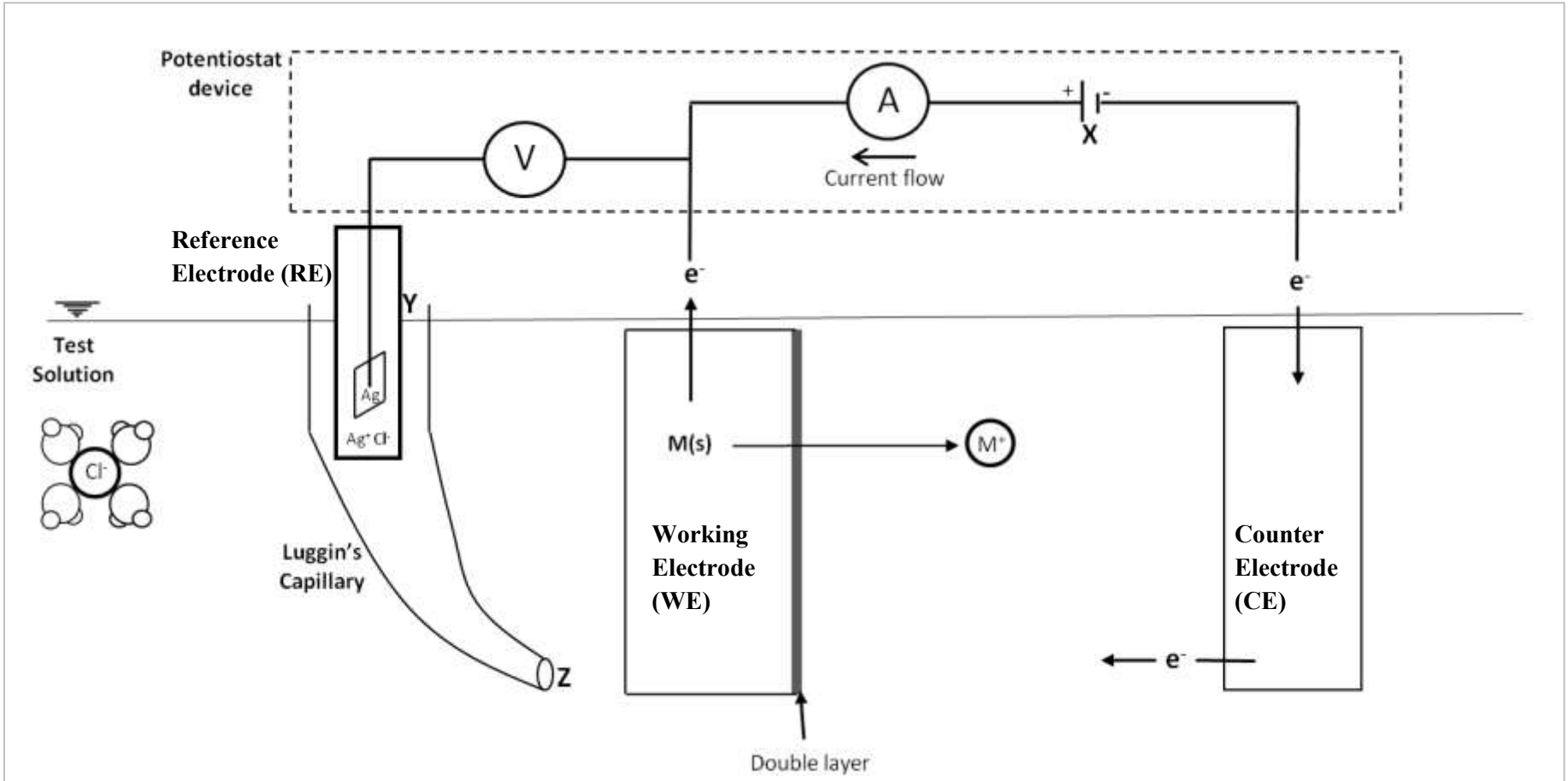

Figure 25 – Three electrode cell notations and operating principles

maintaining V_{WE} at V_{RE} by applying an external current (marker X in Figure 25). According to Ohm's law, V_{WE} equals current flow (i) times resistance (R); since R is constant, i is imposed via an external source to increase V_{WE} until it matches V_{RE}.

A condition related to low conductivity is the IR drop. Corrosion current measurements can be obscured in low electrolyte-containing test solutions due IR drop. Pure water, for example, is a poor electrical conductor due to lack of charge-transporting electrolytes and thus possesses a resistance that prevents the current movement through the test solution. To minimise the effect of solution IR drop, the reference electrode is placed in a Luggin's capillary which is a glass tube filled with the same test solution as in the bulk that extends close to (but not shielding) the surface of the working electrode. Consequently, there is no current flowing between point Y and Z indicated in Figure 25, since there is no exit for the current in that tube. The IR drop that remains within the small distance between Z and the electrode's surface is usually negligible [71].

In the anodic polarisation tests employed throughout this study, polarising the *working-electrode* above its anodic potential was carried out using a three-electrode cell as shown in Figure 26a. The cell utilises a platinum *counter-electrode*, silver/silver-chloride (Ag|AgCl) *reference-electrode* placed in a Luggin's capillary and 80 ml. of electrolyte-NaCl solution. The cell is driven by a General Purpose Electrochemical System (GPES) Potentiostat (Model VersaSTAT3; S/N: Autolab AUT73534; Princeton Applied Research, Oak Ridge, TN 37830, USA). The polarisation tests were evaluated at two concentrations of *electrolyte-NaCl* – 0.001M and 0.1M – prepared by mixing 3.045 g and 0.029 g of NaCl (VWR BDH AnalR; NaCl 58.44g/mol, Lot K33094133412; VWR International, Lutterworth, Leicestershire LE17 4XN), respectively, into one litre of de-ionised water (Purite Select <0.005 mg/ml solids, 18.2MΩ). In addition, the three-electrode cell configuration was placed in a large Faraday Cage (340cm by 340cm base and 600cm tall) to improve the sensitivity of current measurements against the influence of external electric fields [77]. The experiments were carried out at room temperature. Ten minutes of equilibration time was allowed for the working-electrode's submerged surface to be in contact with the electrolyte-NaCl before starting a measurement.

a) Raw current measurements in a three-electrode cell

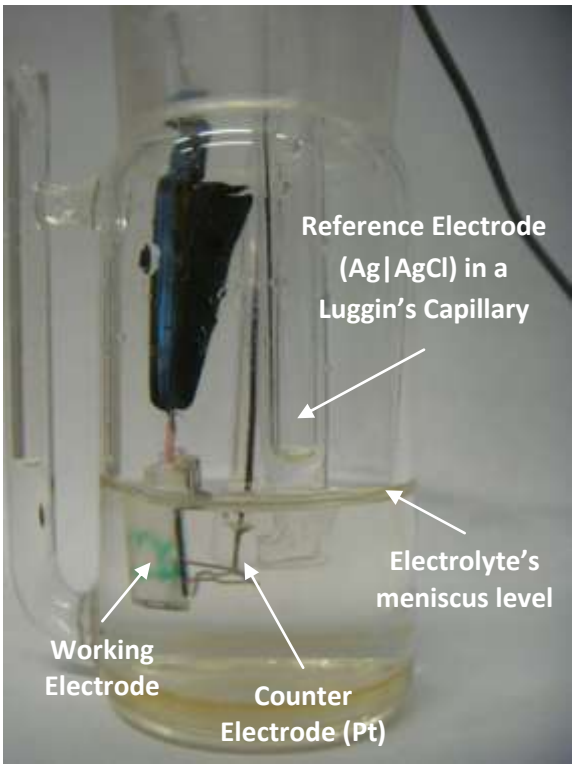

b) Normalising the measured currents with surface-area exposed to electrolyte-NaCl

The calibrated Motic Image Plus software indicates that the image above has an actual dimension of 7.11 by 10.49 mm

MATLAB determines, by differentiating brightness and contrast pixel values, the area exposed to electrolyte as 0.21 cm^2

Figure 26 – Raw current measurements in a three-electrode cell (a) and procedures for normalising the measured current to surface area submerged in electrolyte (b).

Using the GPES software, the potential of the working-electrode, V_{WE} (Volts, V (Ag|AgCl), was set to increase from -0.2 to 1.8V at a ramping rate of 0.0106V/s. As V_{WE} is increased, the corrosion current, *i* (Amperes, A), is simultaneously measured. At the end of a measurement, the working-electrode in question was immediately removed from the solution and thoroughly rinsed with generous quantities of de-ionised water followed by drying with a jet of air. The dried samples were stored in a cylindrical specimen-tube (SAMCO Vials, 48mm high x 10mm diameter - 2.6 ml; ThermoFisher Scientific Ltd, Southend-on-Sea, Essex SS2 5PH) with a small desiccating silicate-pack to preserve the sample against deterioration by moisture. The post-polarised working electrodes were to be retrieved for characterisation of corrosion morphology in a Scanning Electron Microscope (SEM) and Light Interferometer (LI) (Section 3.3), preparation of electron transparent cross-sections using the Focus-Ion Beam (FIM) instrument for compositional analysis in a Transmission Electron Microscope (TEM) (Section 3.4), and etched for general metallographic examination of grain structure and sizes as well as distribution of secondary phases using SEM (Section 3.5).

The reliability of the current measurements was established by repeating the above procedures with two new samples with fresh electrolyte-NaCl solutions in order to obtain the mean and standard deviation values. That is, a total three anodic polarisation measurements were evaluated for each specific heat-treated sample. Should the mean current measurement be calculated as X and standard deviation as Y then there is a 95% chance that the true mean is within plus or minus two standard deviations. To illustrate, if the measured mean current X is 10.0 mA and standard deviation Y is 2.0 mA then there would be a 95% chance of being correct to claim that the true average of our mean estimate 10.0 mA was between 6.0 and 14.0 mA. Sources of uncertainty in the experiment include solution preparation, working-electrode surface area determination and irregular Luggin's capillary placement in the three-electrode cell throughout the experimental duration.

The current measurement of a given sample is characteristic not only of the heat-treatment but also of its surface area submerged in the electrolyte-NaCl solution. The current measurement, therefore, is normalised against its post-corrosion surface area evaluated using a creative digital-image processing procedure. There were two

steps. In the first step, the general dimension of the post-corrosion working-electrode was evaluated with a Light Microscope (LM) (NOVEX Microscopes; Model: RZT-SF; S/N: 65-560; Papenkamp 20, 6836 BD Arnhem, The Netherlands) that was calibrated to the sample's geometric range. An Image Capture Camera (Moticam 480; S/N: S573763; The Global Motic Group, Xiamen 361006, China) on the LM was used to acquire a digital picture of the sample with the appropriate scale-marker. Figure 26b shows a 500°C 48h heat-treated working electrode which was determined from the calibration to have a physical dimension of approximately 7.11 by 10.49 mm. In the second step, this image was processed with a MATLAB code utilising the Image Processing Toolbox aimed at resolving the brightness-contrast pixel difference of the image. The MATLAB algorithm is provided in Appendix I. Figure 26b also shows that this particular working electrode has a surface area contrast that was subjected to electrolyte-NaCl solution of approximately 0.21cm^2. Normalised or effective current measurements in units of $mA.cm^{-2}$, including the standard deviation, were reported throughout the thesis.

3.3 Morphology Characterisation of the Polarised Working Electrode

The corrosion morphology of the polarised working-electrode was characterised using a SEM [78]. High resolution images were obtained by detection of interacted electrons from an incident electron beam that was rastered over a surface area of interest under a vacuum generally better than 10^{-6} Torr. Alone amongst the various types of interacted electrons (e.g. backscattered, secondary, auger, diffracted, and transmitted), the secondary electron – orbital electrons that are ejected from sample atoms by the incident electron beam – were detected to produce the secondary electron images (SEI). The SEM (Model LEO 1525; S/N: 1289; Zentrum für Werkstoffanalytik Lauf (ZWL) GmbH, Hardtstrasse 39b, 91207 Pegnitz, Germany) was configured at an acceleration voltage of 20kV and an aperture size of 60μm to eliminate the high-angle electrons from the beam source. Note that for chemical composition quantification, even though information can be conveniently obtained by detecting the characteristic X-ray from the electron interactions within the SEM, this study employs instead the scanning Energy Dispersive X-ray (scanning-EDX) technique in the TEM from the specimens prepared using the FIB instrument (detailed in Section 3.4). The benefits of chemical analysis using the scanning-EDX technique on thin foils are threefold. First, the measurement uncertainties associated with the penetrative nature of electrons that may pervade several microns deep beneath an unprepared, bulk metal at an acceleration voltage of 20kV are eliminated (i.e., large 'activation volume' of the electron beam may give chemical measurements that are irrelevant to the corrosion site of interest). Second, bright-field, dark-field and energy loss signals can be acquired simultaneously as more information is gathered per incident transmitted-electron in the TEM. Third, 'line-scan' chemical analysis on the FIB cross sections from *developing* corrosion sites – for instance corrosion sites immediately adjacent to secondary phases such as MnS or NbC as suggested by studies of Pardo *et al.* [79], Ryan *et al.*[13] and Williams *et al.* [14] – enables the mechanism of corrosion to be determined.

In addition to corrosion morphology imaging, the other physical characterisation of the polarised working electrode is the evaluation of the *ratio of width to depth* of the *well-developed* pits and crevices. Two techniques have been developed for this purpose. The first uses the ion-sputtering capability of the FIB

microscope (detailed in Section 3.4). The FIB microscope produces a highly-energetic Ga *ion beam* that physically exerts a cascade of collisions on the targeted area to cause ejection or sputtering of atoms. In order for the width and depth of a particular pit or crevice to be evaluated, the targeted area for FIB sputtering is about half the size of a site of interest until a sufficiently deep trench is formed. Figure 27

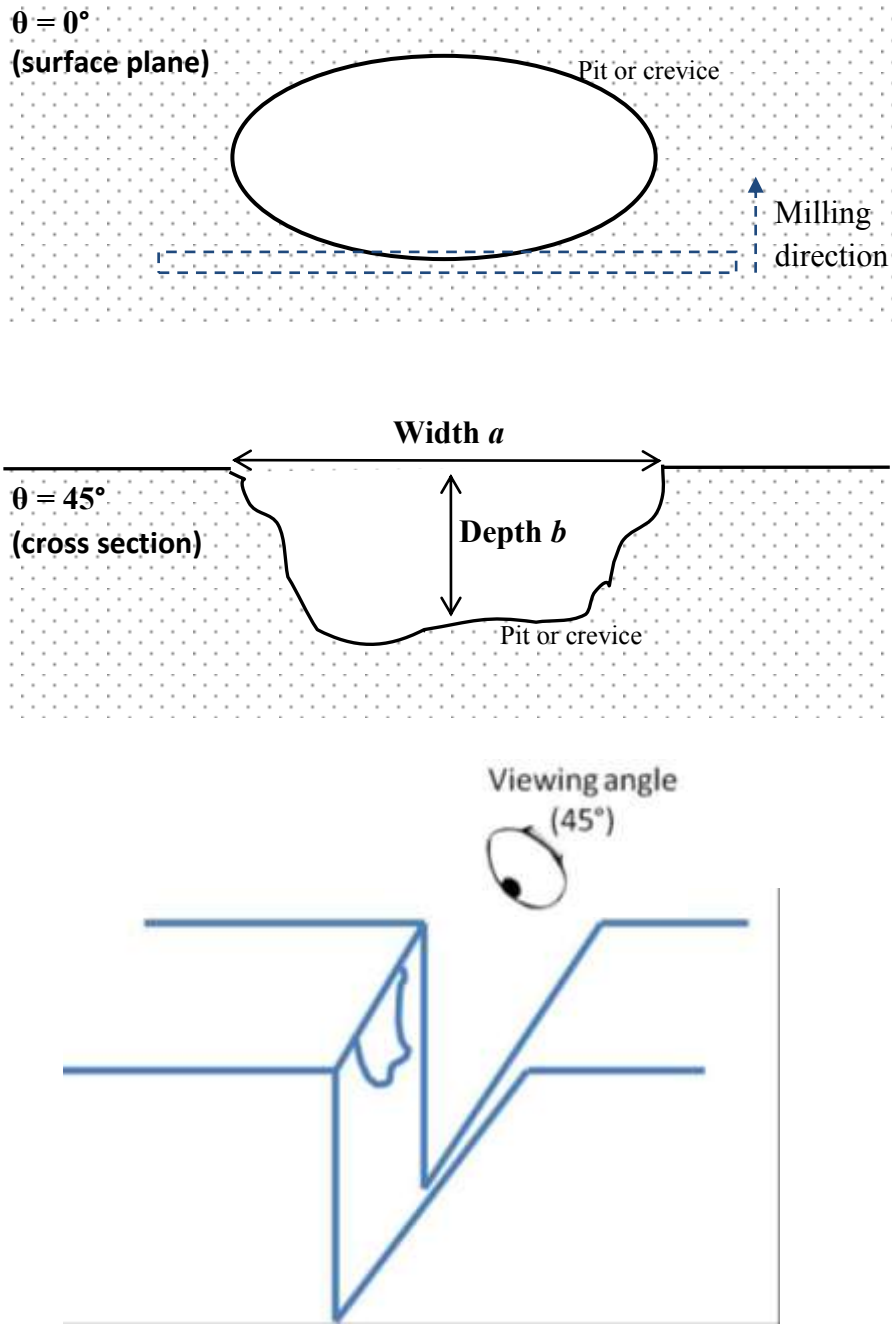

Figure 27 – Evaluation of pit or crevice's width and depth of the post-polarised working electrode

illustrates schematically the FIB sputtering operation. The dotted-rectangle shows sputtering intervals – with maximum ion current intensities of 20 nA – that are successively aimed towards the centre of a pit or crevice of interest. At a tilting angle of 60° the ratio of width to depth was evaluated.

The second technique utilises an Light Interferometer to determine the 3-D topography of a pit or crevice of interest where the ratio of width to depth can be subsequently determined. The 3-D topography was acquired using a scanning-white light interferometer (ZYGO Interferometers; Model: NewView 200; S/N: 98-08-60674; ZYGO Ltd Middlefield, CT 06455, USA). In principal, as the interferometric objective lense is scanned along the vertical direction (z-axis) of the stainless steel sample, the 3-D topography of this highly reflective material is mapped from the *coherent interference* with the white light (Figure 28). Coherent interferences are a result of the optical recombination between the initially split light source by an internal reference mirror – causing bright (constructive) and dark (destructive) fringes – and the sample interferences [80].

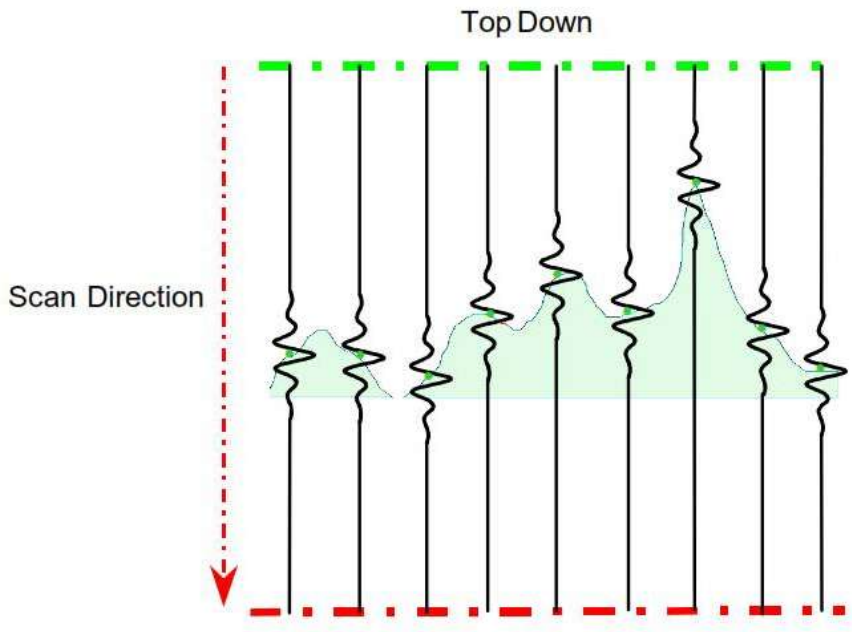

Figure 28 – Build-up of white-light interference on sample surface, adapted from Leach *et al.* [80]

3.4 Morphology and Chemical Composition of Corrosion Products

FIB microscopes have been used increasingly in material science applications which include Secondary Ion Mass Spectrometry (SIMS) and Low Energy Ion Scattering (LEIS) analyses [81-85]. Whilst specimen preparation from the post-polarised working electrode for TEM analysis is focused in this section, FIB has been used extensively for circuit modification in the semiconductor industry utilising its *in-situ* sectioning and micro-machining capabilities. Ion-beams are generated in FIB microscopes as compared to electron beams in conventional electron microscopes; therein lie its advantages and limitations. As ions are large relative to electrons they are able to sputter materials and so shape them for examination. In addition, the sputtered ions can be collected for surface or mass spectrometry analysis of important lighter elements such as beryllium, carbon, nitrogen and oxygen that cannot be detected from characteristic X-ray analyses. Energy Dispersive Spectroscopy (EDS) in the SEM, for example, is limited by beryllium window detector which prevents the passage of characteristic X-rays with energy less than one keV, i.e. K_α X-rays below sodium (Na, Z=11) [86]. However, ion-induced damage, in addition to other consequences such as tunnelling, amorphophrisation, and redeposition of sputtered materials [87] render FIB unsuitable for certain type of studies where sample perseveration is an issue. Both the resulting secondary ions and electrons can be collected for imaging.

The FIB microscope (Model: FEI FIB200; S/N: 4604; Software version; Xpert ver. 2.25; FEICO, Hillsboro, Oregon 97124 USA) was used in this study to prepare samples for elucidating subsurface information of the post-polarised working electrode. There are two specific applications. First, as described in Section 3.3, determining the ratio of depth to width of *well-developed* pits or crevices was enabled by FIB-milling of about half the size of the site of interest, subsequently allowing a clearance for geometrical evaluation of the site when tilted at 60° (e.g., Figure 27). Second, the FIB microscope is used to prepare electron transparent cross-sections (abbreviated to FIB-sections) ~0.1 μm thick for chemical composition analysis in the TEM. The cross-sections are mostly chosen from sites that exhibit *developing* pits or crevices – in particular those around secondary phases such as manganese sulphide (MnS) or niobium carbide (NbC) – in order to examine the factors governing their corrosion evolution processes. The FIB microscope was

equipped with a gallium-Liquid Metal Ion Source (Ga-LMIS). The accelerating voltage for the ion column was set to 30kV and ion emission current was optimised at 2.3μA. The sample is positioned in the vacuum chamber at eucentric height where the ion-beam focus does not change laterally while tilting the sample (a manipulation extensively used throughout FIB-section preparation). The ion currents for sputtering are, from relatively strong to intermediate, 5000, 3000, 1000, 300, 200 and 100 pA respectively. The sputtering time was adjusted to the type of material, e.g. a harder material will require longer sputtering time to achieve the same effect as in a softer material. Both the ion currents and sputtering times in the FIB microscope are controlled by the *Xpert 2.25* software. A particular function within the software that is frequently used for FIB-section preparation is the milling-scripts that are automated for initial bulk-milling operations (as opposed to fine-thinning operations which must be performed manually).

The milling procedure for obtaining a FIB-section involved three operations (and their associated ion currents): bulk-milling (~5000 pA), partial freeing (~300 pA) and final-thinning (~100 pA). At its start a layer of platinum strip is deposited above an area of interest to protect it from damage during subsequent milling operations. Figure 29a shows that the strip has a nominal thickness of ~1.3 μm. In addition, its length and width of 30.0 by 2.5 μm adequately covers the envisaged final FIB-section dimension of about 10.0 by 1.0 μm. Note that the 'X' markers were intentionally etched on the platinum strip for image correlation purposes used by the *Xpert 2.25* software to implement the automated scripts. The bulk-milling operation employs a relatively high ion current of about 5000 pA in order to optimise the removal rate of the majority of the material adjacent to the cross-section of interest. Figure 29b shows the resultant FIB-section to-be that is sufficiently 'thin' but, more importantly, the spaces adjacent allows for the next operation – 'partial freeing'. Partial freeing refers to milling regions at the sides and base of the FIB-section in order to 'free' the section from the bulk metal. Figure 29c shows a partially 'free' FIB-section at a tilt angle of 45°; yet, the FIB-section still hinges to the top-edge of the platinum strip that is structurally-supportive for the final-thinning operation. Note that it is essential that milling the sides of the FIB-section is carried out at angles of 6° clockwise on the far right and 6° anti-clockwise on the far left as the

a) 1.3µm thick platinum deposited on surface for protection during milling

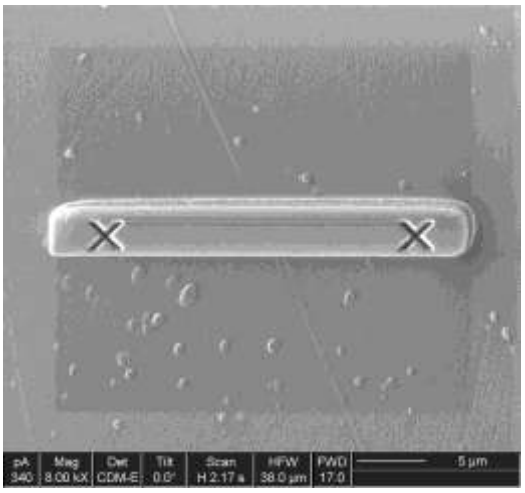

b) initial milling at high currents producing a thick sample

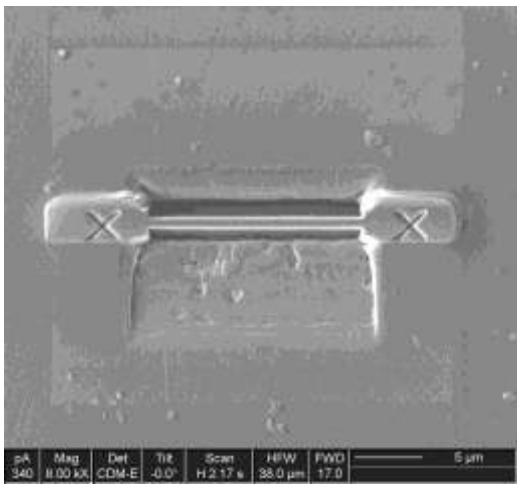

c) tilted 45° for cutting the ‘sides’

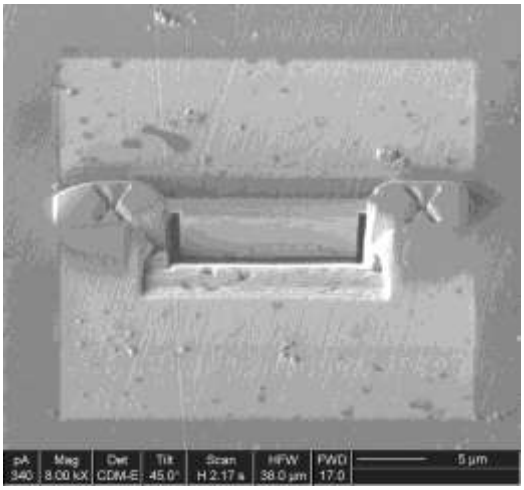

d) final milling to 1.0µm thick

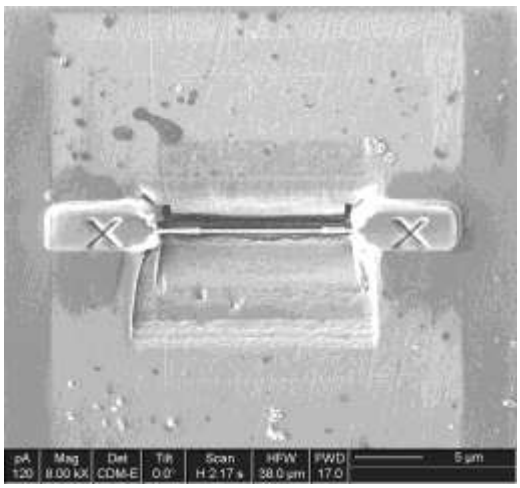

e) grain-structure revealing thin section

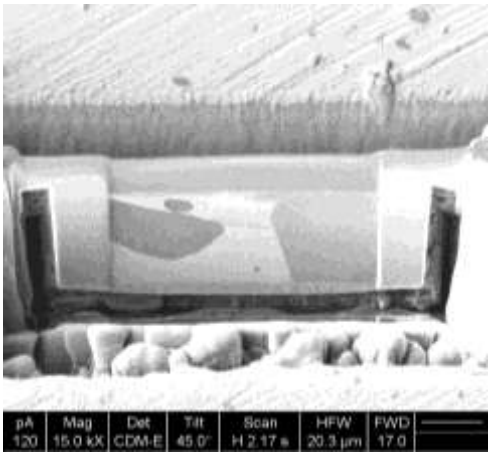

f) thin-section as seen in TEM

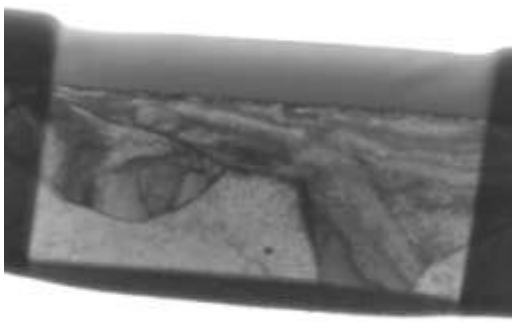

Figure 29 – FIB cross-section preparation for TEM analysis

section gradually expands due to internal stress relief throughout the final-thinning operation. Subsequently, final-thinning is carried out at ±0.8° on the front and back faces of the FIB-section respectively at intermediate ion beam currents of 100 pA until an approximate thickness of 1.0 μm as shown in Figure 29d. Figure 29e reveals its grain structure when tilted at an angle of 45°. At this thickness electron transparency is generally attained but on occasion settling within a sensible range of thickness is allowable where the lack of electron transparency can still be compensated with a higher acceleration voltage in the TEM. It is, however, paramount to take precautions against distortion of the FIB-section during the final thinning operation. Potential causes of distortion are: added weight on, and artificial stresses in, the FIB-section arising from the re-deposited materials as a result of over-milling or mis-focused milling; unbalanced alternation of milling sequence at the front and back faces of the FIB-section; and lack of surface flatness of the sample which causes biased milling rates across the section.

FIB-sections were retrieved from the crater and transferred to the TEM grid (Type: S162A3H Formvar/Carbon 300 mesh Au-25; Agar Scientific Ltd, Stansted Essex CM24 8GF) using the liftout method. The liftout method is schematically illustrated in Figure 30.

FIB-sections were subsequently evaluated in the TEM (Model: JEM2010, S/N: EM13004; JOEL Ltd, Tachikawa, Tokyo 190-0012, Japan). The two aspects evaluated were transmitted-electron, bright-field imaging and scanning-EDX chemical composition analysis. Both analyses were operated at an accelerating voltage of 200 kV with the FIB-section stage at the eucentric height. At eucentric height the electron-beam focus does not change laterally while tilting the sample as a 15°-tilt is necessary to maximise X-ray count whilst acquiring scanning-EDX data). For imaging, the contrast of the FIB section arises due to the differences in the phase of the electron waves that are transmitted through the thin specimen. The transmitted electron images were acquired from the CCD camera (Mulltiscan Model 794; S/N: 04080601; Gatan GmBH, München D-80807, Germany). The TEM was equipped with a scanning-energy dispersive x-ray detector (Model X-Max; S/N: 55355; Software: INCA; Oxford Instruments Ltd, Abingdon, Oxfordshire, OX13 5QX) which was used to quantify the chemical composition of the grains, grain boundaries,

a) A micromanipulator-controlled fine-needle approaching the FIB-trench

b) FIB-section electrostatically attached to the needle

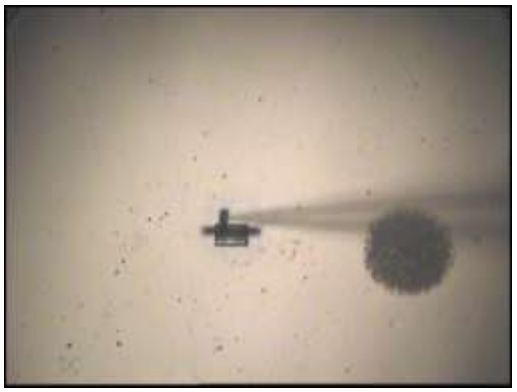

c) FIB-section lifted away from the trench

d) FIB-section and needle approaching a TEM-grid

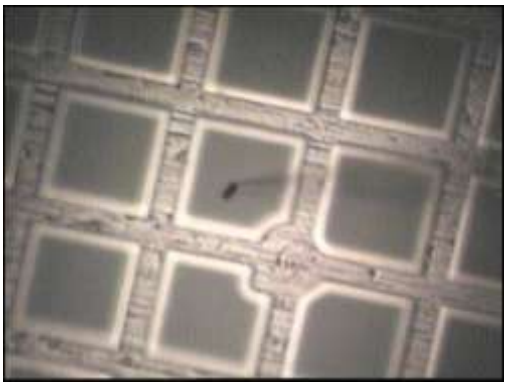

e) FIB-section electrostatically attached on the TEM-grid

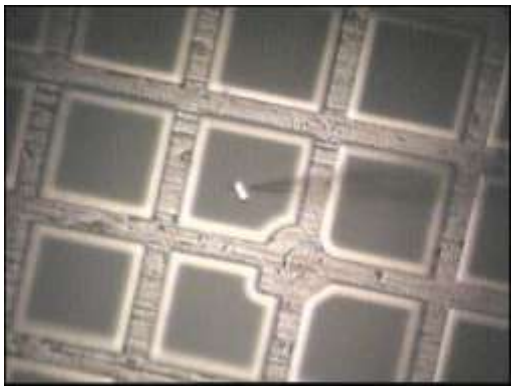

f) needle removed and FIB-specimen is ready for TEM analysis

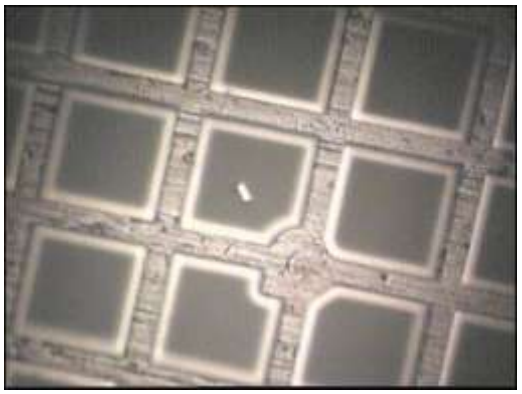

Figure 30 – Lift-out procedure for transferring a FIB-section to TEM grid

and across secondary phases of the FIB-section. The scanning beam probe size was 20 nm and the energy-range quantified is 0-20kV. The analysis is optimised by using an iron-K_α line calibration for each sample and performing the analysis at a tilt angle (θ) of 20° as recommended by the manufacturer.

3.5 Microstructural Characterisation

As a concluding analysis, the post-polarised working electrodes were etched for metallographic examination. Several etchants, shown in Table 11, were investigated for their ability to reveal the distribution of grain structures and secondary phases of the heat-treated austenitic stainless steel 20Cr/25Ni/Nb samples. The etchants preferentially dissolve the higher surface energy sites to provide grain structure contrast. Apart from Kalling's No.2, Vilella's and Marbles which were swab-based etchant chemicals as recommended by Struers Application Note: Metallographic Preparation of Stainless Steel [88], electrolytic-etching with saturated oxalic acid proposed by the Metals Handbook [21] were also evaluated. The latter involves applying a large anodic voltage (note that 6V is relatively large in electrochemistry applications) to the specimen surface in the saturated oxalic acid solution. For this purpose, the three-electrode cell and GPES Potentiostat system (described in Section 3.2) is convenient. The cell's configuration is as follows: the post-polarised sample as the *working-electrode*, platinum *counter-electrode*, silver-silver chloride (Ag|AgCl) *reference-electrode* placed in a Luggin's capillary with about 80 ml. of saturated oxalic acid solution. The GPES software was subsequently used to apply to the working electrode a constant anodic potential of 6V and held for 10s.

Table 11 – Determination of etchant for metallographic examination

Etchant	Composition	Remarks
Kalling's No.2	100mL HCl, 5g $CuCl_2$, 100ml ethanol (95%)	Swab for 3s, 20s and 40s
Vilella's	5ml HCl, 1g Picric Acid, 100ml ethanol (95%)	Swab for 20s
Marbles	10g $CuSO_4$, 50mL HCl, 50ml distilled water	Swab for 3s and 20s
Oxalic Acid	10g Oxalic acid in 100ml distilled water (saturated solution)	Electrolytically-etch at 6V for 10s according to procedures outlined in Davis [21]

Subsequent to etching, the electrodes were analysed in SEM (same SEM conditions described in section 3.3 for corrosion morphology characterisation) to acquire the SEI images which revealed the distribution of grain structures and secondary phases. The SEI image was processed with the MATLAB code earlier described in section 3.1 (and enclosed in Appendix 1) aimed at resolving the *counts* and average size of the secondary phases which appear as bright pixels in the SEI image. The bright pixels are regions of high average atomic number particles that give a higher variation in number of emitted electrons, thus appearing bright relative to regions of low atomic number. In this case, based on the difference in electron emission from regions of different atomic number, the bright pixels are by and large associated with niobium carbides (NbC) in the electrodes, since niobium precipitates are the primary strengthening particles for the AGR fuel cladding (described in section 2.1). The counts of secondary phases are averaged across three 2000x-magnified SEI images of different sites but within the same electrode to obtain the statistical uncertainty or standard deviation of their distribution.

4.0 Results and Discussion

4.1 Electrochemical Behaviour of Thermally-Aged AGR Fuel Cladding

Figure 31 summarises the absolute electrode potentials of the as-sourced and heat-treated AGR fuel cladding specimens that were measured *during the potentio-dynamic scanning when the current density reached 5.0 mA.cm^{-2}*, abbreviated $E_{5.0}$, in both the electrolyte-NaCl of concentration 0.001M (Figure 31a) and 0.1M (Figure 31b). A current density of 5.0 mA.cm^{-2} was selected as the analysis benchmark due to its suitability to compare both electrolyte-NaCl concentrations using the same scales. Averaged across samples from every heat treatment temperature and time, the $E_{5.0}$ values measured were 1.47±0.27V in the 0.001M electrolyte-NaCl and 0.66±0.14V in the 0.1M electrolyte-NaCl. The relatively low $E_{5.0}$ of 0.66±0.14V that has been sufficient to drive the metal dissolution currents up to the 5.0 mA.cm^{-2} mark is due to the high chloride concentrations in the 0.1M NaCl-electrolyte. In contrast the relatively high $E_{5.0}$ of 1.47±0.27V that was required to drive a current of 5.0 mA.cm^{-2} is because of the low chloride concentration in the 0.001M NaCl-electrolyte. The distinct electrode potential ranges – about 800mV per two decades of chloride concentration differences – indicate that lower amounts of chloride ion in the electrolyte decrease the rate at which metal dissolution occurs (e.g., $Cr(s) \rightarrow Cr^{n+} + ne$, $Fe(s) \rightarrow Fe^{n+} + ne$, $Ni(s) \rightarrow Ni^{n+} + ne$). This trend is consistent with Newman *et al.* [8] – who reported for stainless steel 316L a 200mV difference for the same concentration in thiosulphate electrolyte – and others including Galvele [89], Laycock *et al.* [90], Moayed and Newman [91], Soltis *et al.* [64], Smialowska [63] and Williams and McMurray [92] reporting for other metals and electrolyte concentrations. Note that the difference of 800mV is also attributable to the benchmark 5.0 mA.cm^{-2} adopted for analysis which is close to the O_2 evolution regions. At around 1.4V, there exist a rapid rise in currents due to the dissolution of O_2: $O_2 + H_2O + 4e \rightarrow 4OH^-$. Demonstrating a trend consistent with the literature throughout the experimental duration, by means of experimenting with at least two electrolyte-NaCl concentrations as have been employed in this study, provides an empirical gauge of logical corrosion measurements over the many courses of solution preparation, working-electrode fabrication and Luggin's capillary placement in the three-electrode cell.

In addition to the absolute electrode potentials $E_{5.0}$, the percentage values shown at the top of the bar charts in Figure 31 conveniently shows the average percent change in $E_{5.0}$ due to heating time increases, i.e. from 24 to 48h, 48 to 96h and 96 to 192h. The arrow indicates the trends in $E_{5.0}$ changes. The data exhibit both positive and negative changes depending on the heating time transition. A positive change indicates *relative* widening of passive range in the anodic polarisation curves of the electrodes, i.e. improvement in corrosion behaviour. To illustrate, Figure 32 shows the individual polarisation curves from the 700°C samples which constantly exhibit a passive range widening or improvement in the sample's corrosion resistance in response to increasing heating time. At high NaCl concentrations (Figure 32a) the absolute $E_{5.0}$ values were 0.69V, 0.72V and 0.89V – a 13.6% or 200mV compound increase in passive range – corresponding to heating time increase of 48, 96 and 192h respectively. This trend is similar to the measurements at low NaCl concentrations (Figure 32b); the $E_{5.0}$ measured in 0.001M electrolyte-NaCl were 1.38V, 1.57V and 1.63V – a 8.7% or 250mV compound increase in passive range – corresponding to the latter heating time increases. A negative percent change in $E_{5.0}$, on the other hand, is a measure of the *relative* narrowing of the passive range in the anodic polarisation curves or decreasing corrosion resistance of the electrodes as a result of heat treatment. Figure 33 shows the individual polarisation curves of the 500°C samples which consistently exhibit the trend of decreasing corrosion resistance in both electrolyte-NaCl concentrations. The $E_{5.0}$ values measured in the 0.1M electrolyte-NaCl (Figure 33a) were 0.92V, 0.58V and 0.34V – a 63.0% or 580mV compound decrease in passive range – corresponding to a heating time increase of 48, 96 to 192h respectively. Within the same heating times, samples in the 0.001M electrolyte-NaCl (Figure 33b) measured $E_{5.0}$ value decreases from 1.65V, 1.35V and 1.14V – a 29.6% or 510mV compound decrease in passive range.

To compare the trends of corrosion behaviour across all heating temperatures, the percent changes in $E_{5.0}$ for the 24-48h, 48-96h, and 96-192h heating time transitions for the 0.1M electrolyte-NaCl are plotted in Figure 34. In general, heat treatments of up to 96h improve the passive range of the samples (with the exception of the 500°C samples). The averaged percentage increase in electrode potential for the 24-48h heating transition across all heating temperatures is 18.1±10.7%. The successive 48-96h heating transitions shows a further 14.2±6.5% increase averaged

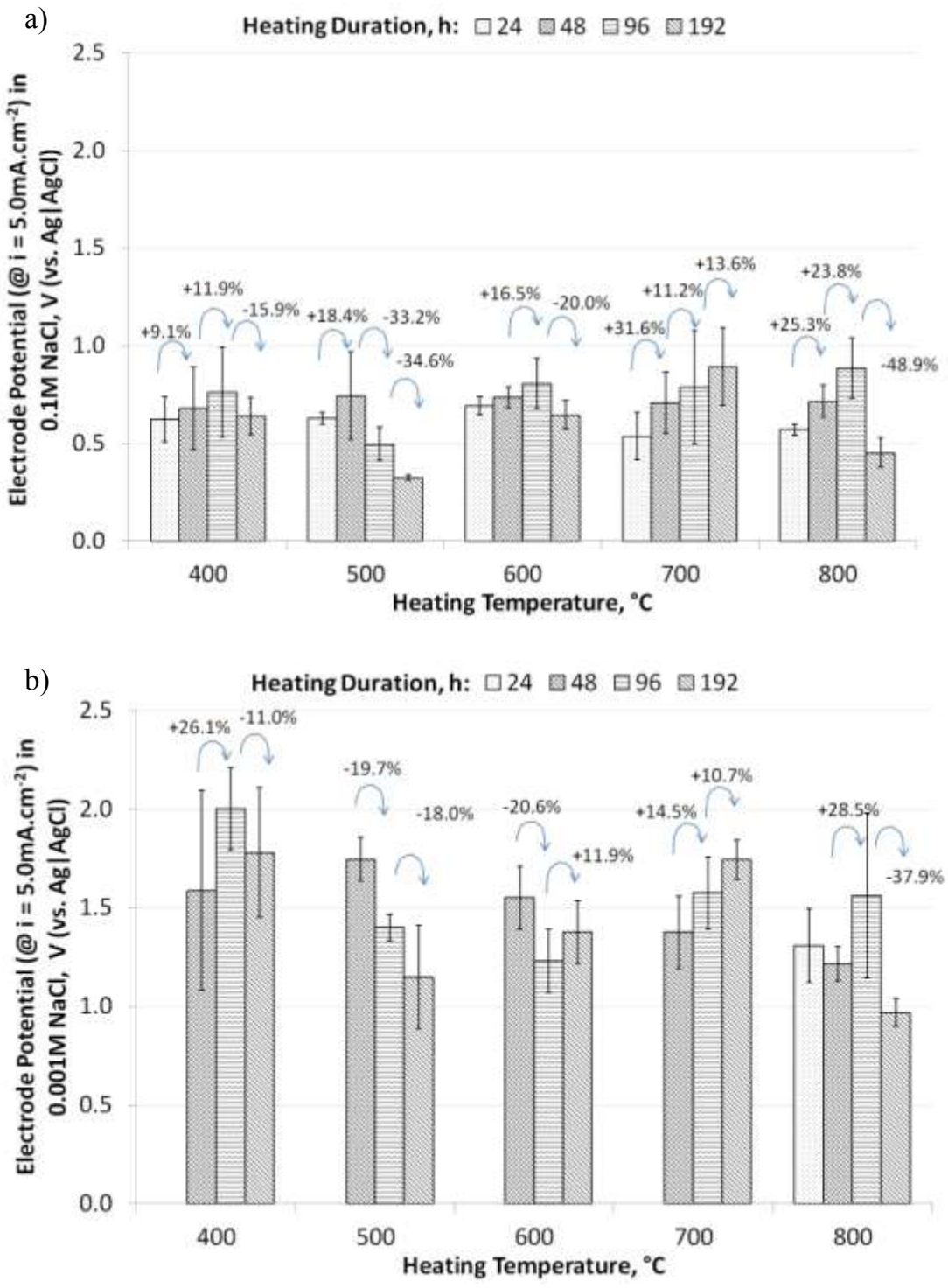

Figure 31 – Electrode potential measurements of the heat-treated samples obtained at benchmark current density of 5.0 mA.cm^{-2} in 0.001M and 0.1M electrolyte-NaCl

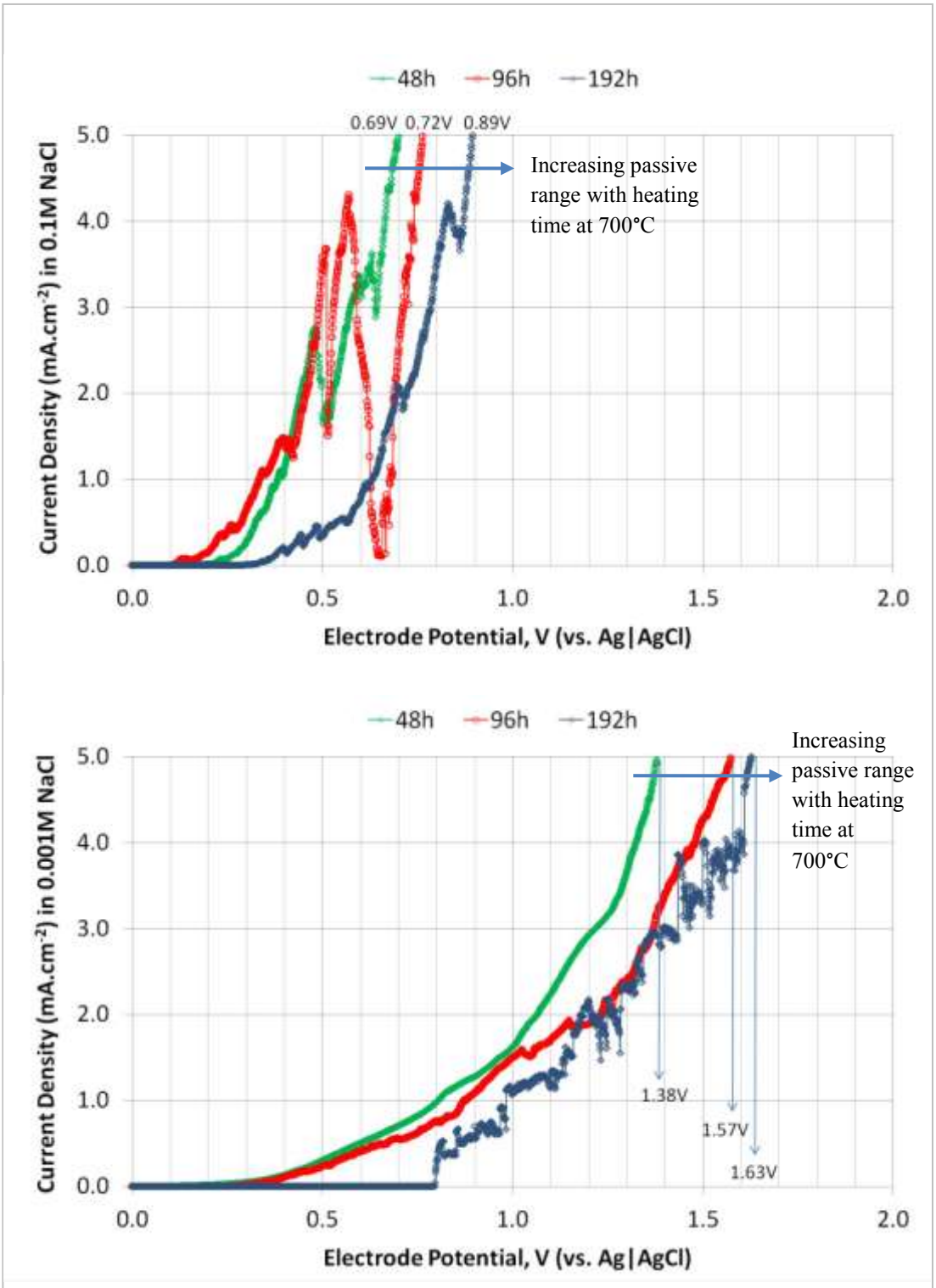

Figure 32 – Anodic polarisation curves for 700°C 48, 96 and 192h heat-heated samples in 0.001M and 0.1M electrolyte-NaCl.

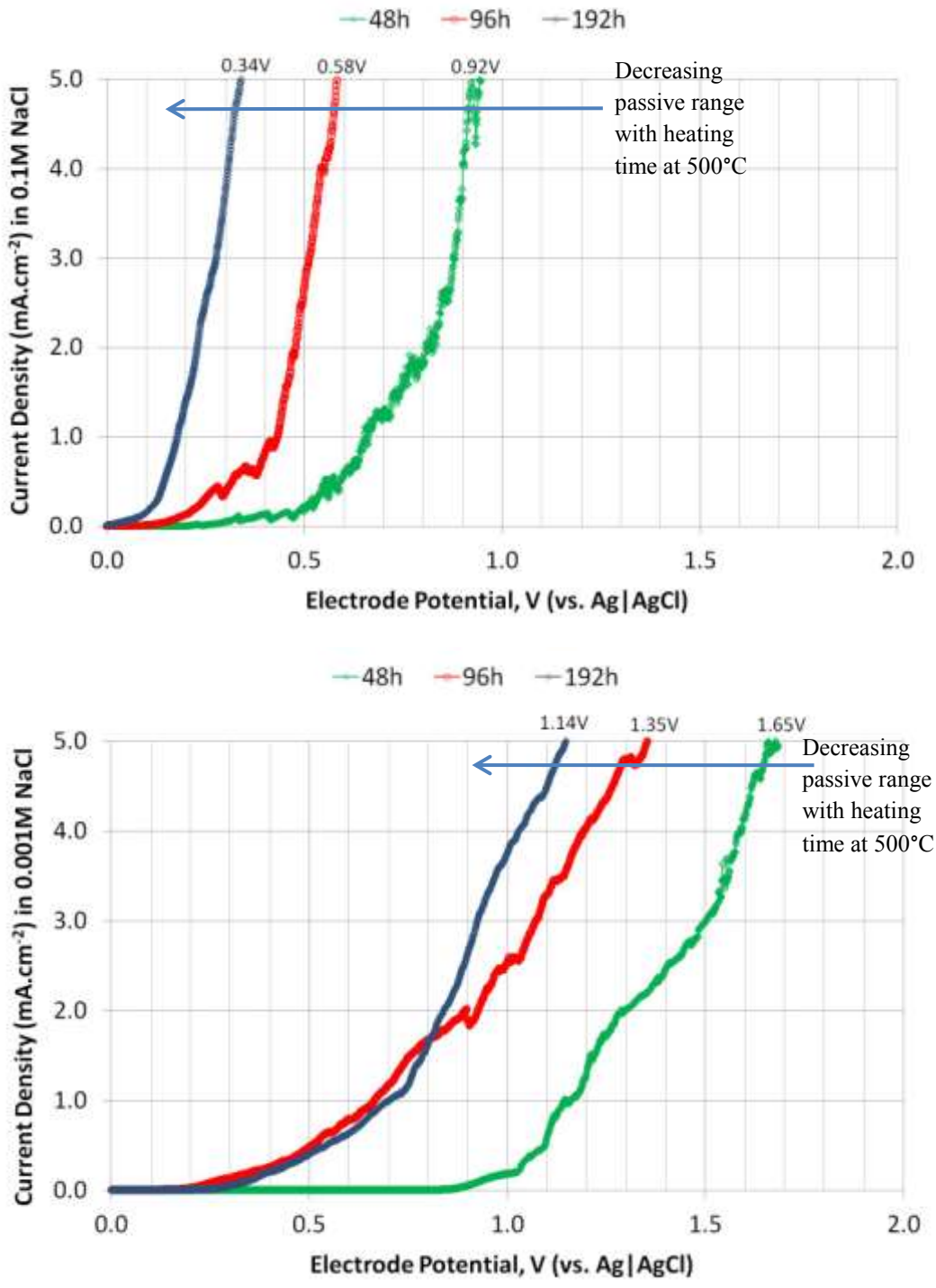

Figure 33 – Anodic polarisation curves for 500°C 48, 96 and 192h heat-heated samples in 0.001M and 0.1M electrolyte-NaCl

across all temperatures (apart from the 500°C samples). Prolonged heating of up to 192h, however, almost always results in a decreased $E_{5.0}$ from its initially increased values over the first 96h of heating; apart from the 700°C samples the 96-192h heating time transition measured a steep, average percent decrease in $E_{5.0}$ values of 29.9±15.0%. Note also that for the 500°C samples the decrease in corrosion resistance has already occurred in the 48-96h heating time transition. The observed changes in corrosion behaviour (variation in the $E_{5.0}$ values) of the specimens can be attributed to the age hardening characteristics (section 2.3.1) that manifest in the heat-treated microstructure, which are characterised by various methods as described in sections 4.2 to 4.5. Specifically, the microstructures which led to the corrosion susceptibility (i.e., 400°C 192h, 500°C 192h, 600°C 192h and 800°C 192h) are characterised and compared to the as-sourced, factory annealed AGR fuel cladding specimens.

Figure 35 shows the absolute $E_{5.0}$ value of the heat treated specimens in the 0.1M electrolyte-NaCl on a time-series plot to examine the effect of heating times on

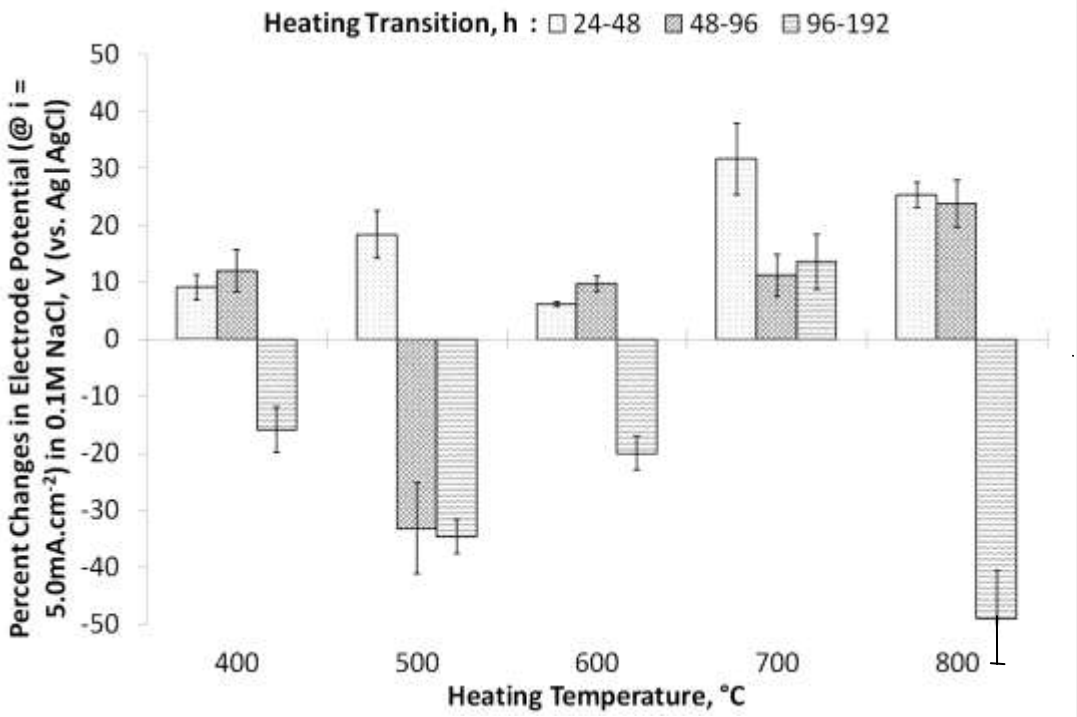

Figure 34 – Percent changes in electrode potential in response to varying heat treatment time for all temperatures

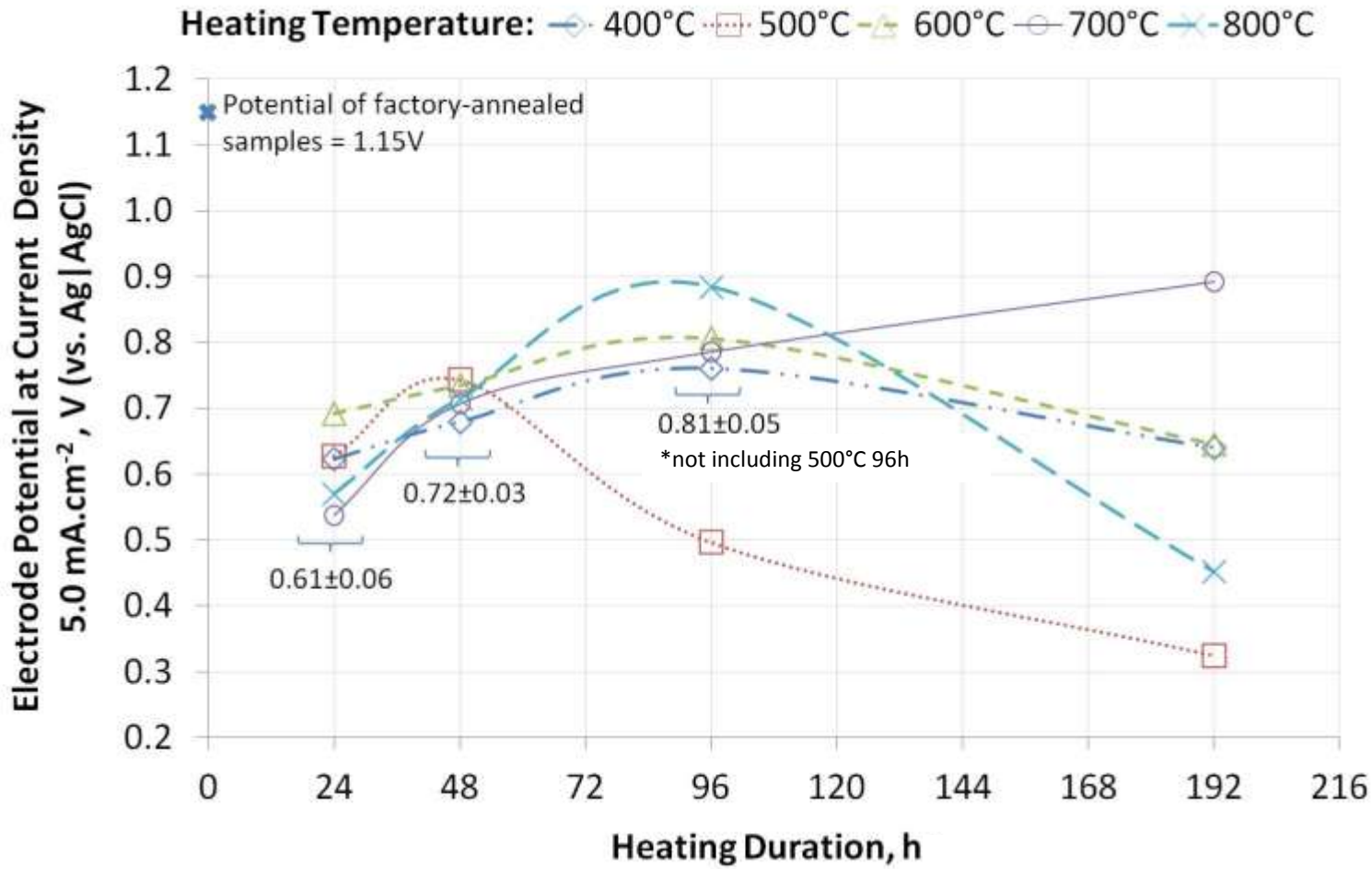

Figure 35 – Electrode potential measured at constant current density of 5.0 mAcm^{-2} as a function of heat treatment time in electrolyte-NaCl 0.1M. Note that the dotted-lines are smoothed-curves.

its corrosion behaviour. Note that the $E_{5.0}$ of the as-sourced, factory-annealed AGR fuel cladding specimens is 1.15V, a high electrode potential which drives a current of 5.0 mA.cm^{-2} due to the sample's optimum corrosion resistance from the manufacturing process. The absolute $E_{5.0}$ values for the 24 and 48h heated samples averaged across all heating temperatures were 0.61±0.06V and 0.72±0.03V respectively, an increase of about 18%. The narrow error-bars exhibited in both averages that are reproducible within 9.9% and 4.5% respectively indicate that for short heating times (i.e., <48h) the heating temperatures employed have not been able to induce a marked difference in the specimens microstructure, hence their similar corrosion behaviours. This notion can be extended to the heating time of 96h (if the 500°C specimens are excluded from the analysis) in which case the absolute $E_{5.0}$ values averaged across all other temperatures was 0.81±0.05V – a value reproducible within 6.2%. The 500°C 96h heated samples, however, measured $E_{5.0}$ value of 0.5V which is a steep decrease from the 48h heating time at a rate of -0.59% h^{-1} (28.3%/48h). The prolonged heating time of 192h shows a wide range of $E_{5.0}$ values, which indicates temperature-dependent microstructural changes. Whilst the 700°C samples showed a marginal improvement in $E_{5.0}$ value from the previous heating times, all other treatment temperatures revealed a decrease. The 800°C samples, in particular, exhibit the sharpest decrease in $E_{5.0}$ at a rate -0.52% h^{-1} (48.3%/96h). The 500°C 192h samples exhibit the lowest $E_{5.0}$ value in this study at 0.34V, i.e., the least corrosion resistance with performance about 810mV relative to the factory-annealed value of 1.15V.

As a summary this section shows the corrosion measurement results from the heat-treated and as-sourced AGR fuel cladding samples that had their electrode potentials measured at the current density of 5.0 mA.cm^{-2}, $E_{5.0}$. $E_{5.0}$ is an expression of passive range; a comparatively smaller value indicates the sample's corrosion susceptibility to the other since that value is already enough to drive a dissolution current to 5.0 mA.cm^{-2}. Averaged across samples from all heating temperature and time, the $E_{5.0}$ values are 1.47±0.27V and 0.66±0.14V in electrolyte-NaCl 0.001M and 0.1M respectively – about 800mV difference per two decades of chloride concentration. High chloride concentration adversely impacts AGR fuel cladding corrosion and therefore should be kept to a minimum in the *Receipt and Storage Ponds*. Within both electrolyte concentrations, $E_{5.0}$ exhibit a consistent trend of

variability across the heat treatment matrix employed in this study (temperatures: 400°C to 800°C, times: 24 to 192h). This suggests that the AGR fuel cladding which operates over a gradient of similar temperature ranges across its 1m length may consist of areas of different corrosion susceptibility, certainly more profoundly if also coupled to effect of radiation damage. Generally, the $E_{5.0}$ values increase over the first 96h of heating (annealing effect) but deteriorate when the sample is further heated to 192h (Figure 34). In particular, heating temperatures of 500°C and 800°C produce samples of the highest magnitude and percent decrease in $E_{5.0}$ values (Figure 34). The next section shows their corrosion morphologies from the post-polarised electrodes and attribution of the deteriorated $E_{5.0}$ values to specific microstructure that results from the heat treatment matrix employed. In particular, the 500°C 192h and 800°C 192h samples, and in comparison to the 600°C 192h and as-received samples, are extensively examined to elucidate the critical microstructural features that affect its corrosion behaviour. These samples have average $E_{5.0}$ values, respectively, of 0.34V, 0.45V, 0.65V and 1.15V.

4.2 Corrosion Morphologies of Post-Polarised Electrodes

This section of the thesis examines the corrosion morphology of the post-polarised electrodes in the SEM. Figure 36 compares at low magnification a series of electrode surface conditions that exhibit an increasing tendency of crevice corrosion between the as-received, 500°C 96h, 500°C 192h, and 800°C 192h electrodes that register $E_{5.0}$ electrode potential values of 1.15V, 0.65V, 0.45V and 0.34V respectively. For the as-received electrode (Figure 36a) the interface between the steel and resin remains 'seamless'. This observation parallels the expectation that the as-manufactured metal should possess a good level of corrosion performance; a relatively high electrode potential of 1.15V is required to drive the metal dissolution currents up to the 5.0 $mA.cm^{-2}$ mark. In stark contrast the electrode from the 800°C 192h heated cladding specimens (Figure 36d), i.e., the highest heating temperature and duration employed in the thermal-aging treatment, exhibited appreciable crevice corrosion between the steel-resin interface and pitting corrosion on the bulk metal's surface. This observation suggests that the corrosion resistance afforded by the as-received cladding has been diminished due to the heat treatment; an electrode potential of only 0.30V has raised the metal dissolution current to a level of 5.0 $mA.cm^{-2}$ or 74% lower electrode potential than the as-received electrode. The microstructural and chemical features that distinguish their corrosion susceptibility are reported in Sections 4.3 and 4.4. The other electrodes, given intermediate heat-treatment temperatures and times of 500°C 96h (Figure 36b) and 500°C 192h (Figure 36c), show intermediate degrees of corrosion between the as-received and 800°C 192h electrodes.

Another observation with regard to the corrosion susceptibility of these electrodes is the proportional decrease in the electrolyte solution's opacity in the three-electrode cell containing the dissolved metal ions from the anodic dissolution processes. Figure 37 compares qualitatively the electrolytes opacity containing dissolved metal ions from the electrodes. For the as-received sample (Figure 37a) the electrolyte solution remains virtually transparent and clear. For the 400°C and 600°C 192h samples the solution became 'murky' (Figures 37b and 37c). For the 500°C 96h, 500°C 192h and 800°C 192h electrodes their electrolyte solution shown in Figures 37d, 37e and 37f respectively are highly sedimentitious. Therefore on a

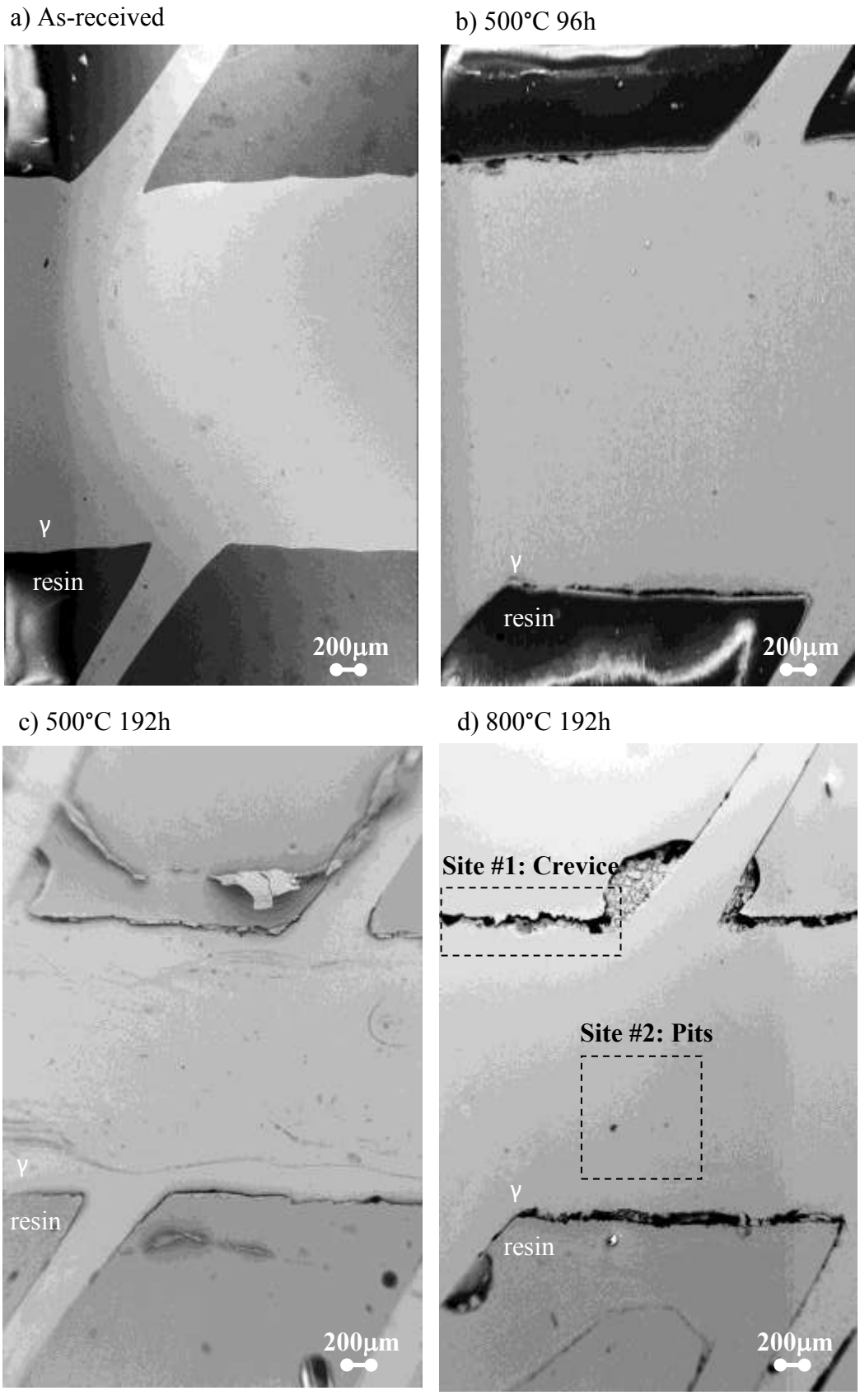

Figure 36 – Surface conditions of post-polarised working electrodes

a) as-received

b) 400°C 192h

c) 600°C 192h

d) 500°C 96h

e) 500°C 192h

f) 800°C 192h

Figure 37 – Opacity of electrolyte solution containing dissolved metal ions

preliminary, qualitative basis there is evidence of increased corrosion susceptibility due to thermal-aging of the cladding specimen as indicated by both the increasing concentrations of pits (discussed in detail later in Section 4.4) and crevices and the proportional decrease in electrolyte solution opacity which contains the dissolved metal.

Site #1 and Site #2 (labelled in Figure 36d) from the 800°C 192h electrode were analysed in detail.

Figure 38 shows three micrographs from Site #1 illustrating its crevice corrosion morphology. Figure 38a shows a deep, ~ 100 μm wide crevice between the steel-resin interface which contrasts the marked corrosion susceptibility of the electrode compared to the 'seamless' interface in the as-received electrode. The metal portion along the crevice exhibits some lace-like corrosion (a lacy corrosion cover). Figure 38b utilised a tilt-angle of 70° to examine the morphology beneath the lacy corrosion cover, albeit with a restricted view. The area beneath the cover extends to a much wider, deeper region. The pit bottom exhibits a smooth surface which indicates that the corrosion process is diffusion controlled as suggested by Galvele [61] (Section 2.5). This micrograph in particular also reveals the metal scales that have collapsed to the pit bottom. At higher magnification (Figure 38c) traces of salt crystals, e.g sodium chloride (NaCl), were seen to have deposited on the surface of these metal scales.

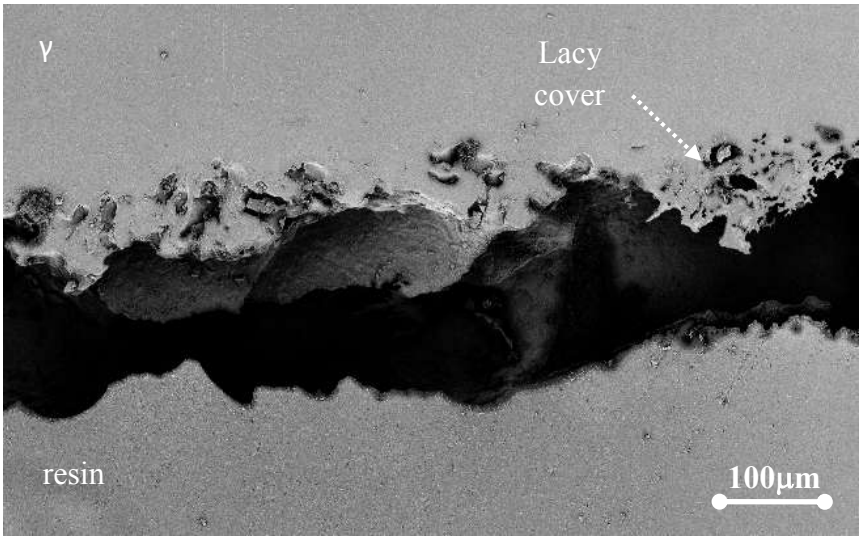

a) Site #1, imaged at θ = 0°

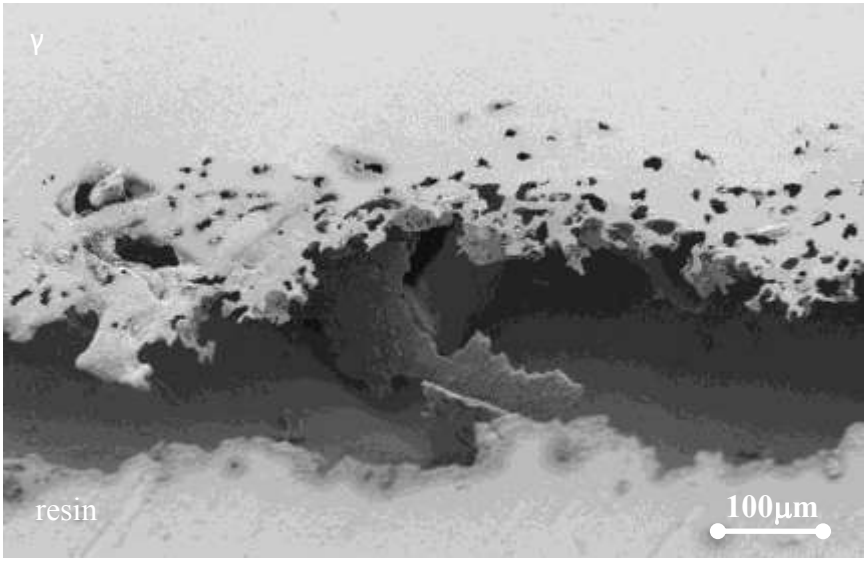

b) Site #1, imaged at θ = 70°

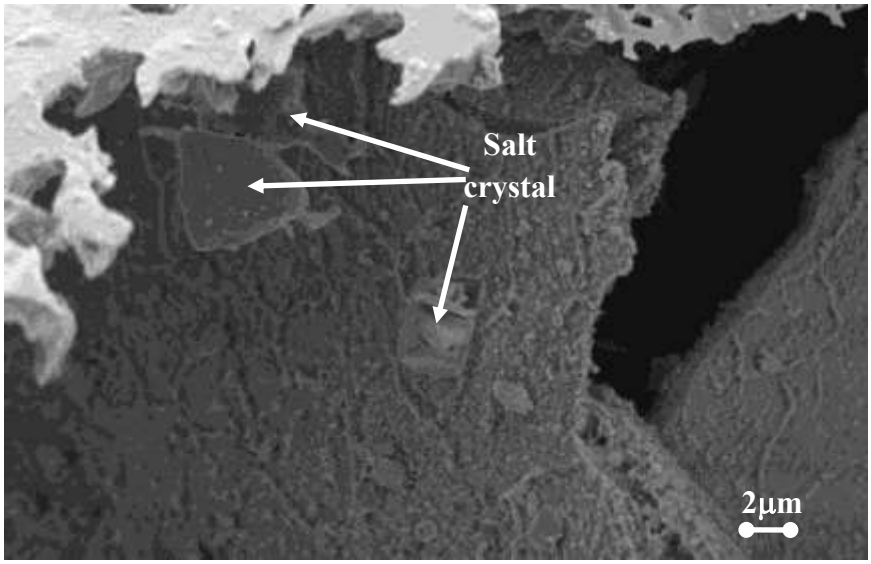

c) close-up of micrograph b)

Figure 38 – Crevice corrosion on 800°C 192h post-polarised electrode

Considering pitting corrosion morphologies, Figure 39 shows a high magnification image of Site #2 from Figure 36d which reveals three forms of pitting corrosion. They include: pitting accompanied by a lacy corrosion cover adjacent to an inclusion, determined to be niobium-carbide (NbC), Figure 39a; pitting *without* visible lacy corrosion cover that also occurs around an inclusion, Figure 39b; and open pits with a concave geometry that are freely exposed to the bulk environment, Figure 39c. Figure 39a shows two examples of pitting corrosion morphology associated with a lacy corrosion cover that is evolving around an inclusion. In the left micrograph, the lacy cover is ~12 μm wide around a rectangular-shaped ~10 by 2 μm NbC particle. The right micrograph shows a larger lacy corrosion cover ~30 μm diameter that is evolving around an angular (4 by 4 μm) NbC particle. Figure 40 shows a compilation of lacy corrosion covers from other electrodes, with details of heat treatment given in the caption, to illustrate their size ranges, even though there is no trend between cover size and heat treatment. Most of the lacy corrosion covers bend over the surface plane due to their width and weight. At some stage, this is potentially followed by collapse into the bottom of the pit. These morphologies suggest that pit acidification processes are potentially *maintained by the lacy corrosion cover* as suggested by Ernst *et al.* [55, 66, 76] and that the acidification process stops as the cover is mechanically detached from the bulk metal. Note that the geometry of these NbC inclusions is well maintained even though extensive corrosion has occurred around them, suggesting that it *acts as a cathode* and is relatively stable to the matrix. Figure 39b shows two other examples of pitting corrosion that do not exhibit a lacy metal cover but that occurs around NbC inclusions. Figure 39c shows two examples of stabilised pits consisting of neither lacy corrosion cover nor inclusions. The left figure shows a stabilised twin-pit feature measuring about 16 μm wide whereas the right figure shows a stabilised hemispherical pit (~10 μm wide) that contain remnants of metal that may have originated from a pre-existed lacy corrosion cover.

a) lacy corrosion cover-type of pitting adjacent NbC inclusion

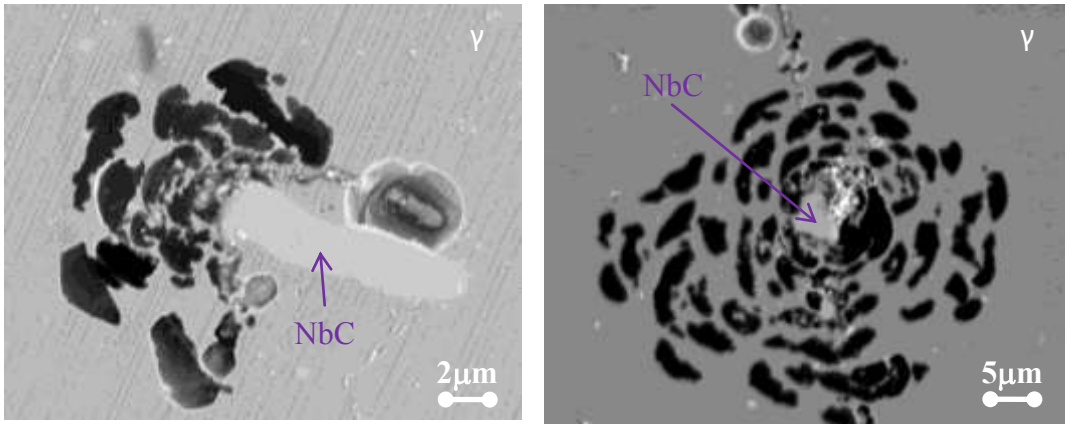

b) pitting corrosion adjacent NbC inclusion

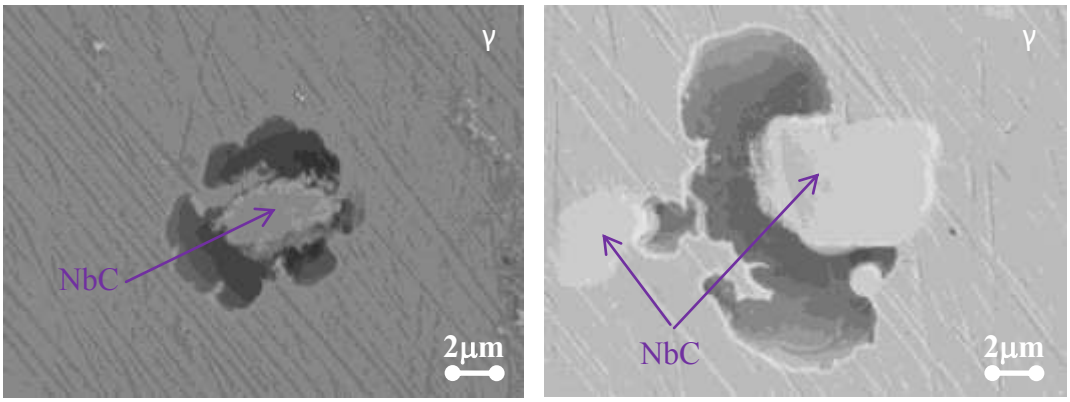

c) stabilised pits with concave geometry that is freely exposed to bulk environment

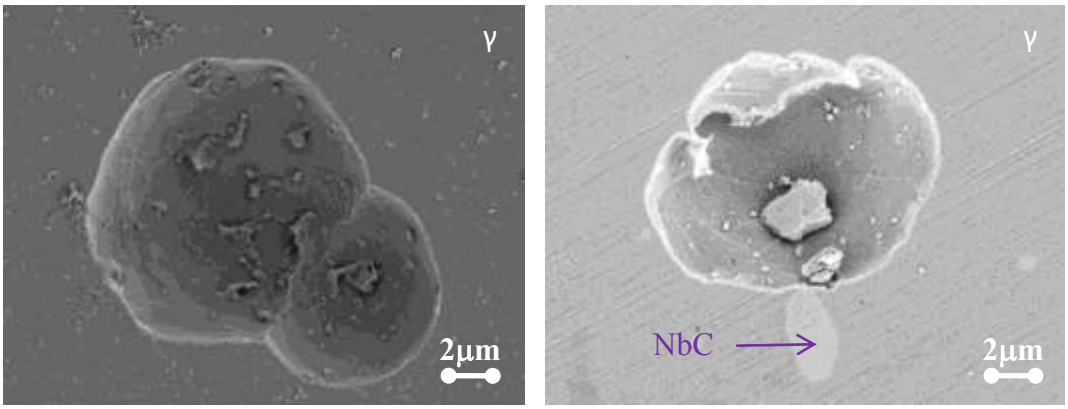

Figure 39 – Occurrences of pitting corrosion in the post-polarised 800°C 192h post-polarised electrode

a) 400°C 192h (~15 µm dia.)

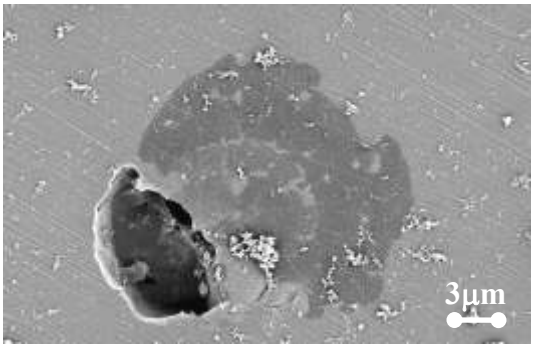

b) 400°C 192h (~10 µm dia.)

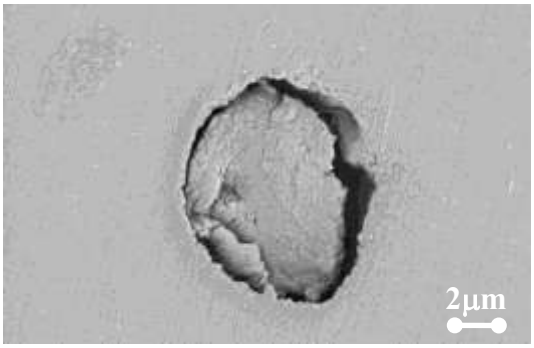

c) 500°C 192h (~5 µm dia.)

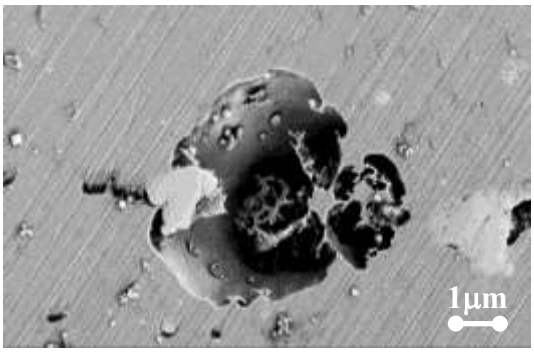

d) 500°C 192h (~25 µm dia.)

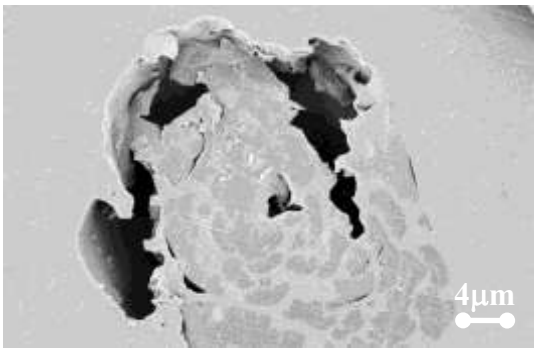

e) 600°C 192h (~10 µm dia.)

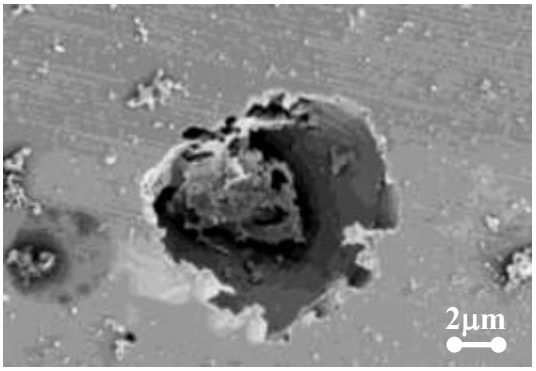

f) 600°C 192h (~12 µm dia.)

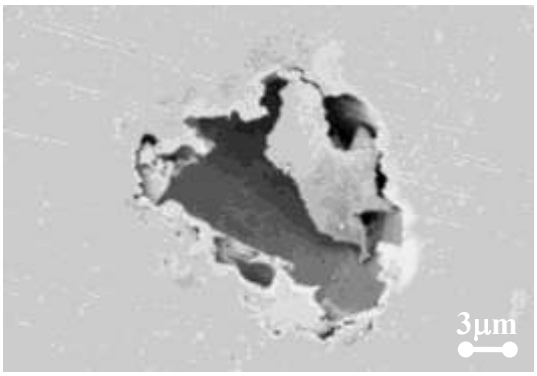

g) 700°C 192h (~12 µm dia.)

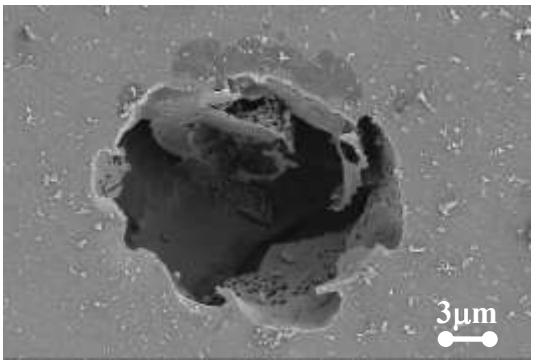

h) 700°C 192h (~5 µm wide)

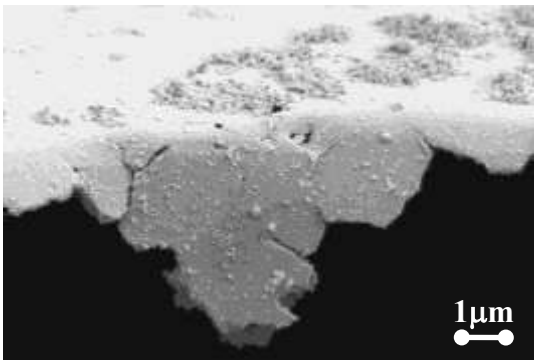

Figure 40 – Typical size and feature of lacy corrosion covers

Figures 41 to 43 show the results from two techniques – interferometry and FIB milling as detailed in Section 3.3 – employed to profile the subsurface geometry of the observed pits and crevices. Figure 41 shows the width and depth measurement of a pit using an interferometer. The left micrograph in Figure 41a shows a pit that was imaged under the SEM whereas the right micrograph shows the corresponding pit that was tracked and analysed under the interferometer. Figure 41b shows two orientations of the resulting 3-D topography image which indicates the flexibility of this method to study the surface roughness and varied depths across the bottom of the pit. This particular pit is 23.0 μm wide by 14.5 μm deep giving a width-depth ratio of ~1.6.

Figure 42 explores the pit geometry of another site using the FIB-milling capability. In Figure 42a material adjacent to the site was removed by milling to provide sufficient clearance to enable the features at the pit to be characterised at a tilt angle of 45°. Figure 42b revealed the pit was 21.5 μm wide by 8.1 μm deep, yielding a width-depth ratio of ~2.6. The micrograph also illustrates the highly porous structure of the lacy corrosion cover and smooth concave nature at the pit bottom which may be stable to further corrosion.

Figure 43 is an attempt to use the FIB-milling technique to characterise the subsurface geometry of a crevice. Figure 43a shows a ~160 μm wide crevice site. Figure 43b shows a rectangular strip along the metal portion of the site that was milled to provide clearance for subsurface examination. Note that the brighter resin contrast in this image is indicative of the metal layer that is re-deposited on the resin surface from the milling process. Figure 43c, however, indicates that the crevice extends to a much greater depth beneath the visible regions which restricts the crevice geometry profiling and also observation of its full morphology. Nonetheless this micrograph reveals that the crevice exhibits *several layers* of lacy corrosion cover.

a) Secondary electron and interferometer images of Figure 44g

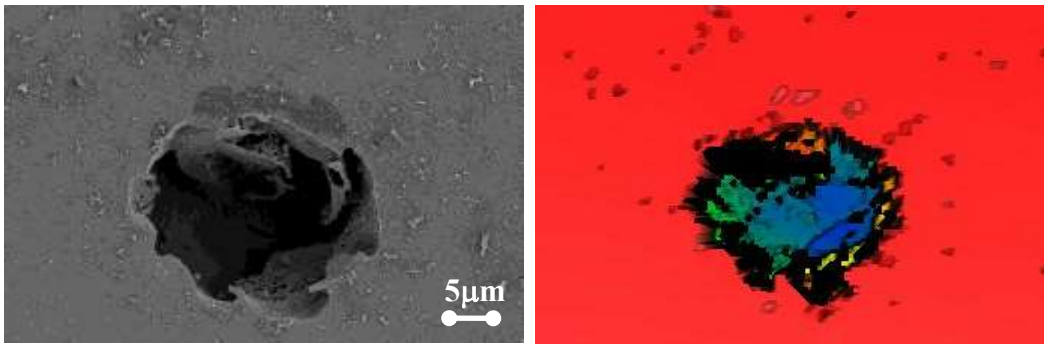

b) Two orientations of 3D-topography image

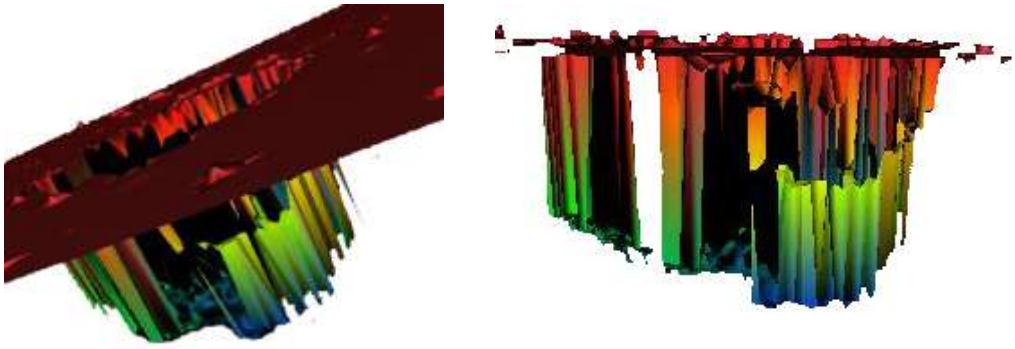

c) Width and depth profiling

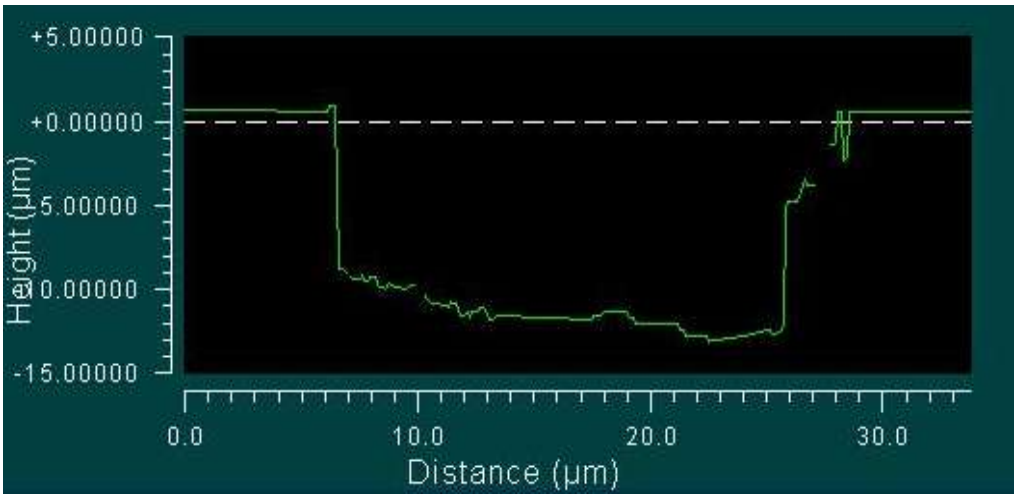

width: 6.5 – 29.5µm
depth: -13.5 – 1.0 µm
width/depth ratio: 1.6

Figure 41 – Depth profiling of 600°C 192h sample with interferometers

a) start of bulk milling, image obtained at θ = 45°

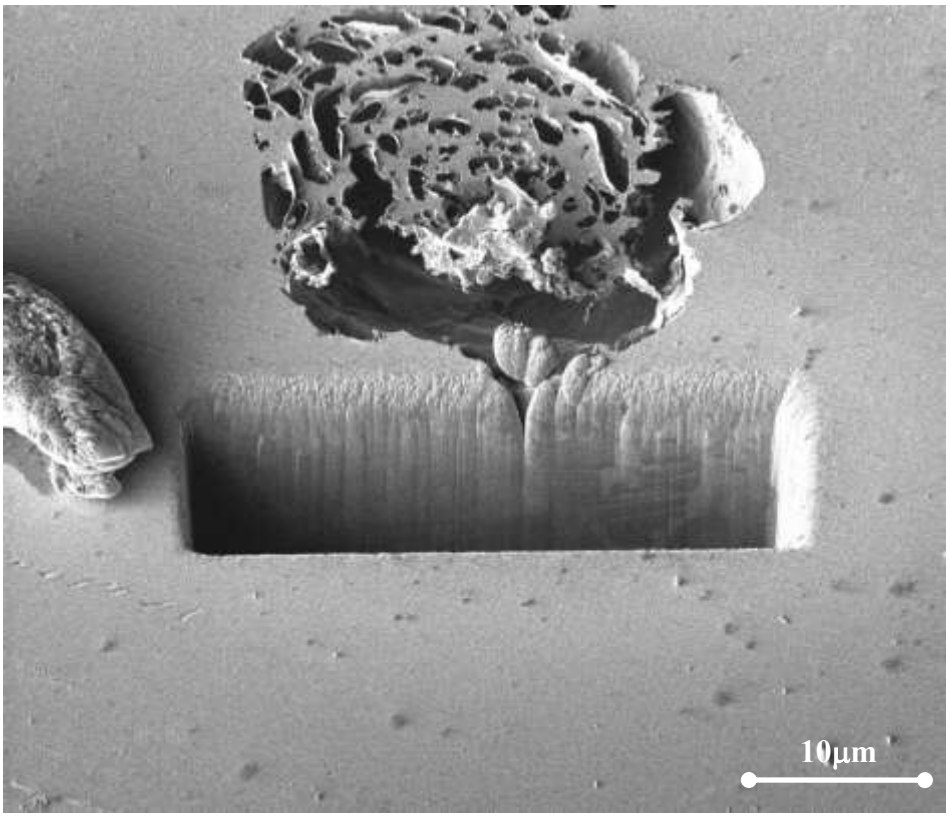

b) bulk milling approaching middle of pit, image obtained at θ = 45°

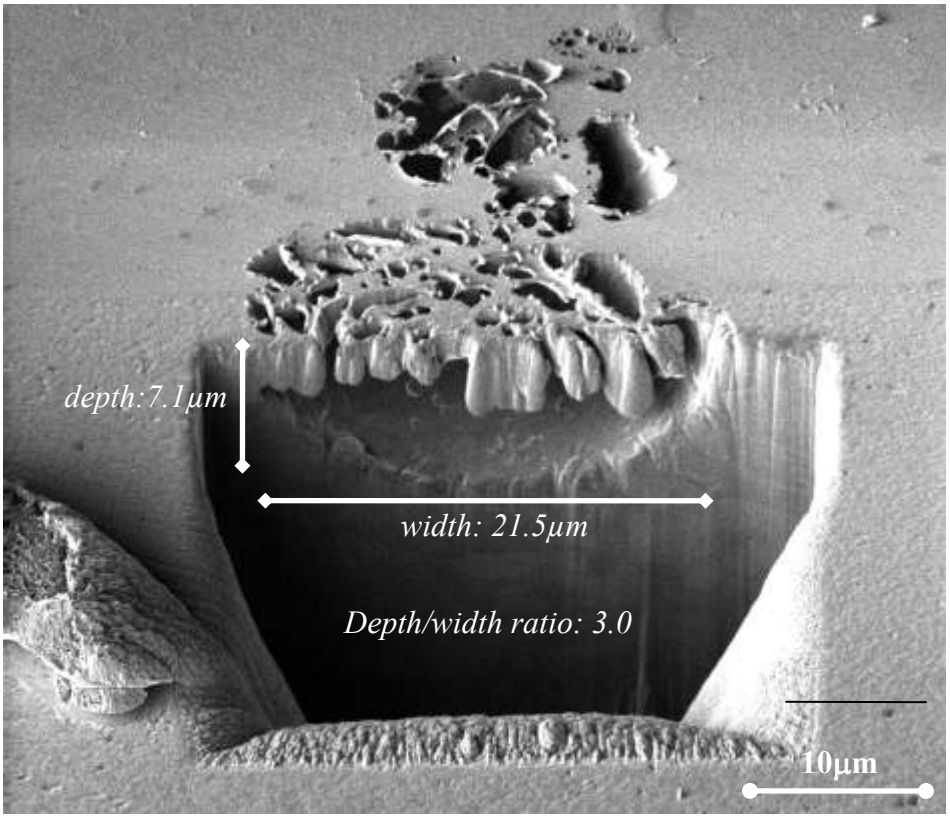

Figure 42 – Subsurface geometry characterisation of pit using FIB on 500°C 192h sample

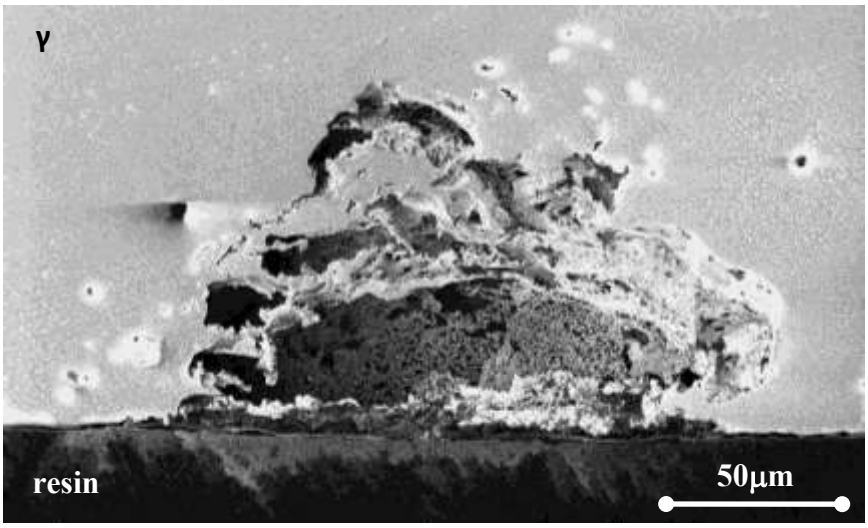

a) crevice site

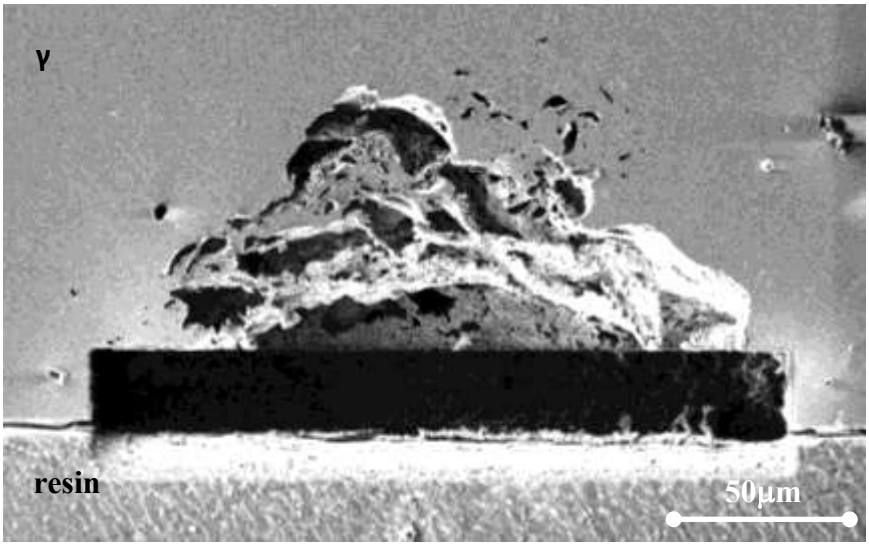

b) FIB ion milling

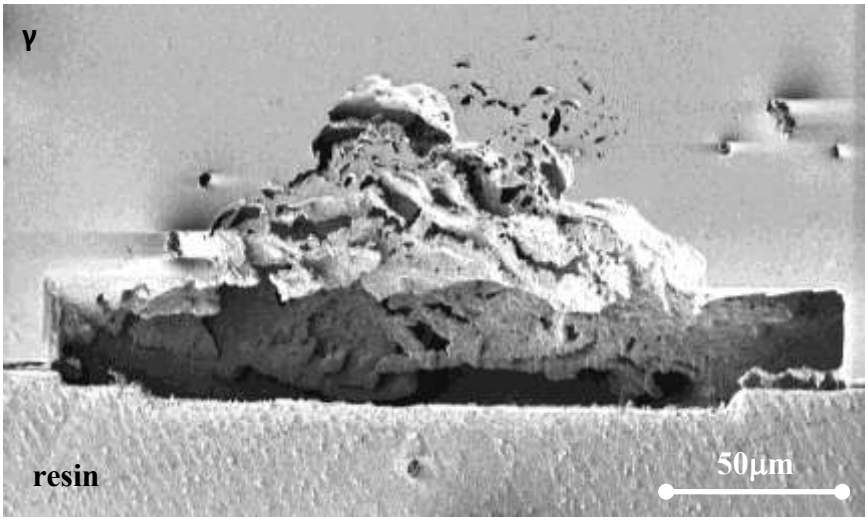

c) imaging at tilt angle of 35°

Figure 43 – Subsurface geometry characterisation of crevice using FIB on 500°C 192h sample

Figure 44 shows FIB characterisation of one of the most-corroded electrodes, the 800°C 192h sample, to indicate the extent and magnitude of microstructural changes arising from subsurface pitting and corrosion. The large micrograph shows a large lacy corrosion cover ~200 μm from the 'centre', although only a portion of the whole cover is shown in Figure 44. Two sites labelled Site #3 and #4 (situated about 300 and 150 μm from the 'centre' respectively) were intended for FIB cross-section characterisation. However, as shown in the magnified micrographs of Site #3 and #4, the regions below the lacy corrosion covers are by-and-large voids. It is reasonable to expect that a much larger network of corrosion remnants exist underneath the surface of the metal cover and that it extends beyond the 'centre'.

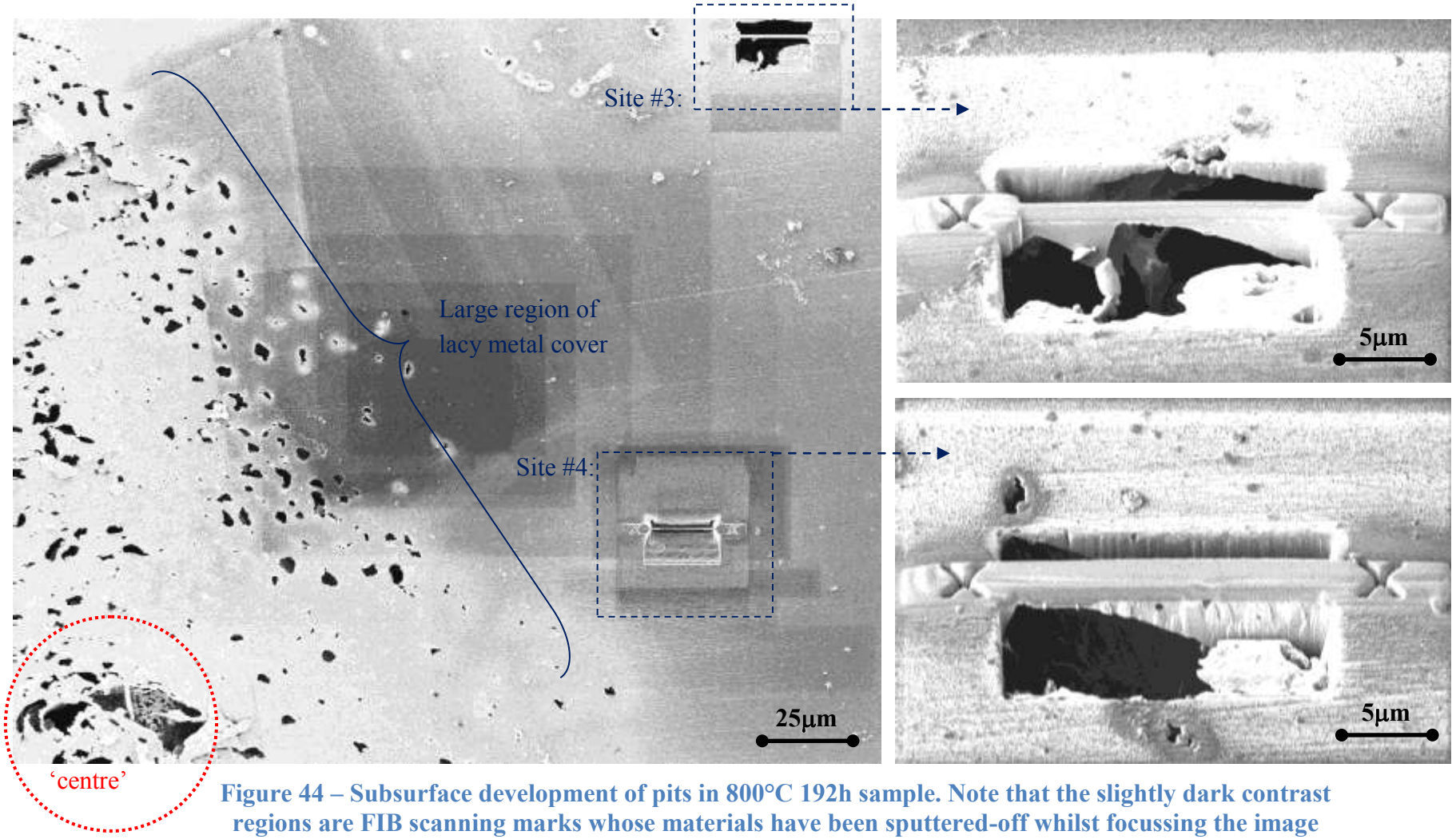

Figure 44 – Subsurface development of pits in 800°C 192h sample. Note that the slightly dark contrast regions are FIB scanning marks whose materials have been sputtered-off whilst focussing the image

On a related matter, in order to analyse the salt crystals formation that has been observed in Figure 38c, an additional experiment was performed to characterise another 500°C 96h post-polarised electrodes retrieved from the electrolyte solution in the three electrode cell but let dry under ambient conditions so not using the normal sample handling protocol involving rinsing by a jet of water. Figure 45 shows salt crystal deposits on the surface of the unrinsed, post-polarised electrode that were concentrated at the metal-resin interfaces and throughout the metal surface. Sites #5, #6 and #7 were analysed more closely to characterise the salt deposit morphologies. Figures 46a and 46b are higher magnification images of Sites #5 and #6 respectively which show high concentrations of salt deposits crystallised along the metal-resin interfaces. Figure 46a, in particular, shows that the salt deposits are *least* concentrated above the area in which the lacy corrosion cover appears most intense. On the other hand, Figures 46c and 46d, higher magnification images of Site #7, suggests that these salt crystals are adherent rather than chemically-absorbed on the metal surface as indicated by the 'detached' salt deposit feature. These preliminary observations suggest that the effects of salt crystallisation may potentially be important in metal dissolution processes and that one of the future work should focus on the effects of crystallisation stresses imparted on the metal surface and modification of the surface tension by the salt deposits [93].

To conclude this section, the morphologies of AGR fuel cladding corrosion, both crevice and pitting, have been revealed with the post-polarised electrodes. Three common types of pitting corrosion were encountered: (i) pitting accompanied by a lacy corrosion cover (Figure 39a); (ii) pitting *without* visible lacy corrosion cover but which extends to a certain depth beneath the surface plane (Figures 39b and 40); and (iii) repassivated or restabilised pits with a concave geometry that are freely exposed to the bulk environment (Figure 39c). They have a width-depth ratio between 1.6 to 2.6, although their actual size varies locally depending on the site and no correlation to their $E_{5.0}$ values as a result of heating temperature and time have been established. Niobium carbide precipitates have a significant role in cladding corrosion as they are involved in most of the pitting and crevice corrosion morphologies encountered. They may *act as cathode* in the electrochemical corrosion mechanisms due to their relatively well-maintained geometry even though extensive corrosion has occurred around them. The next section shows from TEM

analyses on FIB-prepared cross sections the subsurface corrosion features, including chemical composition analyses, of the post-polarised electrodes.

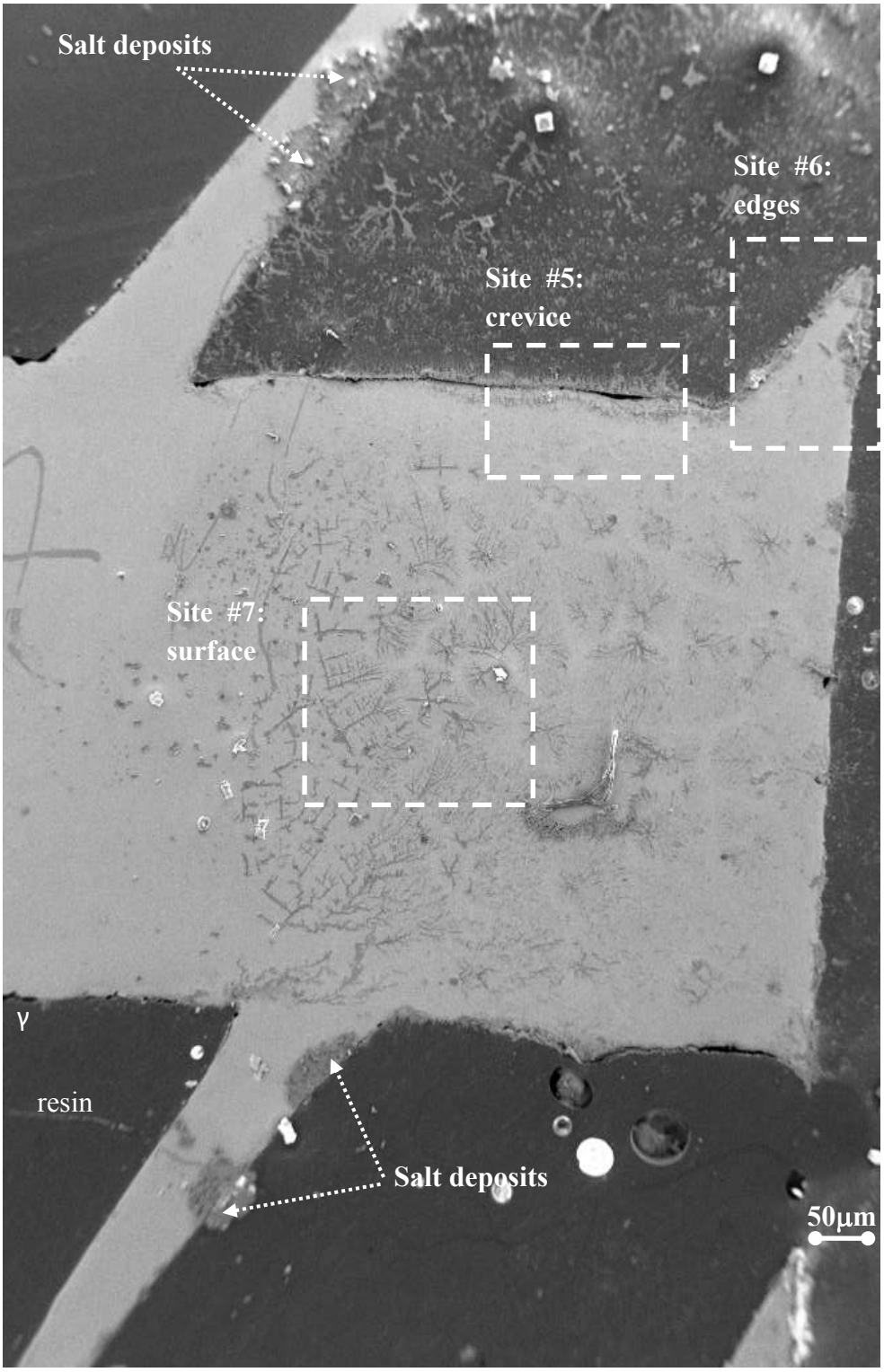

Figure 45 – Salt deposits on the metal-resin interface of the unrinsed, post-polarised 500°C 96h heat treated electrode

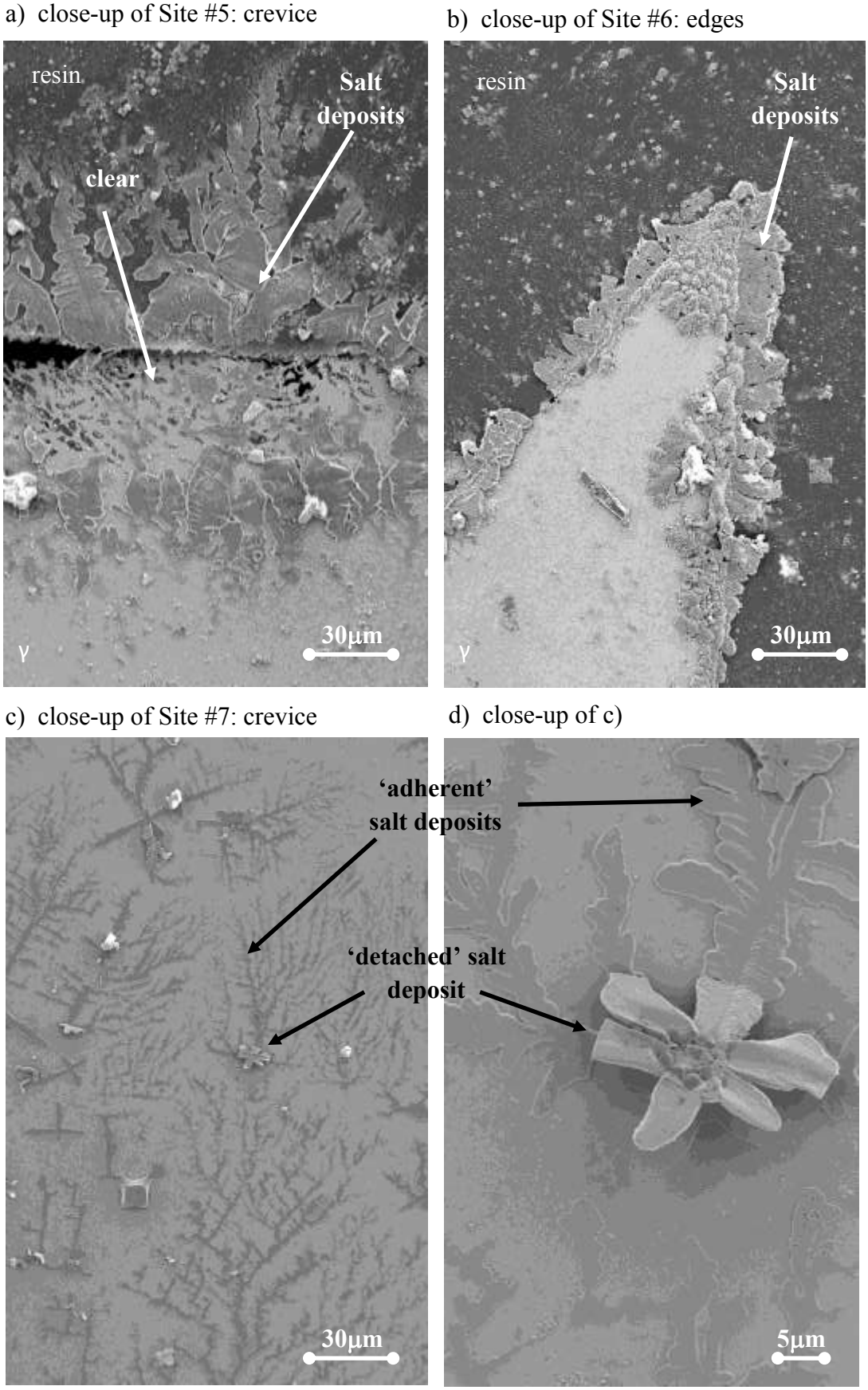

Figure 46 – Salt deposit morphologies of the unrinsed, post-polarised 500°C 96h heat treated electrode

4.3 Chemical Analysis of Subsurface Corrosion

Cross-sections of the post-polarised electrodes were obtained using the FIB technique for subsurface chemical composition characterisation in a TEM. The characterisation presented in this section includes imaging and acquisition of characteristic X-rays from the FIB cross-section using an electron probe of 0.5 nm diameter in either a fixed-spot or scanning mode. Figures 47 to 49 show representative examples of the FIB cross-sections and analyses of the as-received samples (previously measured an average $E_{5.0}$ value of 1.15V). They are compared to the 500°C, 600°C and 800°C 192h heated samples which registered average $E_{5.0}$ values of 0.34V, 0.65V and 0.45V (v.s. Ag|AgCl, Section 4.1) shown in Figures 50-52, 53-57 and 58-59 respectively. In several instances the FIB cross-sections shown were obtained from sites in which corrosion is 'developing' in order to investigate the conditions or internal structure of the anodic dissolution processes occurring.

Figures 47 show FIB cross-sections of two as-received AGR fuel cladding specimens. Low magnification micrographs (Figure 47a and 47b) show an electron-transparent section (~10 µm wide by 4 µm deep) within which the fine precipitates (0.1 – 0.5 µm diameter), indicated by the dark-contrast spots, are dispersed homogeneously throughout the austenitic grains. Three sites highlighted as Site #8, #9 and #10 are shown magnified in Figures 47c, d, e and f with labels indicating the location of probes used for chemical analyses at specific features. The dispersion of fine precipitates was labelled from M to T with their chemical analyses given in Figure 48. The fine precipitates were determined as niobium-rich phases with a mean composition of about 66.6±16.8 at% Nb; they range from 0.1 to 0.5 µm in diameter. The chemical composition of the nominal AGR fuel cladding's austenite grains indicated as A to L in Figure 48 (not explicitly labelled in the micrographs) is 50.3±1.7, 21.0±1.1 and 22.0±0.4 at% of iron, chromium and nickel respectively.

Site #8 contains the occurrence of three adjacent precipitates (labelled X, Y and Z). Analyses indicate that they are a sequence of niobium-manganese-niobium rich phases. Precipitates X and Y have on average a high niobium concentration of 88.4±0.7 at% whereas the manganese-rich precipitate contains about 50.3 at% manganese and 37.1 at% sulphur. Figure 49 confirms their chemical composition via a scanning-probe analysis. The dashed-line indicates the location of the scanning-probe. The chemical profile across the 1.2 µm scan-length, shown as % count,

a) FIB section of as-received AGR fuel cladding #1

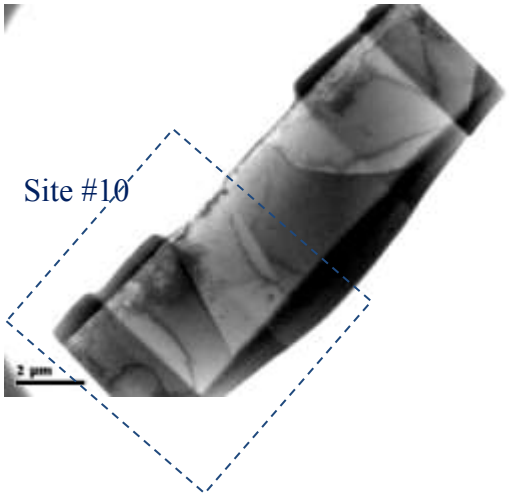

b) FIB section of as-received AGR fuel cladding #2

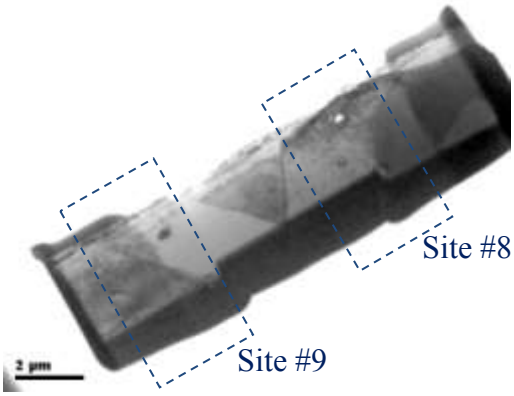

c) Site #10

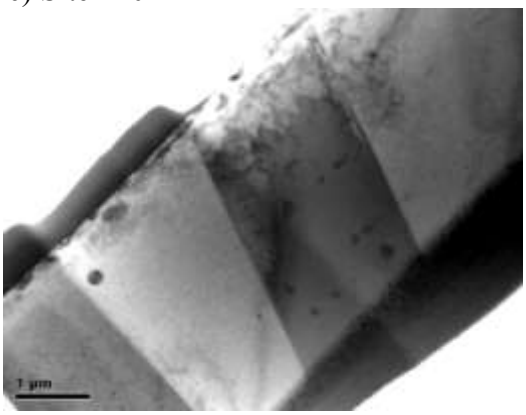

d) Site #8

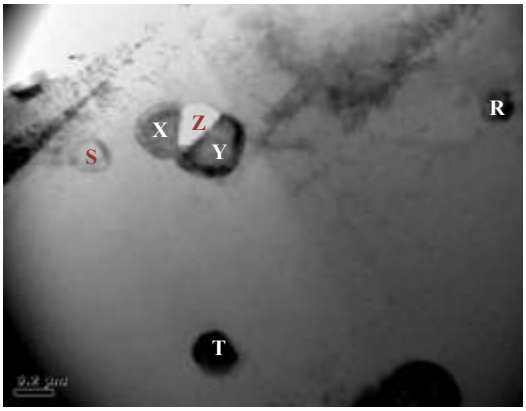

e) Site #10 (extension)

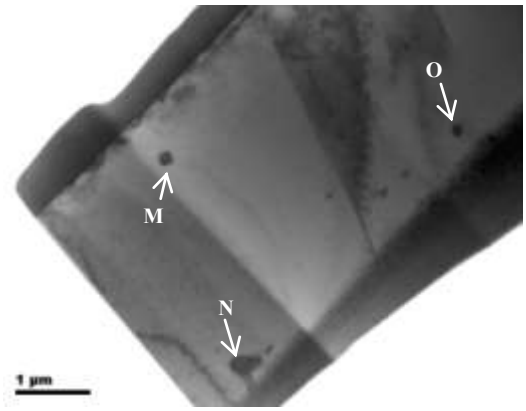

f) Site #9

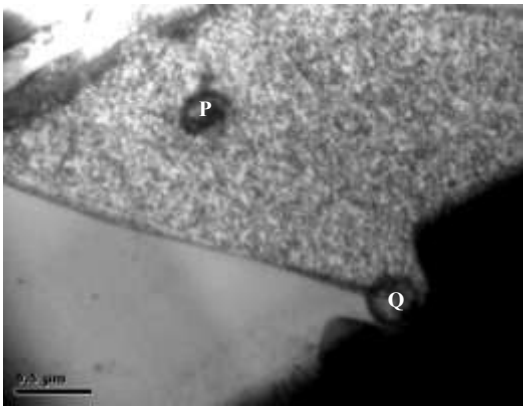

Figure 47 – FIB cross-sections of as-received AGR fuel cladding

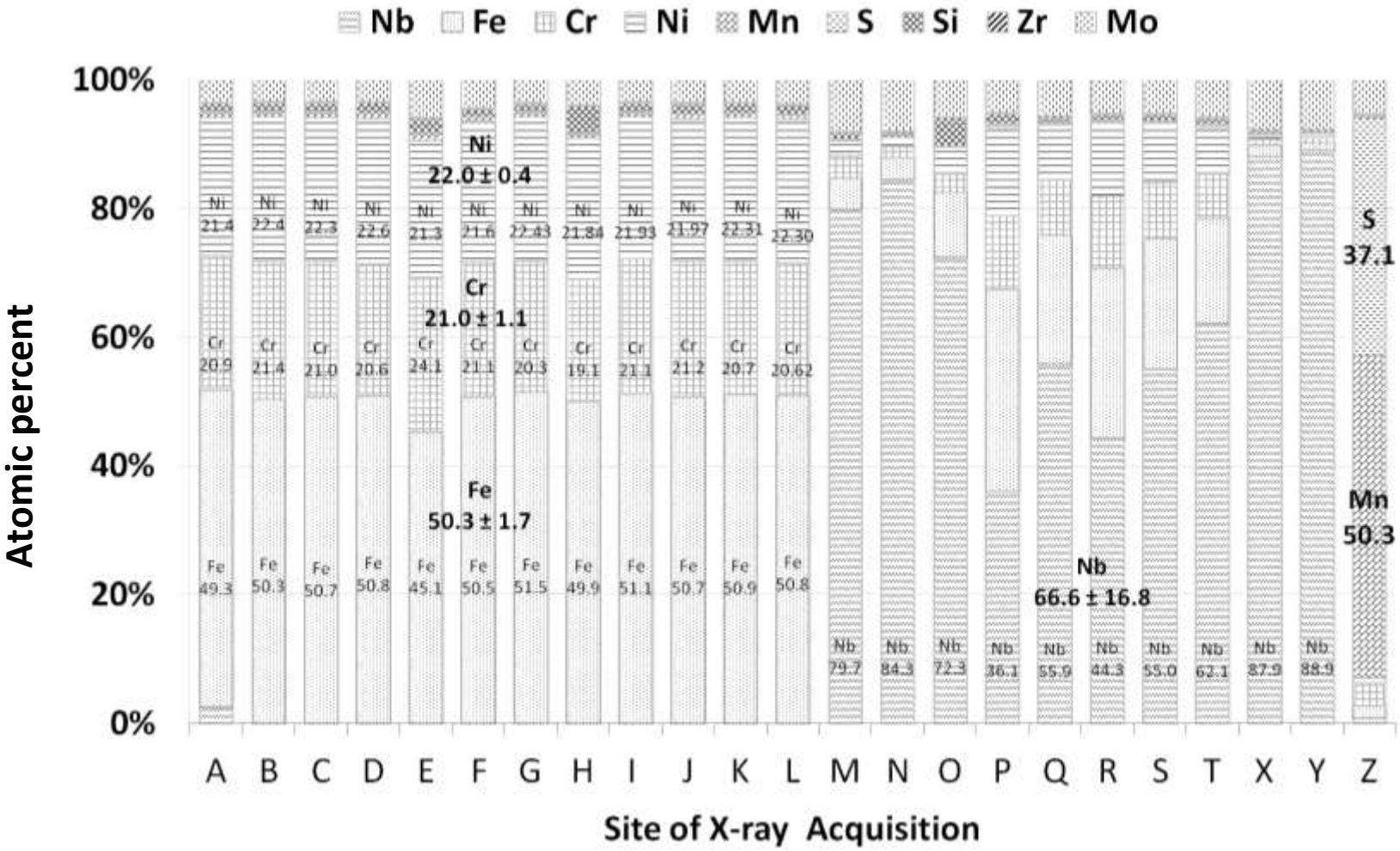

Figure 48 – X-ray analyses of the FIB cross-section from the as-received AGR fuel cladding

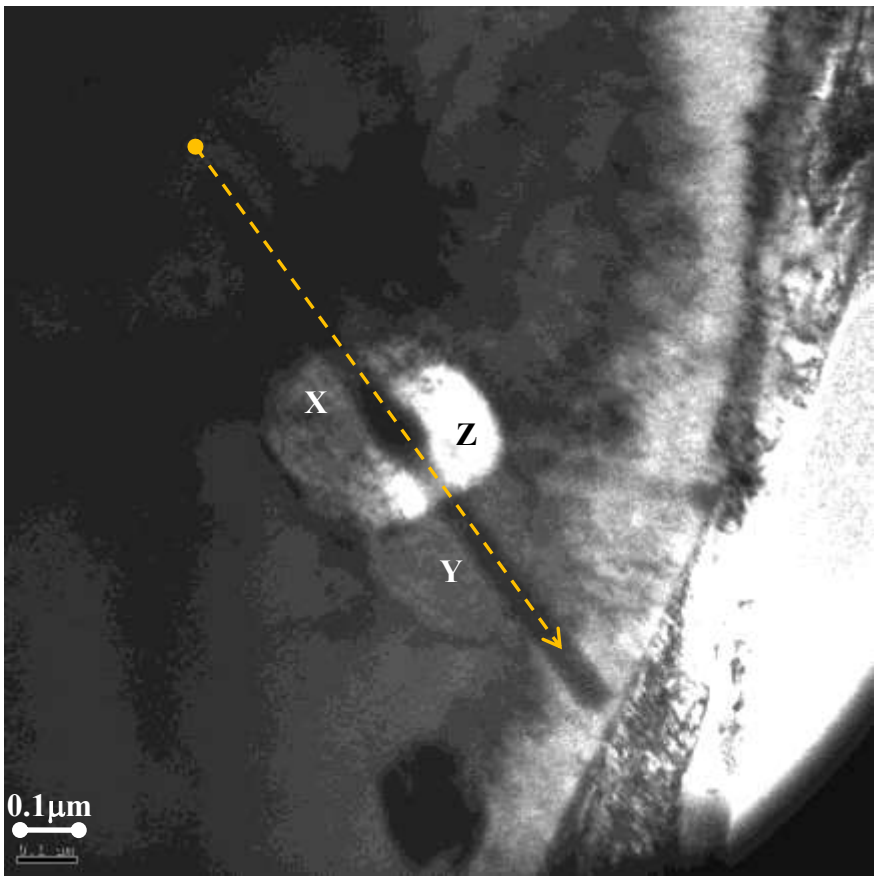

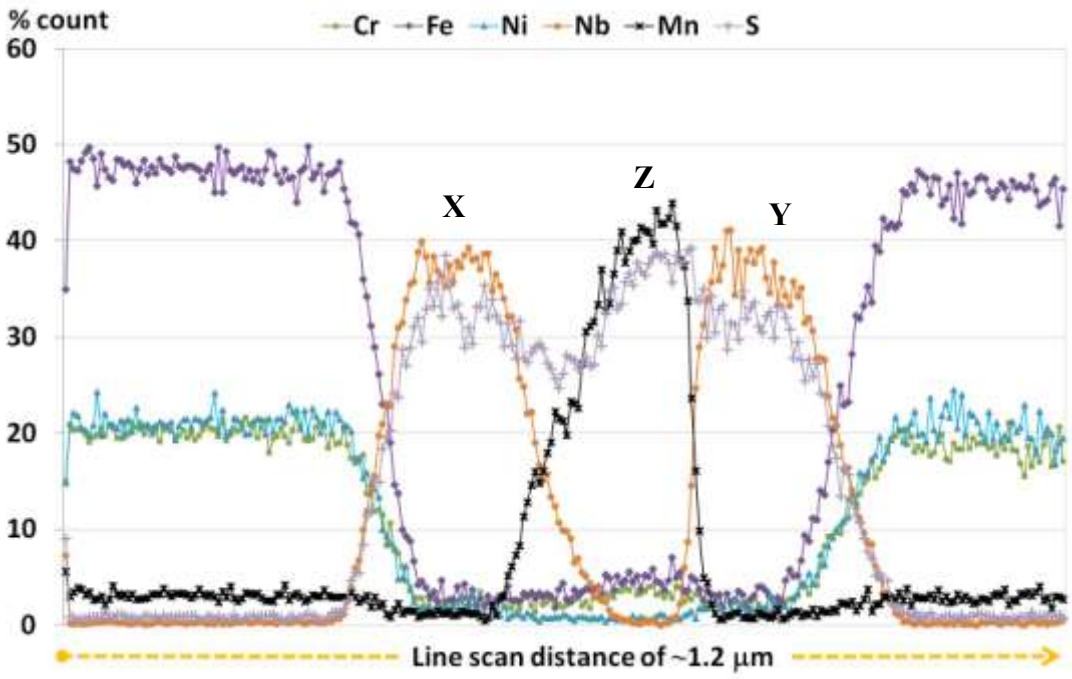

Figure 49 – Scanning-probe analysis of the niobium-manganese-niobium rich precipitates from site #8 of the as-received AGR fuel cladding specimen

conveniently illustrates a sequence of five alternating features: austenite-γ metal; niobium rich precipitate (X); manganese-sulphide precipitate (Z); niobium-rich precipitate (Y); and austenite-γ metal. These features may potentially become conditions for corrosion initiation due to potential for galvanic or electrochemical imbalance. One of the benefits of chemical analyses with FIB cross-sections in a TEM are that features with complex internal structure can be analysed by the fine electron probe, contrary to chemical analyses of the sample surface in an SEM which may produce characteristic X-rays from a large activation volume several angstroms beneath the surface that are not representative of the particular feature.

Figures 50-52 show FIB cross-sections and analyses of the 500°C 192h post-polarised working electrode. Figure 50a shows the electrode surface which consists of a relatively large (~20 μm dia.) lacy corrosion cover located in the bottom left of the micrograph. The rectangular box adjacent to the cover highlights the approximate area where a FIB cross-section was obtained for subsurface corrosion morphology characterisation. Figure 50b (the corresponding FIB cross-section) reveals *microstructures containing strain fields indicative of high dislocation density* and also, interestingly, two 'voids' indicated by the bright spots. The two 'voids' are situated around the particle labelled M (Figure 50d), determined to be niobium-rich phases with an average concentration of 77.2±0.8 at% Nb from the chemical analyses presented in Figure 52. This observation shows that one of the potential avenues for metal dissolution is around NbC precipitates. The NbC precipitates in this sample are large, up to 6 μm wide, relative to those observed in the as-received samples (0.1–0.5 μm dia.) and so are likely due to the heat treatment employed. Figure 50c shows the chemical profile, in % count, across the 3.0 μm scan-length indicated by the dashed-line in Figure 50d which revealed a sequence of alternating phases along regions labelled B, M, C and L: austenite-γ metal; niobium-rich precipitate (M); *dissolved-metal* below the north bright 'void'; niobium-rich precipitate (L); and austenite-γ metal. The term *dissolved-metal* was coined to refer to an alloy composition that is significantly lower than the nominal austenite-γ concentration, previously determined to be 50.3±1.7 at% Fe, 21.0±1.1 at% Cr and 22.0±0.4 at% Ni (Figure 48), which has been frequently observed along the gaps between NbC precipitates. This feature is presented more clearly with another 500°C 192h FIB cross-section shown in Figure 51. Figure 51a was labelled X, Y and Z for

the fixed-spot chemical analyses and a dashed-line parallel to them for scanning-mode chemical analyses. The results of the fixed spot chemical analyses shown in Figure 52 (the right hand bar charts) indicate that Y is a dissolved-metal region which contains niobium (18.7 at% Nb) with dissolved alloy compositions of 40.1 at% Fe, 16.7 at% Cr and 18.2 at% Ni – a 20.2%, 20.5% and 17.3% decreased in Fe, Cr and Ni from the nominal austenite-γ metal. Y is sandwiched between X and Z, both of which are relatively large (compared to the 0.1 μm-sized niobium phases in as-received samples) niobium-rich phases that averaged 90.0±0.3 at% niobium and were ~1 μm wide for precipitate Z and up to 6 μm wide for precipitate X. Results from the scanning-mode chemical analyses (Figure 51b) shows the chemical profile, in % count, across the 1.2 μm scan-length which confirms a dissolved-metal region in between two large niobium carbide precipitates. Regions G, H, I, J and K represents the austenite-γ metal of the heat treated samples with 50.3±0.6 at% Fe, 20.9±0.6 at% Cr and 22.1±0.2 at% Ni that are closely comparable to those measured in the as-manufactured samples (Figure 48).

Comparing the FIB sections of as-received AGR fuel cladding (2 samples shown in Figure 47) and those heated 500°C 192h (2 samples shown in Figure 50 and 51), we can say that heat treatment causes the NbC precipitates to grow considerably in size; across the FIB sections which have consistent dimension, the former contains NbC precipitates of ~0.5 μm dia. whereas the latter ~5um dia. (an order magnitude growth), even becoming comparable to the austenite-γ grains adjacent to them. In section 4.2, we proposed that, because the NbC precipitates remains well maintained even though extensive corrosion has occurred around them, NbC *acts as a cathode* in the participating galvanic corrosion processes; the current observations (and further substantiated later in the section) we propose that the NbC precipitate size is an issue which may enhance this corrosion effect. In addition, Figures 50b and 51a shows FIB sections with *high dislocation densities* (thus high stress fields), potentially as a result of the particle size growth, which may be another contributing factor to the corrosion processes. FIB cross-sections shows *subsurface corrosion propagation occurs along the periphery of the NbC precipitates*, either as a fully oxidised metal manifesting as voids (Figure 50d) or alloy of decreased concentration from its nominal austenite-γ metal (coined *dissolved-metal regions*), on the order of 20.2%, 20.5% and 17.3% depletion in Fe, Cr and Ni respectively.

a) post-polarised electrode surface with lacy cover

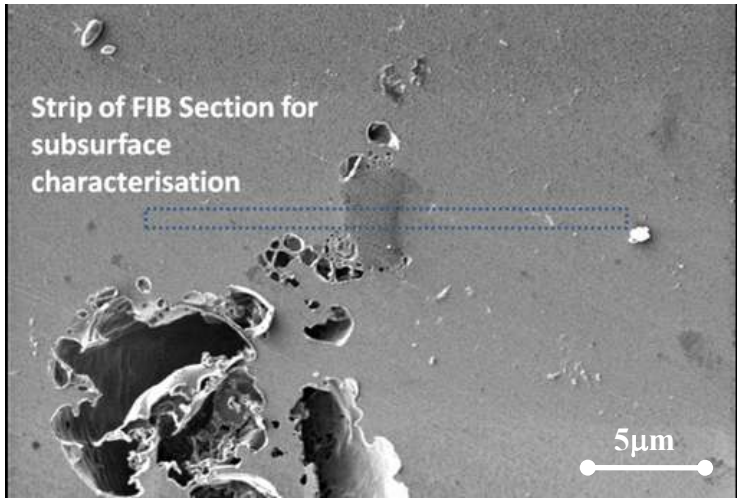

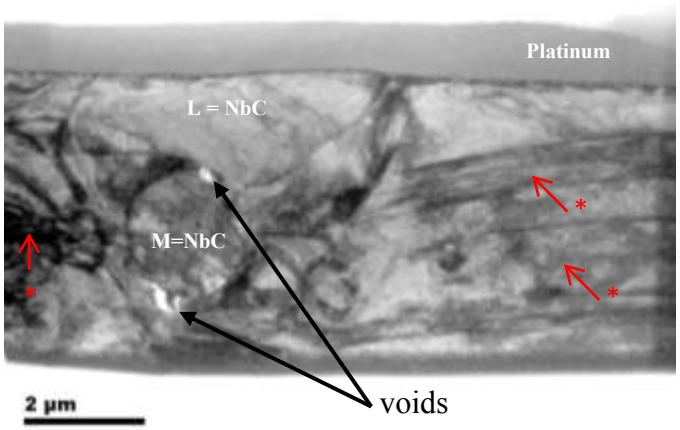

b) FIB cross-section indicating high **dislocation densities***

c) scanning probe analyses

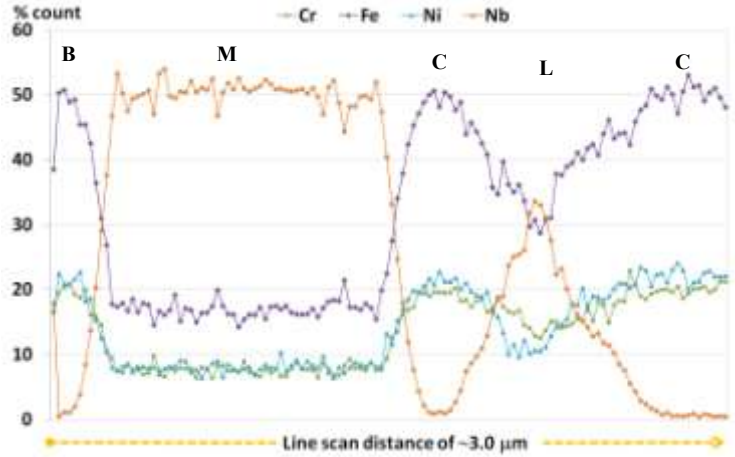

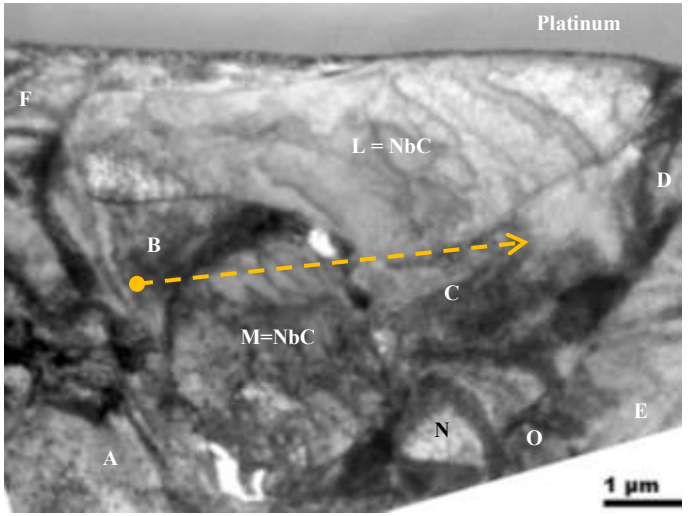

d) location of scanning probe indicated by the dashed-line

Figure 50 – FIB cross-section analyses with a scanning probe of the 500°C 192h post-polarised working electrode

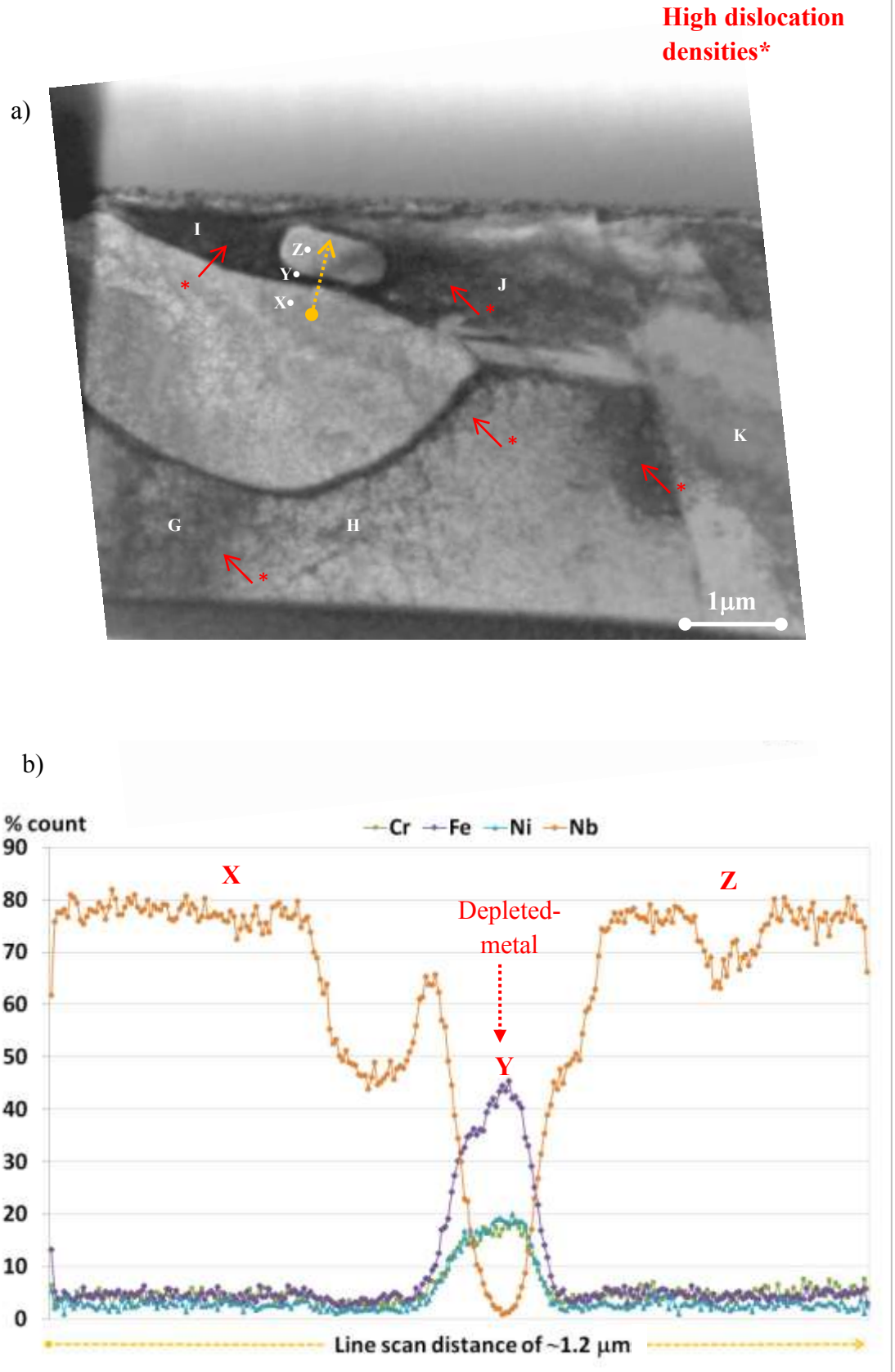

Figure 51 – FIB cross-section of high dislocation densities and scanning probe analyses of the 500°C 192h heated post-polarised working electrode

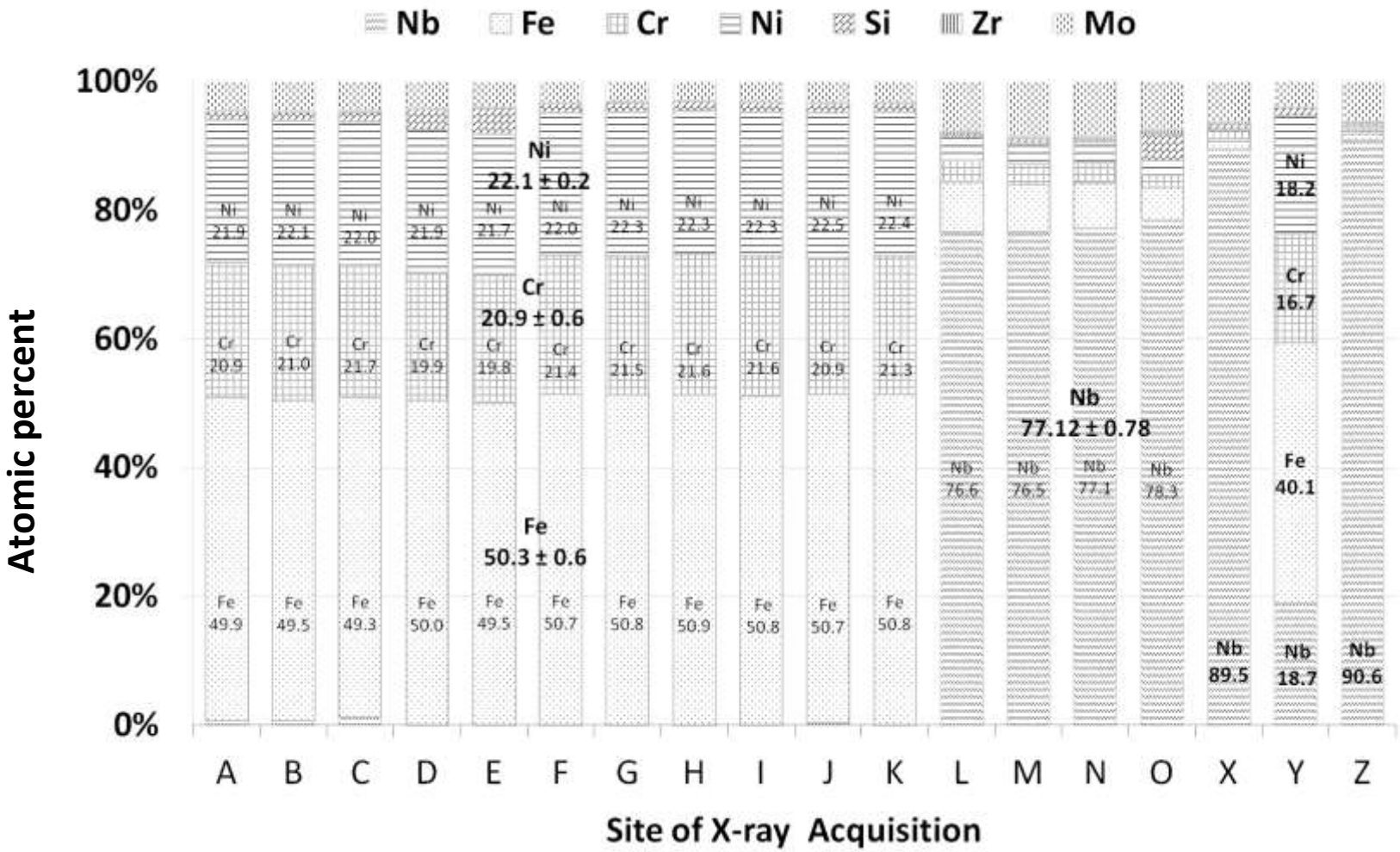

Figure 52 – X-ray analyses of the FIB cross-section from the 500°C 192h AGR fuel cladding

Figures 53 to 57 show two FIB cross-sections and their analyses from the 600°C 192h post-polarised electrodes. Figure 53a shows a corroding site adjacent to an inclusion whose FIB cross-section was obtained (Figure 53b). Figure 54 shows the chemical composition results from areas labelled from the same region A to E. Metal dissolution is shown to occur around a 2 µm wide aluminium-rich precipitate (A) of about 86.1 at% Al. The austenite grains (labelled B to E), however, were composed of 47.4±1.4 at% Fe, 19.9±0.5 at% Ni and 21.9±0.3 at% Cr respectively. Compared to as-received samples, which contained 50.3±1.7 at% Fe, 21.0±1.1 at% Cr and 22.0±0.4 %at Ni, this particular heat treatment causes a small but significant change from the cladding's nominal austenite-γ composition, i.e., a 5.6% and 5.2%

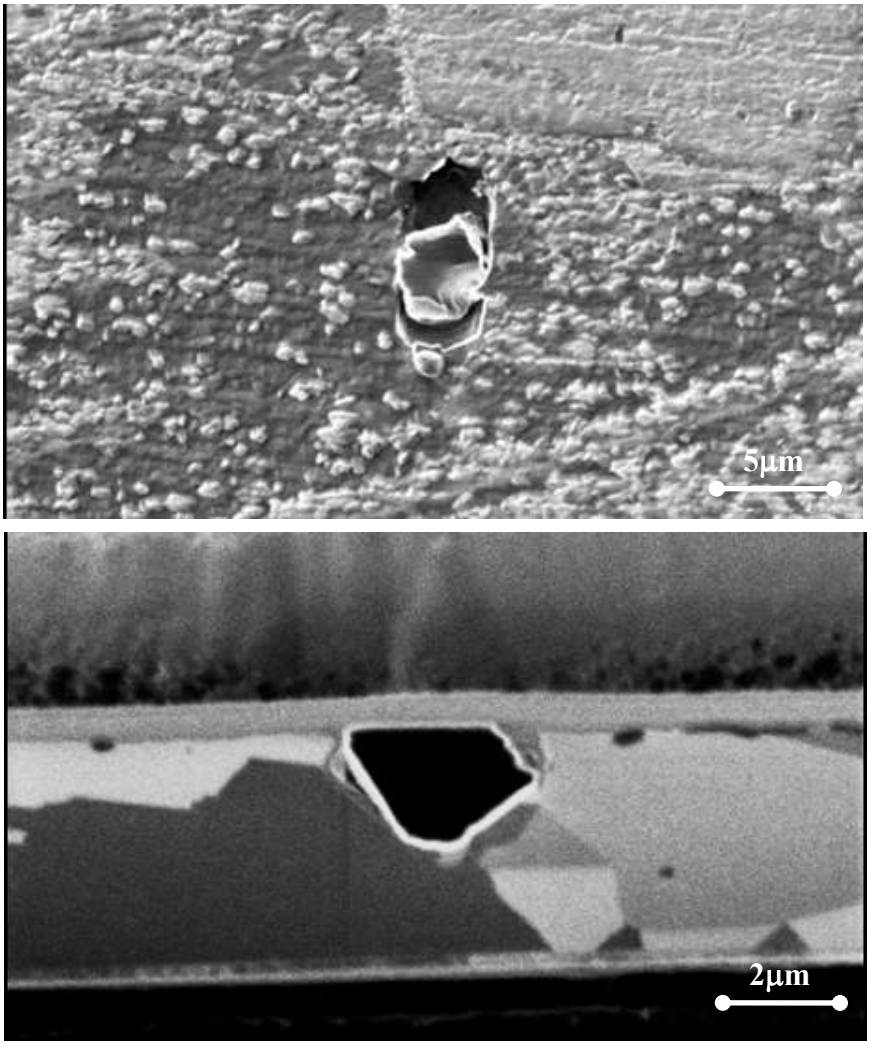

a) metal dissolution around inclusion

b) FIB cross-section

Figure 53 – FIB cross-section of the 600°C 192h heated post-polarised working electrode. Note that the rough surface in Figure 53a is just an artefact due to over-rastering with ion beams whilst focussing the sample for FIB section preparation.

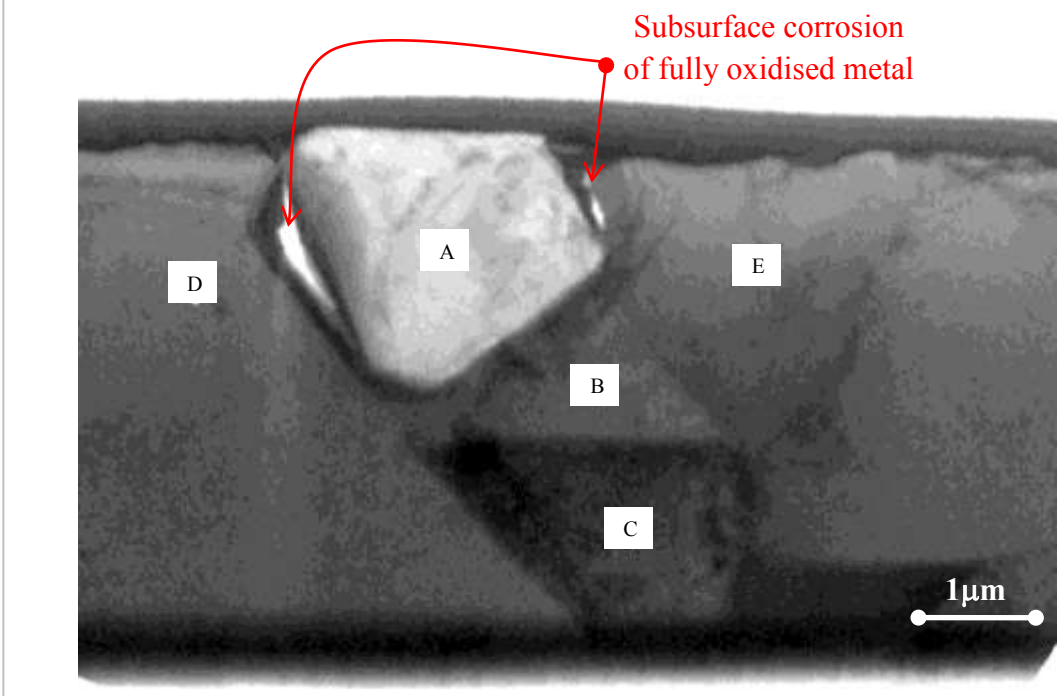

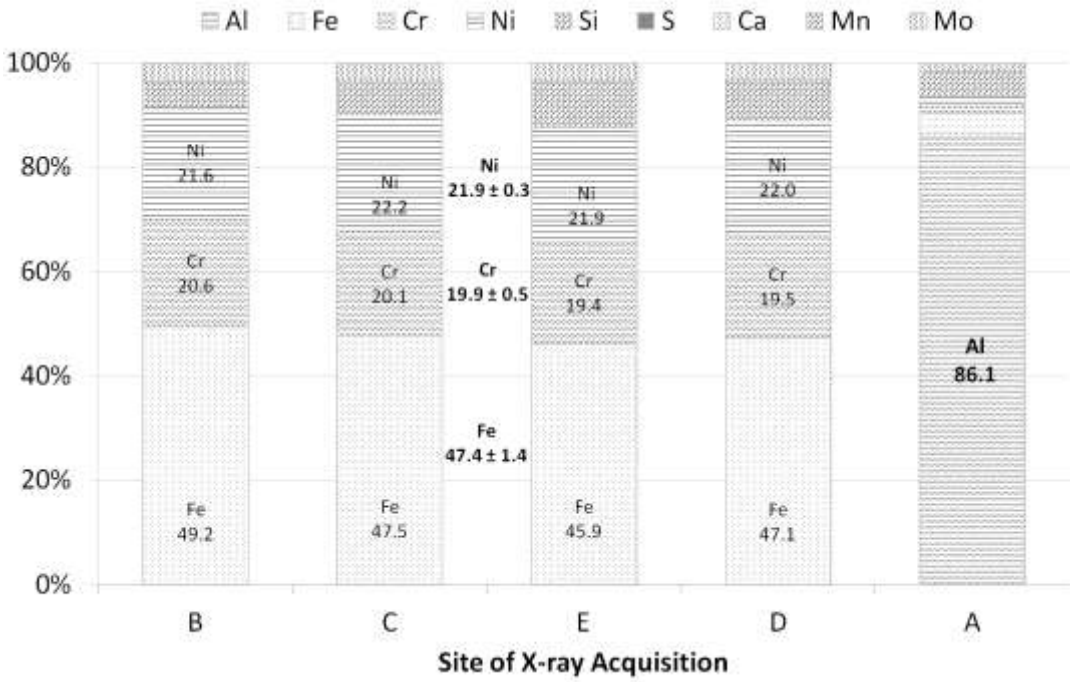

Figure 54 – X-ray analyses of FIB cross-section from 600°C 192h AGR fuel cladding

decrease in austenite Fe and Cr respectively. This decrease in alloy Fe and Cr may indicate increased activity of the niobium in the microstructure, i.e., more alloy were precipitated by the niobium atoms as secondary phases that are large in size.

The FIB cross-section shown in Figure 55 indicates a 'bright' region of about 10% the area of the section in which the metal is apparently 'disintegrating'. Figure 58a labels alphabetically the detailed chemical composition measurement within this region in order to characterise the internal structure of the 'disintegrating' metal. The varied contrast parts of this region are indicative of the presence of different phases; the brightest contrast is at void arising from anodic dissolution of the metal. Chemical analyses (Figure 56b) reveal four different phases:

I. sites E, I, J, L and A are aluminium-rich silicon phases **(AlSi)** with average concentrations 74.0±4.1 at% Al and 12.9±1.8 at% Si;
II. sites F, K, and B are zirconium-rich aluminium phases **(ZrAl)** with average concentrations 56.8±10.3 at% Zr and 26.3±9.8 at% Al;
III. sites H and G are manganese-sulphide phase **(MnS)** of concentrations 42.1±0.5 at% Mn and 35.6±0.3 at% S; and

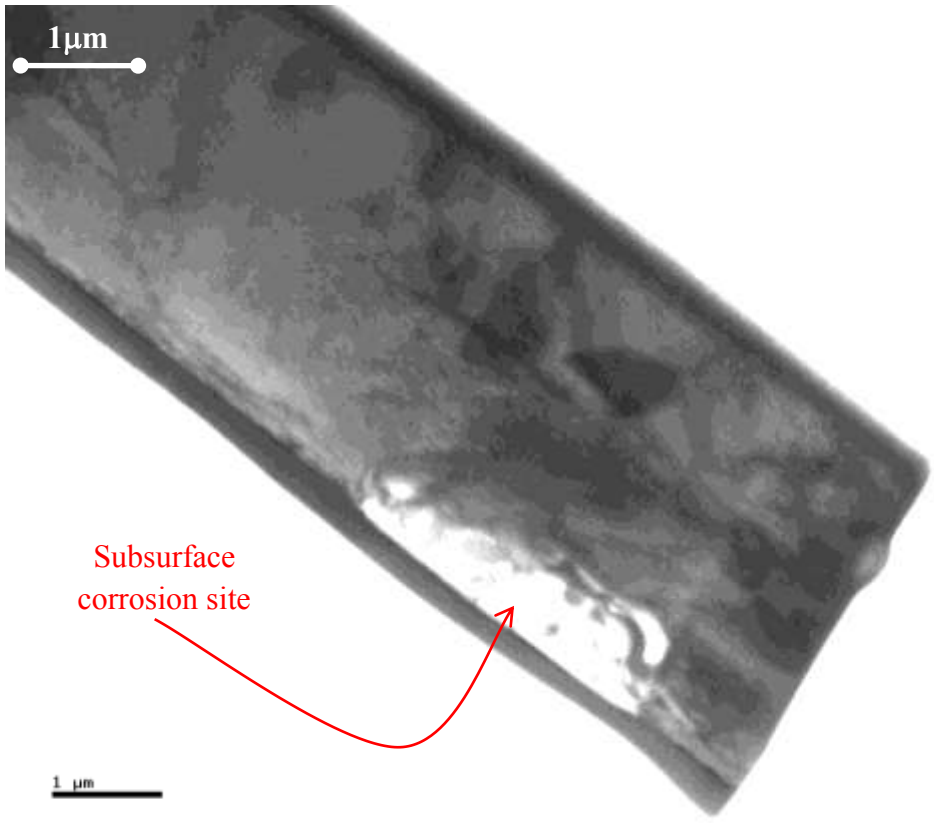

Figure 55 – FIB cross-section of the 600°C 192h heated post-polarised working electrode

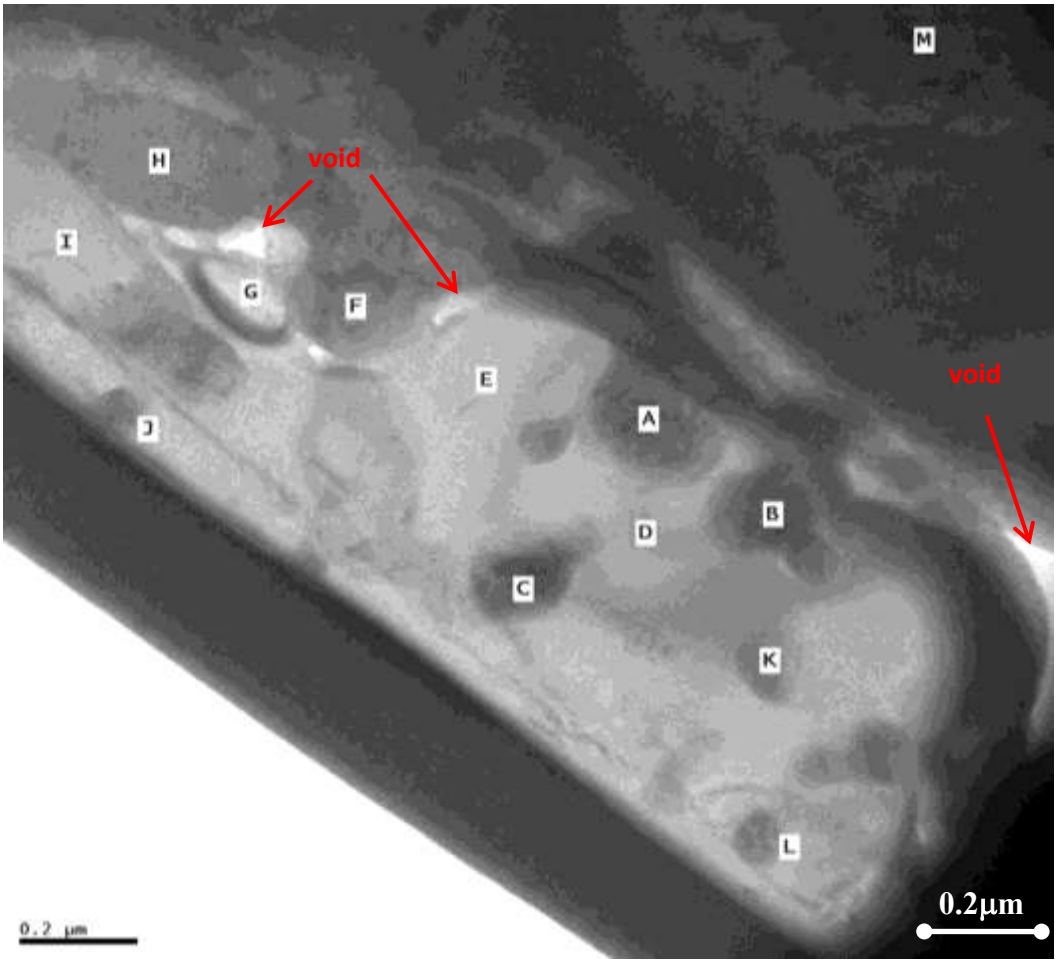

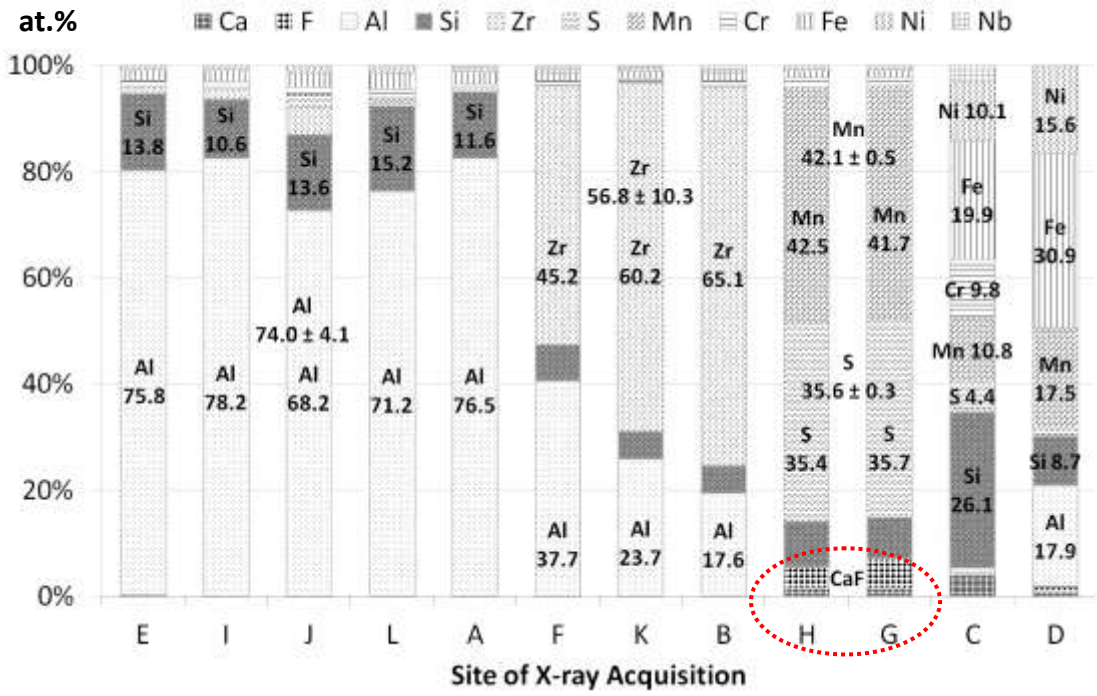

Figure 56 – X-ray analyses of the FIB cross-section from the 600°C 192h AGR fuel cladding

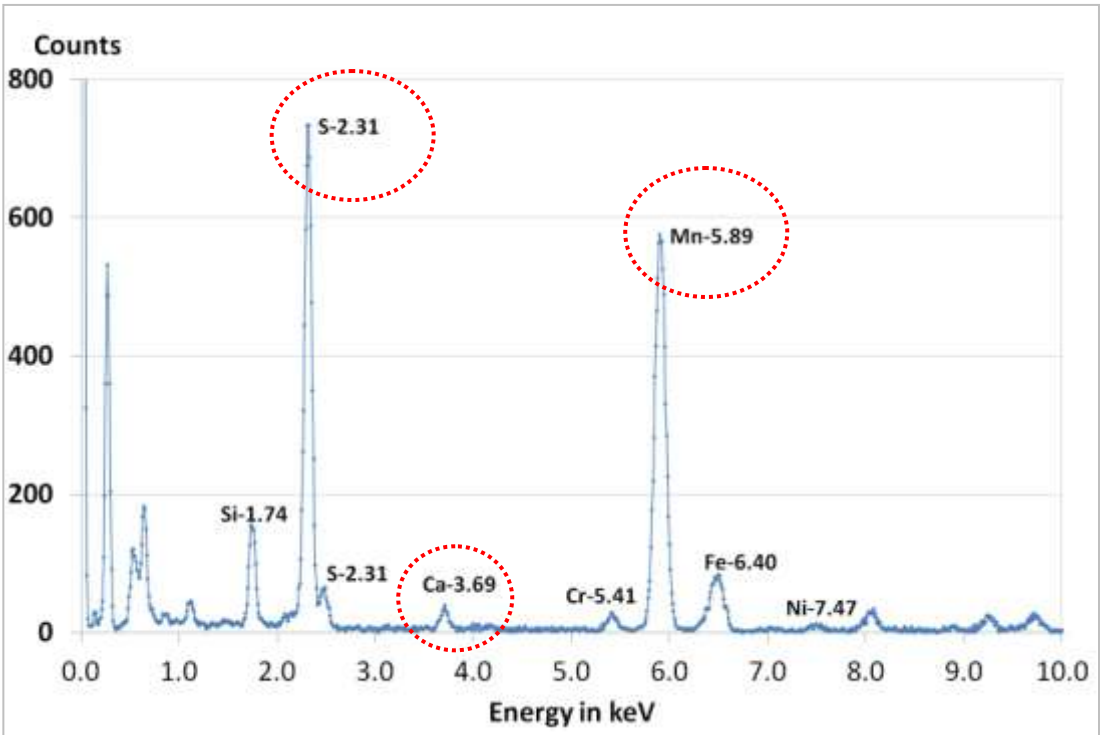

Figure 57 – X-ray spectra indicating counts of elements from the 600°C 192h AGR fuel cladding

IV. sites C and D which are dissolved-metal phase**,** as previously discussed, of 25.4±7.8 at% Fe (49.5% decrease from nominal austenite-γ) and 12.8±3.9 at% Ni (42.1% decrease from nominal austenite-γ). Note that Site C is silicon-rich with 26.1 at% Si and Site D is aluminium-rich with 17.9 at% Al but *zero chromium,* rendering the metal non-stainless.

Sites H and G (the MnS-phase) beside the voids revealed elevated levels of calcium and fluorine, even though the co-located site F (the ZrAl-phase) was *not* calcium- or fluorine-containing. The occurrence of calcium is confirmed by EDS (Figure 57) which shows distinct peaks for calcium (as well as Mn and S) indicative of its presence, supporting the role of MnS in localised corrosion processes as demonstrated by Ryan *et al.* [13].

Other sites of corrosion interest include the periphery of sites A, B, C, D and K which have different chemical compositions, including the zero- chromium, non-stainless zone (site D). These observations may indicate the different corrosion rates of the alloy or micro-segregation.

Figure 58 shows the pitted surface, FIB cross-section and a TEM image with labels of the 800°C 192h electrode. Figure 58a shows the electrode's surface which contains a small pit ~2μm wide. A FIB cross-section was obtained from around this region to characterise the subsurface corrosion morphology. Figure 58b shows a successfully-prepared FIB cross-section which indicates a large ~2μm wide subsurface corrosion cavity beneath the metal. Figure 58c is the corresponding bright-field TEM image. Labelled alphabetically A to F are the locations of electron probes used for chemical composition analysis, results shown in Figure 59a. A and B were both niobium-rich particles having average concentrations of 83.7±1.1% Nb. All other regions analysed were austenite grains of composition iron, chromium and nickel of concentration 47.7±1.1, 19.7±0.4 and 20.9±0.3 at% respectively. In addition a line-scan of ~3.5 μm long was performed parallel to E, A, B and C indicated by the dotted-line, results shown in Figure 59b. The scan profile shows in sequence: nominal austenite-γ; weakened metal; niobium-rich precipitate (A); weakened metal; niobium-rich precipitate (B); weakened metal; and nominal austenite-γ. This observation reaffirms the detrimental effect of the niobium-rich particle which appears to be one of the drivers for corrosion initiation.

As a summary, this section has compared the subsurface corrosion morphologies of the post-polarised electrodes which include the as-received cladding specimens, the 600°C 192h, 800°C 192h, and 500°C 192h heat-treated specimens that register $E_{5.0}$ electrode potential values of 1.15V, 0.65V, 0.45V and 0.34V respectively (Section 4.1). The two most important microstructural features that affect corrosion behaviour are NbC size and presence of dislocations in the austenitic-γ matrix. Compared to the heat-treated samples, the as-received specimens have small NbC precipitates ~0.1μm and there were numerous counts of these precipitates, ~20 within a 10 by 4 μm analysable area within a FIB-section, that are homogeneously distributed (Figure 47). Upon heat treatment, it was observed NbC precipitates between ~1.5 and 5μm in size, significantly larger than those observed in the as-received specimens. In addition, there were increased dislocation densities in the surrounding austenite-γ matrix (Figures 50 and 51). Whilst the *surface* corrosion morphologies characterisation discussed in Section 4.2 suggest that the NbC precipitate may act as cathode in the participating galvanic corrosion processes, the *subsurface* corrosion morphologies characterisation with FIB-sections herein

suggest that corrosion is *initiated* around the periphery of these phases indicated by the metal depleted regions which have alloying elements concentration substantially decreased from its nominal austenite-γ composition (50.3±1.7 at% Fe, 21.0±1.1 at% Cr, 21.0±0.4 wt% Ni), at varying degrees up to zero-percent chromium which renders the steel non-stainless. This effect is also shown in between individual NbC precipitates and austenite-γ matrix and between two collocated NbC precipitates (Figures 50b, 51a and 58c). In most cases (7 out of 8 FIB sections prepared), the observed metal dissolution occurs around NbC precipitates because they are the primary strengthening particles for the AGR fuel cladding (reviewed in section 2.2). However, it has also been observed that metal dissolution may also occur around the non-primary secondary phases including MnS, AlSi, ZrAl as shown in Figures 54 and 56, not a critical corrosion issue because of their low distribution in the AGR fuel cladding matrix.

a) post-polarised electrode surface with a 2 µm wide pit

b) FIB-cross section from a)

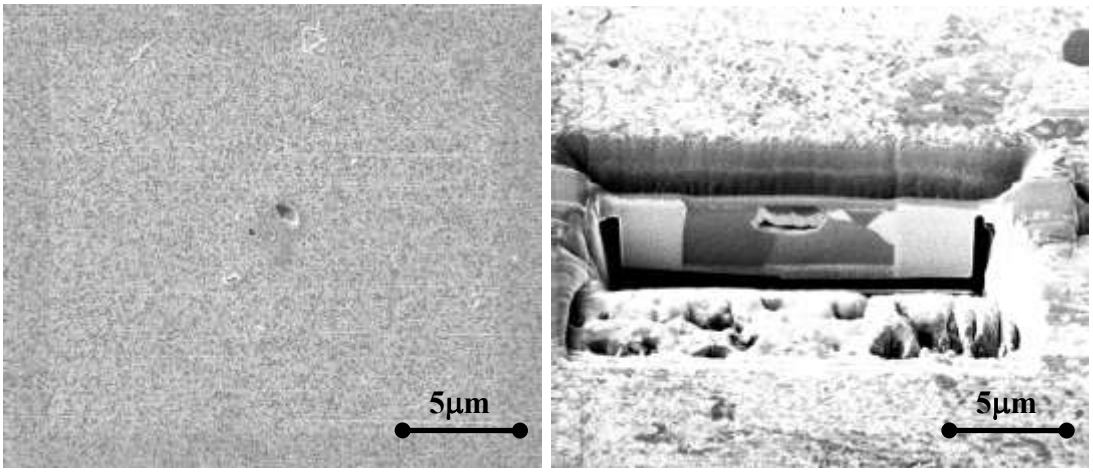

c) Bright-field TEM image

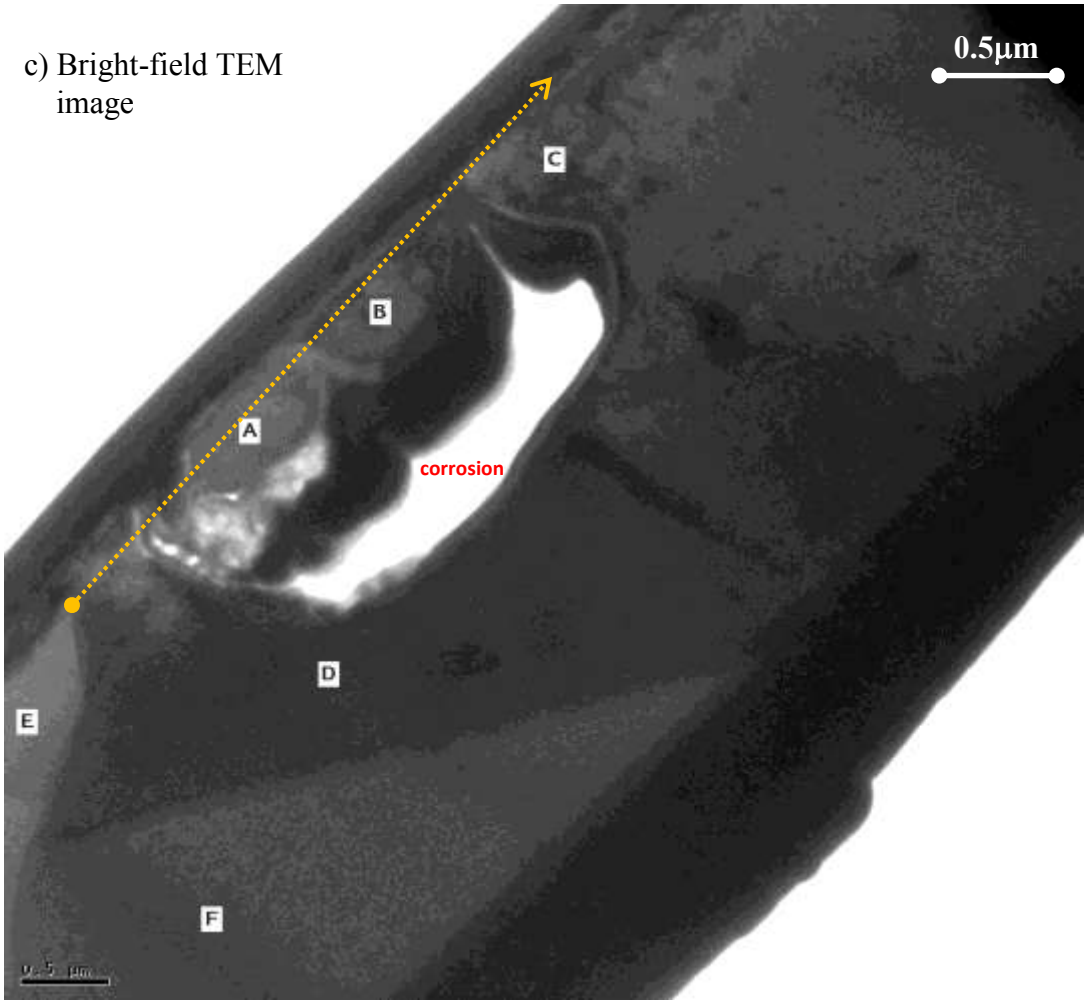

Figure 58 – FIB cross-section of the 800°C 192h heated post-polarised working electrode

a) fixed-spot X-ray analyses

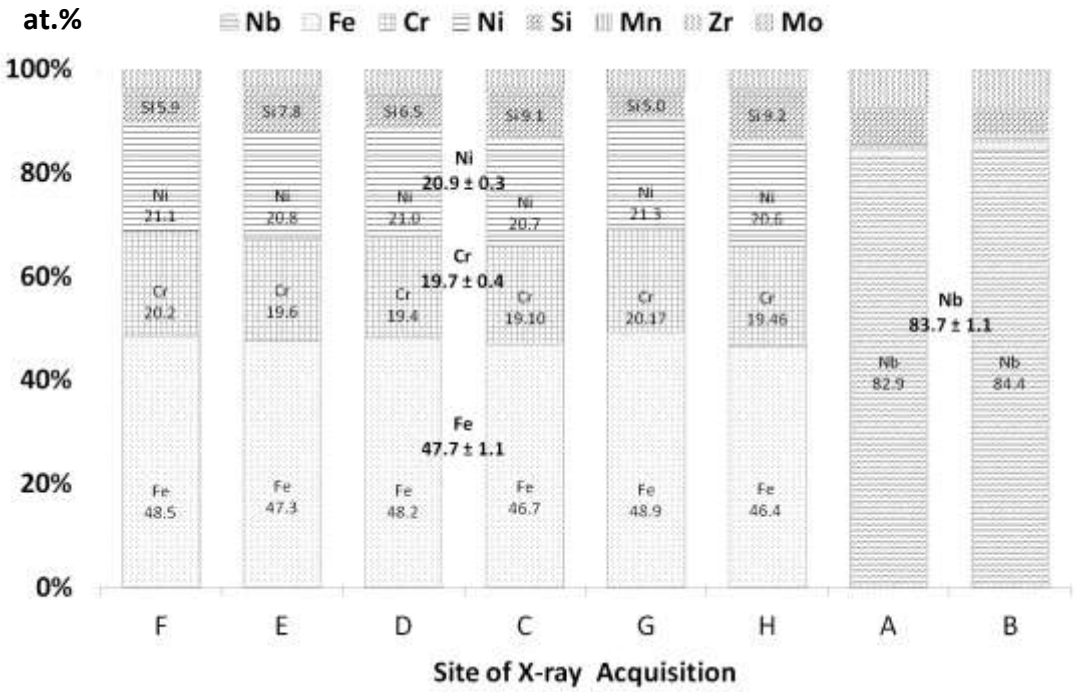

b) scanning-probe analyses

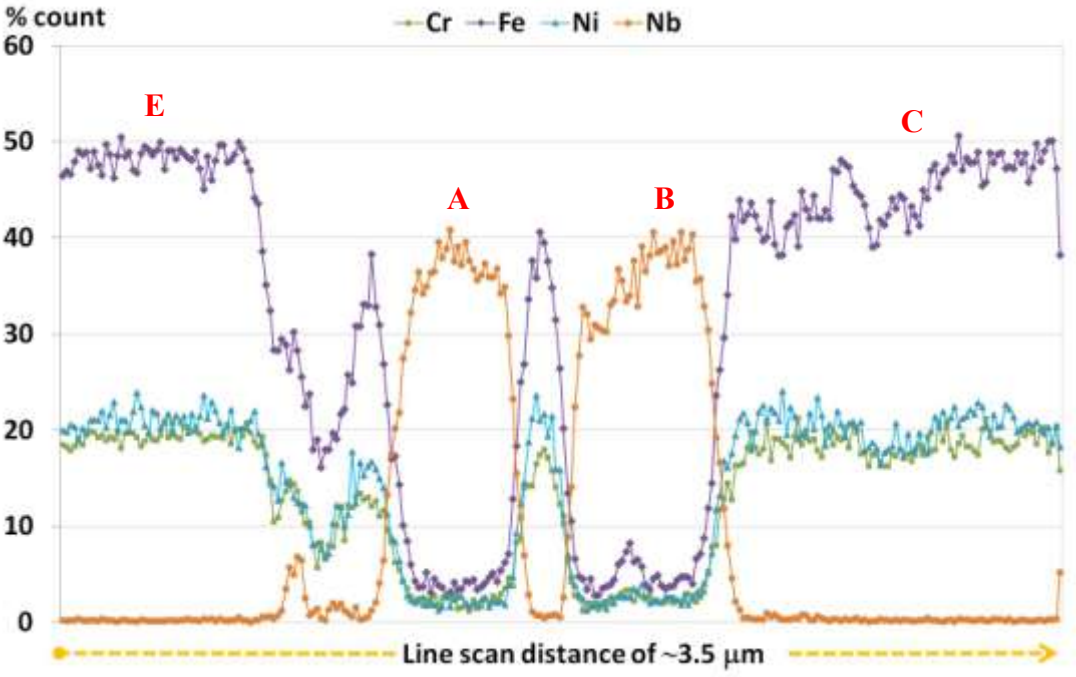

Figure 59 – X-ray analyses of the FIB cross-section from the 800°C 192-hour AGR fuel cladding

4.4 Microstructures of Heat-Treated Samples

Several etchant candidates were compared for their ability to reveal the electrode's microstructure for SEM examination. Figure 60 compares the as-received AGR fuel cladding electrode to those that have been swabbed in Kallings solution for 20s, Marbles solution for 20s and electrolytically-etched with saturated oxalic acid solution for 10s on a 6V potential. The electrolytic-etch (Figure 60d) most

a) Post-polarised electrode

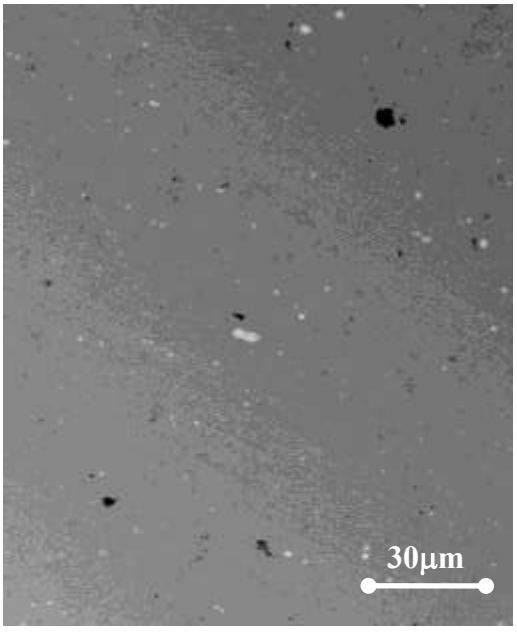

b) Kalling's, swabbed 20s

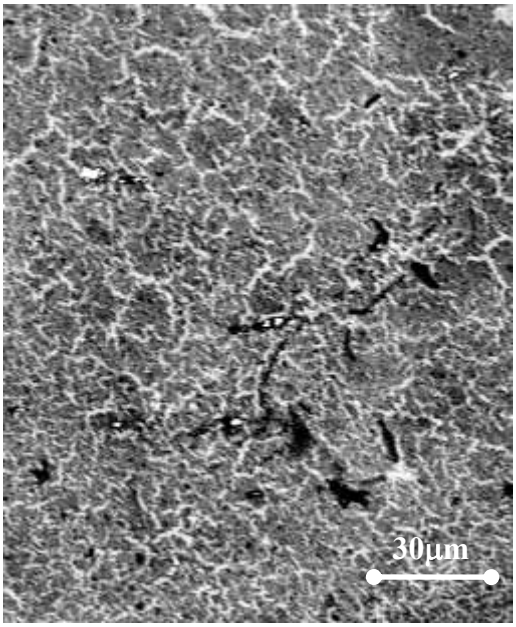

b) Marbles, swabbed 20s

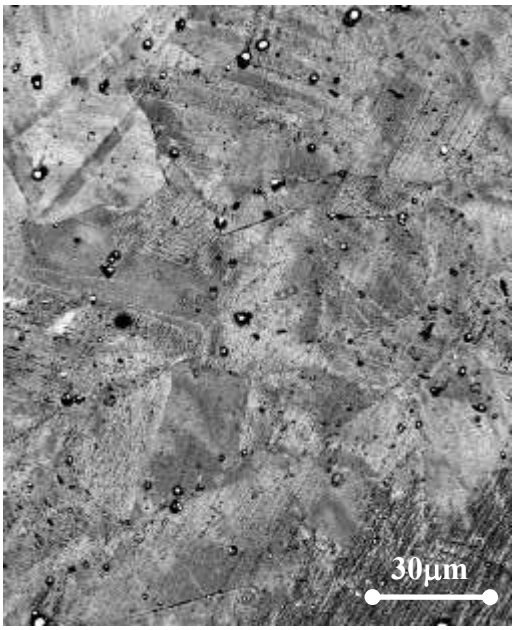

d) Oxalic acid, electrolytic-etching

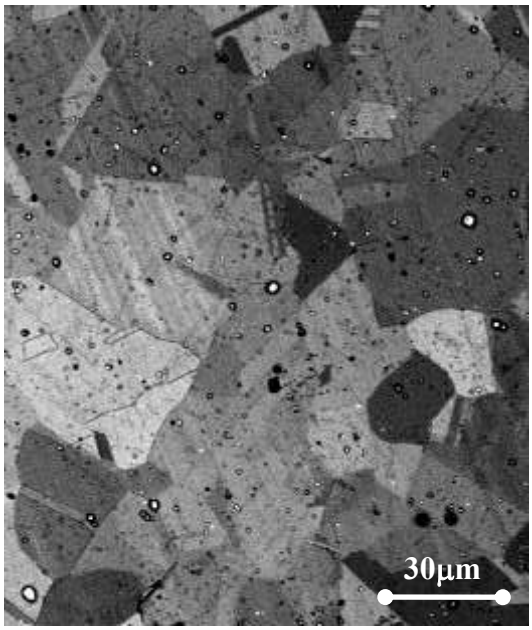

Figure 60 – SEM images of as-received AGR fuel cladding microstructures from several etchants

clearly revealed the microstructural feature including the austenitic grains, twins, grain boundaries and dispersion of secondary phases indicated by the bright atomic contrasts. SEM images obtained from the other swab-based etchants generally produce lower contrast micrographs with increased numbers of etch-pits, even though etching with the Marble's reagent for 20s produced images that are similar to the electrolytically-etched samples. Etching by Kalling's reagent produced an increase in number and size of etch-pits, low image quality and is an ineffective etchant for the AGR cladding material. Given the satisfactory micrographs from electrolytically-etched samples, these techniques were used throughout the thesis and further systematic investigation of the dependence of etchant and etching time for image optimisation was not pursued.

Figures 61 to 64 show low magnification microstructures and counts of bright contrast indicative of secondary phases from the as-received, 600°C 192h, 800°C 192h and 500°C 192h electrolytically-etched electrodes that are associated with $E_{5.0}$ values (section 4.1) of 1.15V, 0.65V, 0.45V and 0.34V respectively. To enable comparison among samples, all the micrographs were recorded under consistent SEM condition of 20kV accelerating voltage and 13 mm working distance. Over an area of 0.05 cm^2, 3115±296 precipitates were observed in the as-received cladding (Figure 61), 1729±146 in the 500°C 192h samples (Figure 62), 2264±44 in the 600°C 192h samples (Figure 63) and 1580±105 in the 800°C 192h samples (Figure 64); the maximum precipitate diameter within the microstructures were ~2, 20, 5 and 20 μm respectively. Figure 65 is a summary of the variation in number of precipitates and maximum precipitate diameter with $E_{5.0}$ (current when potentio-dynamic scan reach 5.0 mA/cm^2).

The microstructure of the as-received samples is characterised by the homogenous dispersion of fine ~0.1 μm precipitates (the largest being ~2μm) and relatively high precipitate counts of ~3115±296 (/0.05cm^2). The observed austenitic grains ~25 μm dia. agree with those reported by Waddington and Jones [20]; they have composition of 50.3±1.7 at% Fe, 21.0±1.1 at% Cr, 21.0±0.4 wt% Ni as established from EDS analyses on the FIB sections (Figure 48). Such are the general microstructural features that correspond to the least corroding samples which has an average $E_{5.0}$ of 1.15V. On the contrary, for the samples that were heat-treated at critical temperatures (500°C and 800°C, Figure 34) and heating times (192h, Figure

a) Electrolytic-etched microstructure of as-received AGR fuel cladding

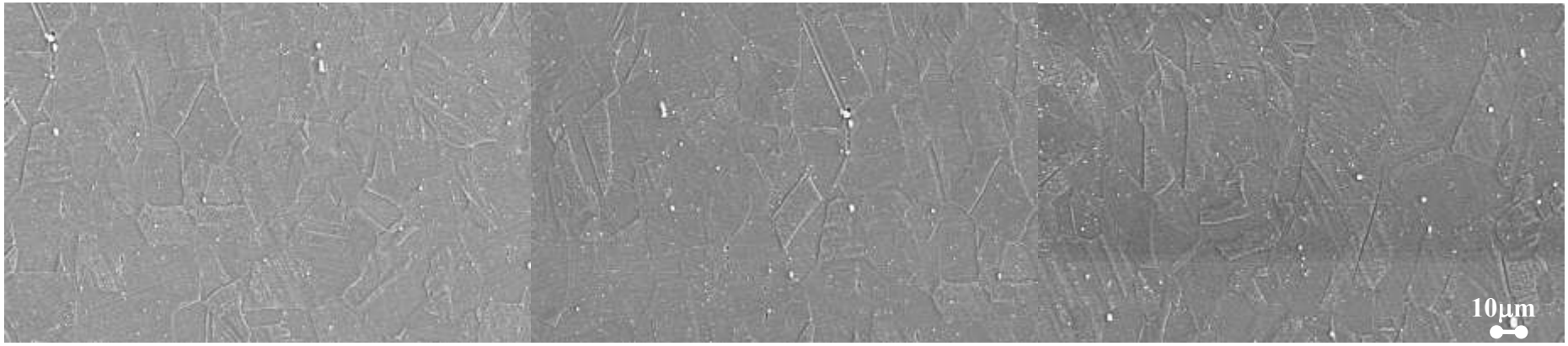

b) Precipitate contrasts (total of individual precipitates = 3115)

Figure 61 – Microstructure and precipitate count of as-received AGR fuel cladding

a) Electrolytic-etched microstructure of 500°C 192h specimens

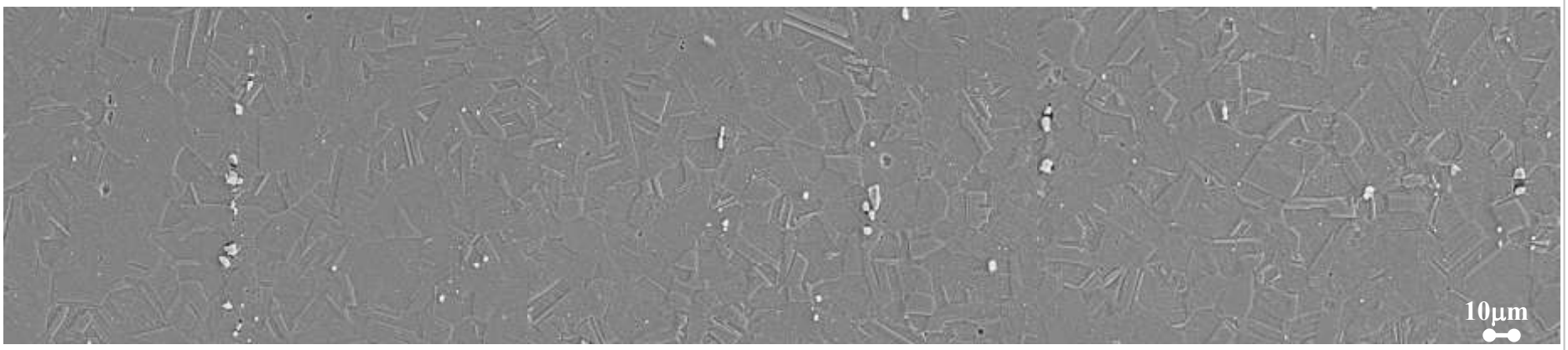

b) Precipitate contrasts (total of individual precipitates = 1789)

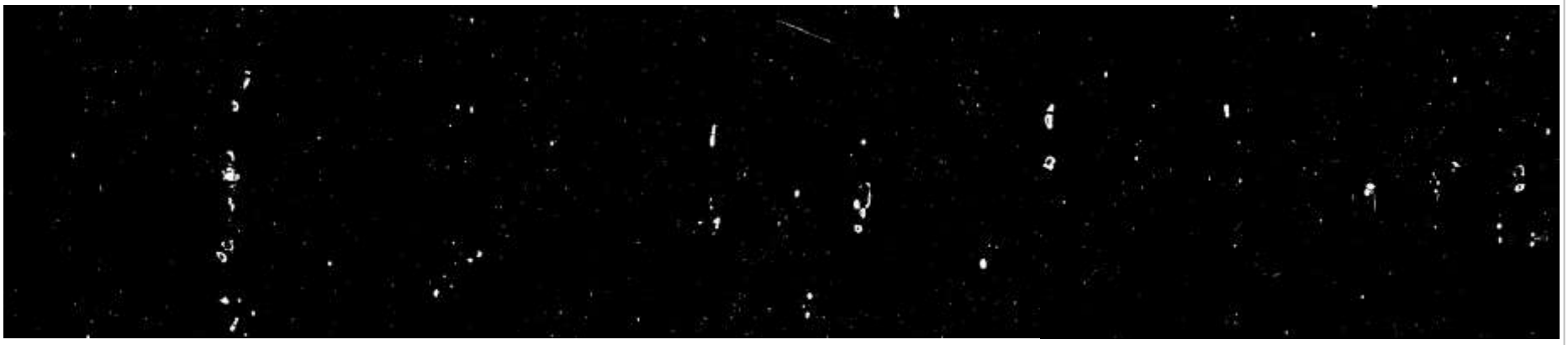

Figure 62 – Microstructure and precipitate count of 500°C 192h heated sample

a) Electrolytic-etched microstructure of 600°C 192h specimens

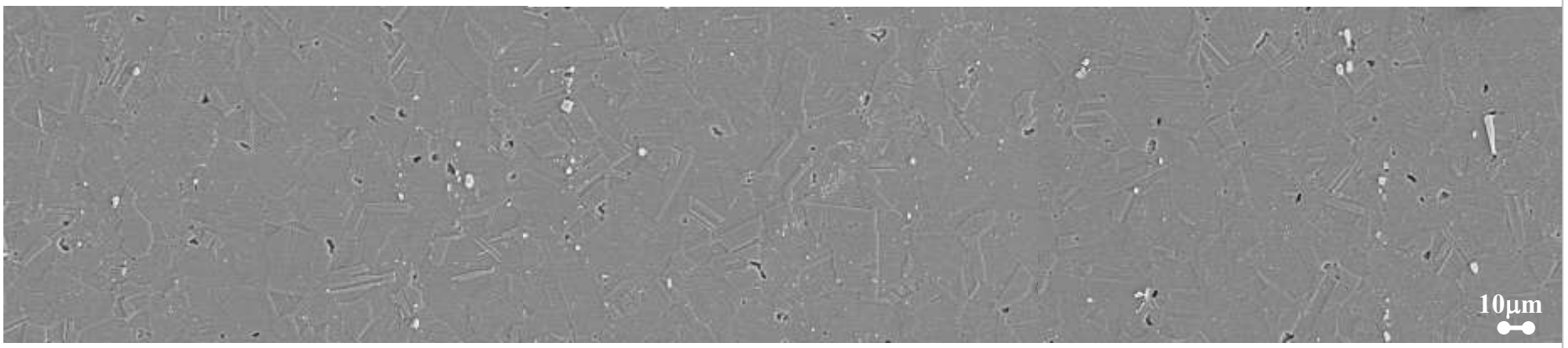

b) Precipitate contrasts (total of individual precipitates = 2264)

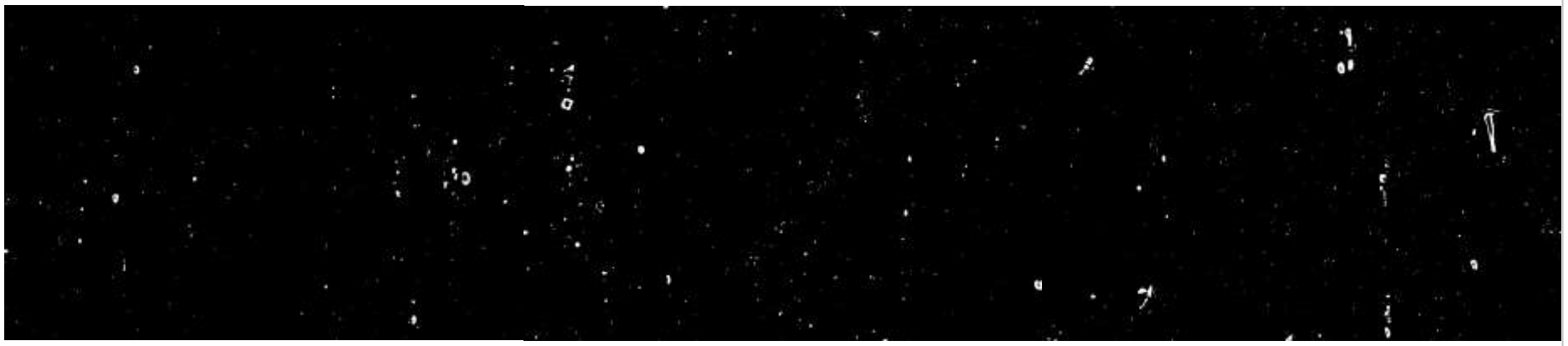

Figure 63 – Microstructure and precipitate count of 600°C 192h heated sample

a) electrolytic-etched microstructure of 800°C 192h specimens

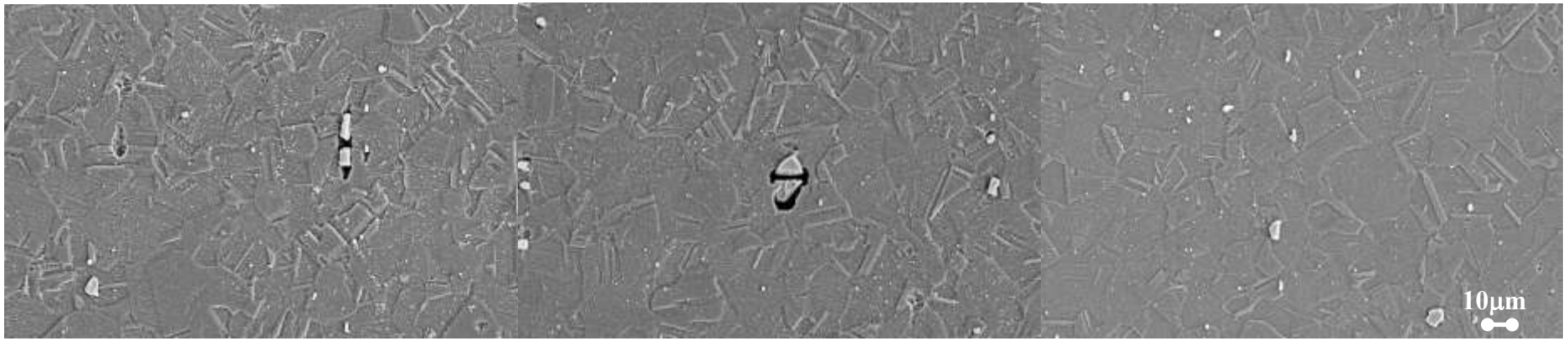

b) Precipitate contrasts (total of individual precipitates = 1580)

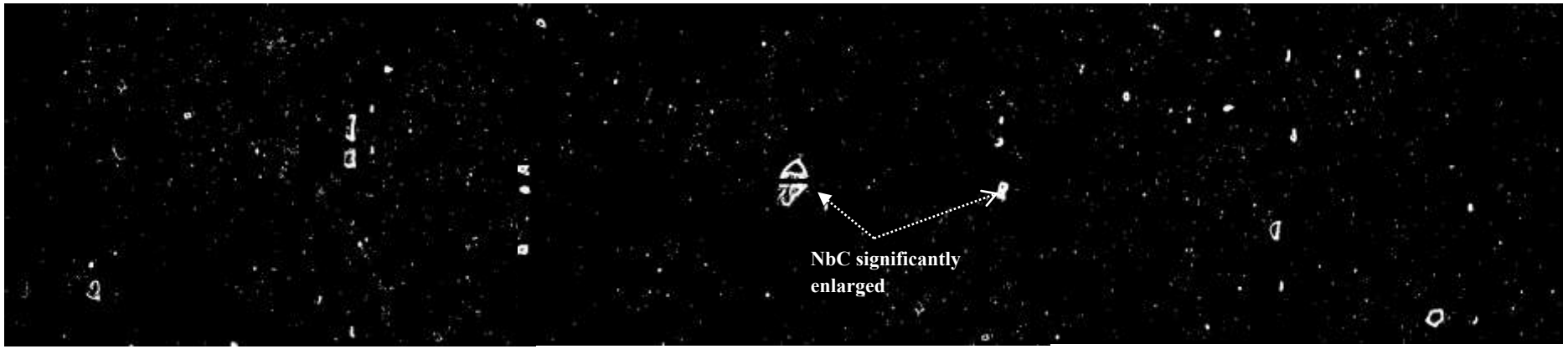

Figure 64 – Microstructure and precipitate count of 800°C 192h heated sample

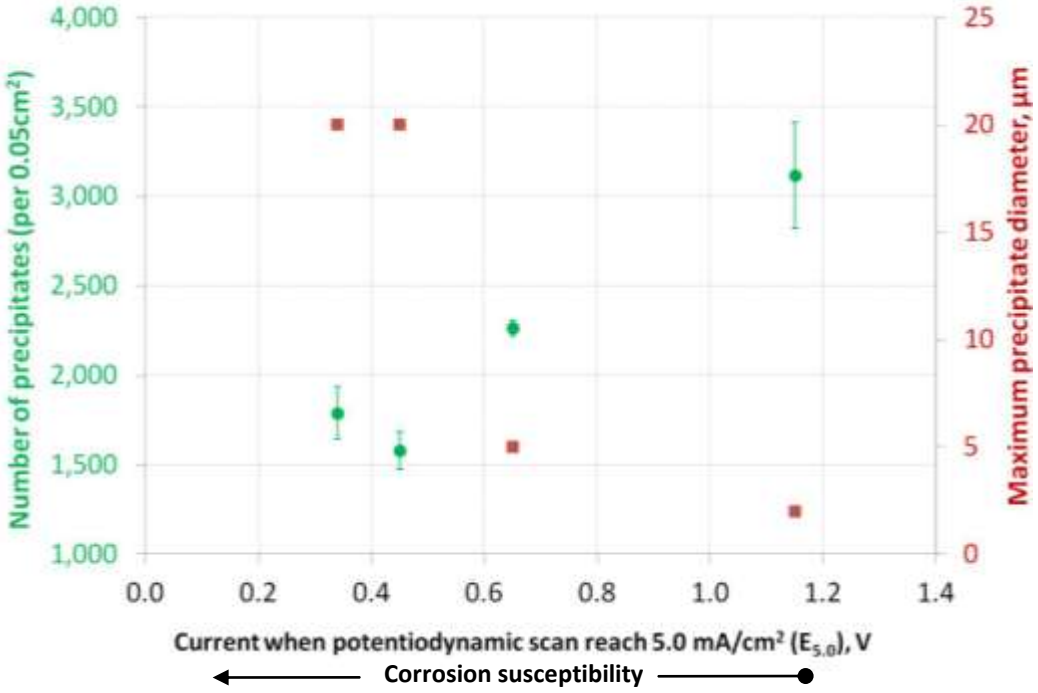

Sample	$E_{5.0}$ (v.s Ag|AgCl)	Number of Precipitates (/0.05cm²)	Maximum Precipitate Diameter (µm)	Average Grain Size in Matrix (µm)
As-received	1.15V	3115±296	~2	25
500° C 192h	0.34V	1789±146	~20	15
600° C 192h	0.65V	2264±44	~5	15
800° C 192h	0.45V	1580±105	~20	10

Figure 65 – Variation in number of precipitates and maximum precipitate diameter with $E_{5.0}$

35) that produces $E_{5.0}$ of 0.45V and below (~800mV difference from the as-received samples), their precipitate size were generally larger with maximum diameter ~20 µm and precipitate count lower <1789±146 (/0.05cm^2). The increase in sample's corrosion susceptibility with size is consistent with the results of Bohni *et al.* [15] whose work on MnS similarly suggests that a critical precipitate size is necessary for initiation of corrosion chemistry (Figure 22b). Note that in the case where the samples were not heated at the critical temperatures, i.e. the 600°C 192h specimens which measured intermediate $E_{5.0}$ of 0.65V, the precipitate counts are on average

2264±44 (/0.05cm^2) whereas the precipitate size were ~5 µm, values that falls between the as-received cladding and the 500°C 192h and 800°C 192h samples.

Figures 61 to 64 also shows that the austenite-γ grain sizes in the matrix are smaller, ~15 µm or less, when heated at the critical temperature and time compared to the ~25 µm austenite grains in the as-received cladding. Note that the FIB-sections of the as-received AGR fuel cladding (Figure 47) show austenite grains of at least 3 by 3 µm or larger (full elucidation limited by FIB-section size) whereas those heat-treated, for example the 600°C 192h sample (Figure 54), have smaller grains as small as 1.0 by 0.5 µm. Since smaller grain sizes within the bulk metal increase grain boundary availability, and together with the observations that NbC grows with heat-treatment, it can be suggested that heat treatment may increase the *probability of NbC contact with austenite-γ grain boundaries*, schematically illustrated in Figure 66.

As a summary, this section shows the varied *microstructural distribution* between the as-received AGR fuel cladding and those due to heat treatment that are important to substantiate the findings established from FIB-sections analyses in section 4.3 of the bulk metal. Whilst the FIB-sections have enabled precise quantification of chemical composition in the NbC precipitates, the austenite-γ matrix and their interfaces and high resolution imaging on the internal structure of corrosion, each of them, however, only represent a very small region (~4 µm subsurface thickness by 10 µm wide) within the bulk metal. It is not practical to produce enough FIB-sections and to statistically analyse the microstructural

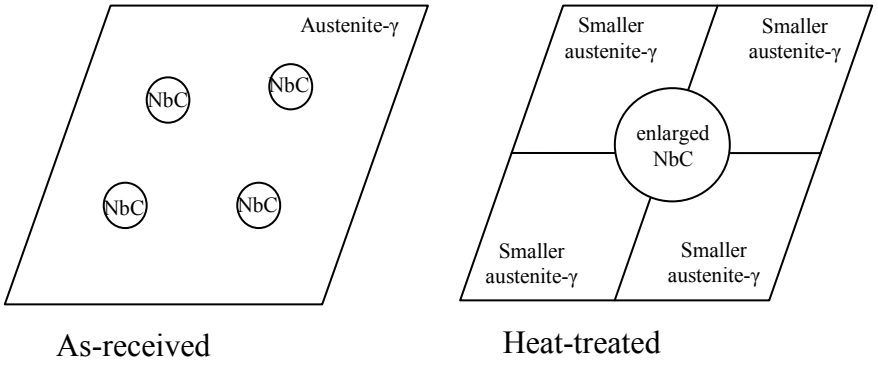

Figure 66 – Illustration of increased probability of NbC grain boundary contact with the austenite matrix (γ) with heat treatment

distribution of key phases in the bulk metal. Therefore, the development of etchant and subsequent image analysis has been a reliable approach to compare the microstructures across a wider area within a sample. Indeed, the observation that it is the large NbC precipitates between 5 to 20 μm causing corrosion susceptibility agrees very well with those previously obtained from the FIB-sections' analyses (section 4.3). The relationship between $E_{5.0}$ with both the precipitate count and precipitate size shown in Figure 65 indicates that they are the two most important microstructural distribution features that are correlated to a high-corrosion AGR cladding. These observations also agree well with the results of Bohni *et al.* [15] who suggest that the role of MnS precipitates in stainless steel 316L corrosion initiation are profound above a critical precipitate size of 1.0 μm dia. (Figure 22). In the case of AGR cladding the $E_{5.0}$ values indicative of corrosion susceptibility are profound *above* a precipitate diameter of 1.0 μm and in microstructures that have lower precipitate counts as a result of their growth into larger particles.

5.0 Summary – Importance of Microstructure to AGR Fuel Cladding Corrosion

Successful corrosion control of spent AGR fuel during interim storage at Sellafield has traditionally employed a corrosion inhibitor, specifically caustic soda (NaOH) at pH 11.4, to prevent fuel cladding corrosion in the *AGR Storage Pond* in which the spent fuels are immersed. In THORP's *Receipt and Storage Pond*, however, corrosion inhibitors cannot be employed due to a mix of cladding and container metals from both the AGRs and LWRs (Chapter 1). Although acceptable corrosion control has been achieved by the current demineralised-water storage at pH 7, the need to store them for a further 80 years under NDA's strategic plan requires a demonstration of the fuel cladding integrity against corrosion and release of FPs. Furthermore, there have been concerns that environmental constituents (e.g. sea salt) accidentally introduced into the pool may accelerate corrosion. The focus of the investigation reported in this thesis is understanding of the physical microstructural aspects that underpin AGR fuel cladding corrosion. The findings may contribute to the scientific basis that informs long-term control, monitoring practice and storage decisions over the AGR fuel cladding lifetime.

Although many studies have clarified metal corrosion processes, both theoretically and experimentally, including the classic studies of Galvele, Laycock, Newman, Pickering and Frankel (Section 2.5), there has to date been no explanation that fully describes the phenomena in AGR fuel cladding. This is because corrosion processes specific to the AGRs involve concurrently a number of microstructural factors, e.g. radiation damage, sensitisation, passive film oxidation and stress, that involve radionuclides and occur at the nanometre scale so making elucidation difficult. In this thesis, AGR fuel cladding samples sourced from Sellafield Ltd, cut and individually heat treated at temperatures from 400 to 800°C for 24 to 192h were characterised both in terms of their corrosion behaviour and of microstructure. Since the principal goal was to contrast microstructural features attributable to corrosion susceptibility, the characterisation techniques employed were corrosion measurements using the anodic polarisation method and microscopy techniques using the SEM, FIB, TEM and EDS analyses (Chapter 3) which revealed the

geometry, distribution and composition of grains, secondary phases and grain boundaries that have evolved.

Corrosion behaviour measurements using the anodic polarisation method are commonly made to measure a metal's corrosion performance. The cut samples were formed as electrodes and an electrode potential applied from zero to 1.6V (limit of oxygen evolution) in reference to the Ag|AgCl electrode potential (the potential that our measurements are referenced against). Figure 31 in Section 4.1 summarises the electrode potential when dissolution current density reaches 5.0 $mA.cm^{-2}$, $E_{5.0}$. With $E_{5.0}$, the relative corrosion susceptibility of the samples was compared, both across the heat treatment temperatures and times and in electrolyte concentrations of 0.001M and 0.1M. The $E_{5.0}$ values were 1.47±0.27V in the 0.001M electrolyte-NaCl and 0.66±0.14V in the 0.1M electrolyte-NaCl – about 800mV difference per two decades of chloride concentrations. As expected, a high chloride concentration adversely impacts AGR fuel cladding corrosion and this result confirms that chloride levels should be kept to a minimum in the *Receipt and Storage Ponds*. The $E_{5.0}$ measurements further revealed that samples from heating temperatures of 500°C and 800°C (Figure 34) and a heating time of 192h (Figure 35) exhibit the highest corrosion rates, consistently observed in both electrolyte concentrations. Specifically, the 500°C 192h ($E_{5.0}$ = 0.34V) and 800°C 192h ($E_{5.0}$ = 0.45V) samples were compared with the 600°C 192h ($E_{5.0}$ = 0.65V) and as-received samples ($E_{5.0}$ = 1.15V) to elucidate the critical microstructural features that impact on its corrosion behaviour. Note that the lower $E_{5.0}$ value indicates the more corroded samples since that applied potential is already enough to drive a dissolution current to 5.0 $mA.cm^{-2}$.

Figure 67 summarises the main findings that are important considerations in developing a safety case for the fuel cladding integrity during wet storage. By employing various microscopy techniques on the post-polarised electrodes to examine the corrosion morphologies and its internal structures, corroborative evidence has been obtained that niobium carbide (NbC) second phases are a critical element that underpins AGR cladding aqueous corrosion behaviour, and are involved in most of the pitting and crevice morphologies encountered. Paradoxically, NbC is the principal precipitation strengthening particle in the AGR fuel cladding added in the austenite-γ metal up to 0.7 %wt (Table 1). Analogous to the results of Bohni *et al.*

[15], Ryan *et al.* [13] and Williams *et al.* [14] on the role of MnS inclusion in stainless steel 316 corrosion and Buchheit *et al.* [94] and Suter and Alkine [95] who described corrosion around Al_2CuMg (S-phase) in aluminium alloy, the roles of NbC in AGR fuel cladding corrosion are clarified by the following observations:

I. The pitting **corrosion morphologies**, if not occurring as open hemispherical cavities that are freely exposed to the bulk environment, occur predominantly *around NbC*. SEM examination shows extensive corrosion around NbC precipitates even though they themselves remain well-maintained and geometrically-intact (e.g., in Figure 40). This observation suggests that a localised galvanic couple may have formed where the NbC precipitate *may act as a cathode* in the participating galvanic dissolution processes and the adjacent austenite-γ metal is the anode that undergoes preferential oxidation. FIB-sections (Figures 50, 53, 54, 56 and 58) show austenite-γ metal dissolution where proportionally large (~2 by 5 μm) subsurface cavities and ~0.1 μm dia. voids were formed between NbC and bulk austenite-γ indicative of dissolution processes occurring or that have occurred.

II. The pitting corrosion morphologies that occur around the NbC precipitates exhibit four important **dissolution characteristics** indicated by examining localised pits in detail:

    i) *Lacy Corrosion Cover*

    SEM examination shows bulk austenite-γ dissolution in the form of lacy corrosion covers around NbC precipitates. Figure 39a shows two lacy corrosion covers ~10 to 20 μm dia. that evolve around the NbC precipitates and extend beneath the surface plane. Cross-section examination shows that the covers have width-depth ratio between 1.6 to 2.6, although their actual size varies locally depending on the site. Note that the lacy corrosion covers previously described by Ernst *et al.* [66, 76] for thin stainless steel foils and Laycock *et al.* [54] for bulk metals were not associated by them with any secondary phases as have been demonstrated in this investigation.

ii) *Dissolved Metal Regions along NbC Peripheries*

Chemical analyses (EDS) on FIB-sections show that the interface between NbC precipitates and bulk austenite-γ contains a thin envelope (~ 1 μm thickness) of *dissolved-metal regions along the NbC peripheries.* Specifically, the dissolved-metal region is characterised by substantially decreased alloying element concentration compared to its nominal austenite-γ composition (50.3±1.7 at% Fe, 21.0±1.1 at% Cr and 21.0±0.4 at% Ni). On average, the dissolved-metal region exhibits 20%, 21% and 17% reduction in Fe, Ni and Cr, respectively. In certain sites, for example Site D in Figure 56, the metal-dissolved regions contain no chromium, rendering the localised region in question non-stainless and susceptible to the slightest driving force for corrosion initiation. Alterations to the bulk austenite-γ in the presence of NbC precipitates, albeit at selected sites, show that there exists a preferential and accelerated attack on the austenite-γ (anode) member within a localised galvanic couple.

iii) *Diffusion-Controlled Mechanisms of Austenite-γ Dissolution*

The corrosion morphologies exhibit a *smooth* concaved pit bottom, both as open hemispherical cavities that are freely exposed to the bulk environment (e.g. Figure 39c) or as shielded cavities beneath a lacy corrosion cover (e.g. Figure 42 and Figure 43). The smooth pit bottoms indicate that diffusion-controlled mechanisms were involved in the austenite-γ dissolution processes, potentially similar to the pit-acidification theory suggested by Galvele [61]. As he pointed out, at its start metal dissolution may occur at the bottom of the pit which is followed by a self-sustaining pit-acidification mechanism that enables the pit to grow until a steady state condition is reached.

iv) *Enhanced Austenite-γ Dissolution in Microstructures with High Dislocation Densities*

FIB-sections revealed samples that exhibit comparatively high corrosion susceptibility – e.g., the 500°C 192h ($E_{5.0}$ = 0.34V) and

800°C 192h ($E_{5.0}$ = 0.45V) electrodes – show high dislocation densities in their austenite-γ metal matrix. The presence of dislocations, thus high-stressed regions in the microstructure, is also accompanied by large ~5 μm dia. NbC precipitates (e.g. Figures 50b and 51a). In the samples that are relatively corrosion noble – e.g. the 600°C 192h ($E_{5.0}$ = 0.65V) and as-received ($E_{5.0}$ = 1.15V) electrodes – the NbC precipitates sizes are small (~0.1 μm dia.) and ~10 of them are homogeneously distributed within an observable FIB-section area of typically 10 μm wide by 4 μm deep from the surface (e.g. Figure 47). These contrasting features show the growth of fine NbC precipitates into larger inclusions due to heat treatment during which dislocation densities also increase. The growth of NbC precipitates above a certain critical size, parallel to the suggestion by Bohni *et al.* [15] and along with subsequent increased stress generation, may be responsible for the adverse impact on cladding corrosion.

Whilst FIB-sections have enabled precise quantification of chemical composition of the NbC precipitates, the austenite-γ grains and the *dissolved-metal* interfaces, as well as high resolution imaging of the internal structure of corrosion, only a small area (~4 μm subsurface thickness by 10 μm wide) is examined within the bulk metal. Since it is impractical to examine enough FIB-sections to get statistically significant understanding of bulk material the electrodes were etched in oxalic acid solution to reveal the bulk-scale microstructures that are critical to corrosion. Specifically, the highly corroded 500°C 192h ($E_{5.0}$ = 0.34V) and 800°C 192h ($E_{5.0}$ = 0.45V) samples show behaviour attributed to their large ~20 μm dia. NbC precipitates and small ~15 μm dia. austenite-γ grains. The 600°C 192h ($E_{5.0}$ = 0.65V) and as-received ($E_{5.0}$ = 1.15V) electrodes, the relatively corrosion-noble ones that give corrosion stability to the AGR cladding, contained fine ~0.1 μm NbC precipitates that are homogeneously distributed with large ~25 μm austenite-γ grains. These observations suggest that corrosion susceptibility is proportional to both the increase in NbC precipitate size and decrease in austenite- γ grain size.

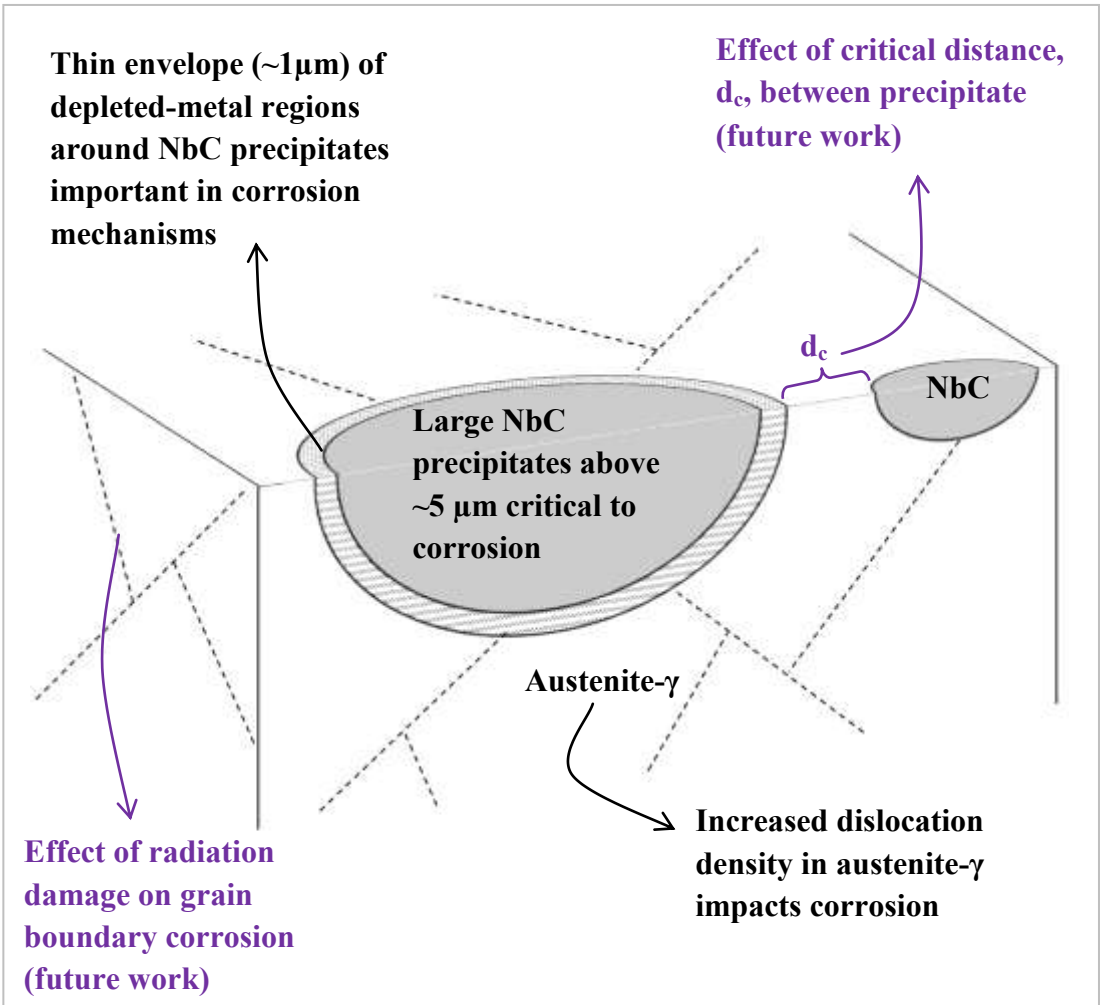

Figure 67 – Illustration of AGR fuel cladding microstructures that underpin its corrosion behaviour

6.0 Conclusions and Recommendations for Further Study

The focus of the investigation reported in this thesis is the impact of microstructure and secondary phase formation on Advanced Gas-Cooled Reactor (AGR) fuel cladding corrosion in chloride aqueous solutions, amongst other known corrosion factors which include radiation-induced segregation and thermal sensitisation. An understanding of the AGR fuel cladding microstructure that may underpin its corrosion behaviour has been established. There are several important considerations in developing a safety case for the fuel cladding integrity during long-term storage. Primarily, NbC precipitates are strongly correlated to corrosion susceptibility in wet storage, encountered in most pitting corrosion morphologies. Even though NbC is the principle precipitation strengthening particle in the austenitic 20Cr/25Ni/Nb fuel cladding providing improved resistance to irradiation creep and fuel swelling during reactor operation, corrosion morphologies were mostly present around NbC precipitates. Both SEM and FIB-section examination show that the bulk austenite-γ metal around NbC precipitates exhibits extensive corrosion. The principal mechanism through which the NbC acts is potentially as the *cathode of a localised galvanic couple* where the surrounding austenite-γ matrix is the sacrificial anode preferentially dissolved. This dissolution process is likely to involve a diffusion-controlled process, potentially a pit-acidification step since the bottoms of the pits are often smooth as observed under the lacy corrosion covers and subsurface features in FIB-sections. Dissolution is more profound in samples that i) were tested in high chloride concentrations, ii) contain NbC precipitates greater than ~5 μm dia., iii) exhibit high dislocation densities in their microstructure and iv) have small austenite-γ grain sizes (~15 μm dia.). Accounting for all potential possibilities of AGR spent fuel safe store, both wet and dry, these results suggest that aqueous contact with chloride must be avoided when possible and development of corrosion inhibitors should be focussed on NbC precipitate mechanisms.

Not all aspects of the AGR fuel cladding microstructure have been covered to provide a complete the description of its corrosion phenomenology. The principle challenge lies in the difficulties to procure, process and examine radioactive materials. Nonetheless, continuing on the successful demonstration of a combined corrosion measurements and creative microscopy techniques, there are five further study areas that should be pursued to add to the current knowledge base:

I. *Heavy-Water Studies for Pitting Corrosion Mechanisms*

Whilst FIB-sections obtained from carefully selected lacy corrosion cover and active corrosion sites have successfully revealed the internal structure of corrosion processes, one of the first employed in studying active corrosion sites, further characterisation of cladding corrosion mechanisms could be performed using heavy water (D_2O) as a tracer-electrolyte with a broader range of corrosion inhibitor solution which includes sulphate (SO_4^{2-}), thiosulphate ($S_2O_3^{2-}$) and nitrate (NO_3^{2-}). Its electrochemical behaviour is the same as that of normal water (H_2O) but *its location* in the subsurface corrosion cavities and pit can be distinguished, leading to information that relates to the nature of the galvanic interaction between the NbC precipitate and bulk austenite-γ metal and pit-acidification condition in corrosion processes. In addition, residual electrolytes from the post-anodic polarisation experiments could be analysed for the concentrations of dissolved ion, e.g. iron, chromium, and nickel using Inductively-Coupled Plasma Mass Spectrometry (ICP-MS).

II. *Effect of Grain Boundary Chromium Depletion on Corrosion*

One of the limitations to providing an overall and encompassing microstructure perspective to AGR fuel cladding corrosion has been that the current facility has not been equipped to examine the corrosion of cladding that has been processed in a reactor. Whilst this study has adopted simulated conditions by thermal-aging to investigate the impact of a variety of secondary phase formation, the *in-situ* grain boundary chromium depletion condition due to neutron-irradiation as pointed out by Norris *et al.* [18, 19] needs to be understood for a complete understanding of corrosion behaviour. The next steps should focus on mimicking materials of varying grain boundary-damaged microstructures at proton- or neutron- irradiation facilities to be tested for its corrosion impact. Such samples can be characterised with the experimental capabilities that have been developed and demonstrated in this thesis. In addition, localised corrosion measurements could be performed using microcapillaries as electrochemical cells (e.g., developed by Suter *et al.* [95]), sensitive down to pA and fA current measurements and involve only a small ~1.0 μm dia. exposed

surface area (as opposed to cm^2 exposed area in this study), to investigate growth and evolution of NbC corrosion mechanisms.

III. *In-situ Corrosion Monitoring Methods*

The corrosion measurement technique that has been employed in this study is the anodic polarisation method – an accelerated measure of the metal's corrosion performance under deliberately applied electrode potentials. Whilst electrode potential measurements have successfully compared *in relative terms* the corrosion performance of the heat-treated specimens, the AGR spent fuels in the ponds are, however, subjected to a 'true' corroding-potential or the open circuit potential (OCP). One important work is to develop a correlation between the laboratory-measured electrode potentials to its actual environmental performance (e.g. its OCP) since the spent fuels will undergo a foreseeable storage time before either the resumed reprocessing schedules or disposal in a geological repository can be undertaken.

IV. *Role of Salt Films*

That the presence of chloride accelerates corrosion processes is well-known. Further to the chloride-induced diffusion theories developed (e.g., Galvele [61]) and corrosion initiation mechanisms proposed (e.g., Ernst *et al.* [55]) to clarify metal dissolution processes, one of the issues that can be investigated is the mechanical and electrochemical effect of salt crystallisation in pit formation. In observing the formation of salt crystals in post-polarised electrodes that are deliberately un-rinsed (e.g., Figure 46), it is likely that salt crystallisation effects, including stresses imparted on the metal surface and modification of the surface tension by the salt deposits, may be important in the initial steps of corrosion processes. Further experimentation with instrumentation that can provide metal density data or surface sensitive measurements (e.g., skin current or surface acoustic waves) should be useful in elucidating the evolution of metal corrosion *under* the salt films.

V. Role of Stress in Corrosion

Corrosion susceptible specimens contained grown, large NbC precipitates (~5 μm) that have increased dislocation densities in their adjacent austenite-γ microstructures. It possible that there is a thermal expansion mismatch between the NbC and austenite-γ metal during the heat treatment, causing the increased dislocation densities. One important aspect to investigate is the extent to which stress in the AGR metal impacts corrosion. Potential experiments that can be conducted would involve annealing out the dislocations and repeat the corrosion measurements.

7.0 References

1. Seinfeld, J.H. and S.N. Pandis, *Atmospheric Chemistry and Physics: From Air Pollution to Climate Change*. 2nd ed. 2006, Hoboken, NJ , Chichester: Wiley, John Wiley. 1203.
2. Standring, P.N. *The Long Term Storage of Advanced Gas-Cooled Reactor (AGR) Fuel*. in *Storage of Spent Fuel from Power Reactors*. 1999. Vienna, Austria: International Atomic Energy Agency (IAEA).
3. Hands, B.J., *Investigation of the Viability of Demineralised Water as a Long Term Storage Medium for AGR Fuel*, BNFL Commercial Reports, 2005, Copyright © British Nuclear Fuels Plc.
4. Herbert, D., G.O.H. Whillock, and S.E. Worthington, *Zero Resistance Ammetry - Its Application in Preventing the Corrosion of Stainless Steel in Cooling Waters.* Materials Science Forum, 1995. **192-194**: p. 469-476.
5. Hands, B.J., *Alternative Corrosion Inhibitors for Long Term AGR Fuel Storage*, BNFL Commercial Reports, 2005, Copyright © British Nuclear Fuels Plc.
6. Hands, B.J., *A New IGA Sensor Design as an Alternative to Active Brace Tests*, BNFL Commercial Reports, 2005, Copyright © British Nuclear Fuels Plc.
7. Glasgow, B. B., Siahmed, A., Wolfer, W. G. and Garner, F. A., *Helium Bubble Formation and Swelling in Metals.* Journal of Nuclear Materials, 1982. **103**(1-3): p. 981-986.
8. Newman, R.C., Newman, R. C., Wong, W. P., Ezuber, H. and, Garner, A., *Pitting of Stainless Steels by Thiosulfate Ions.* Corrosion, 1989. **45**(4): p. 282-287.
9. ATI Allegheny Ludlum Brochure, *Technical Data Blue Sheet: ATI 20-25+Nb Alloy*, 2009, Allegheny Technologies Incorporated.
10. Westinghouse Electric Company Brochure, *Nuclear Fuel Manufacture at Springfields*, 2008, Westinghouse Electric Company.
11. Stobbs, J.J. and A.J. Swallow, *Effects of Radiation on Metallic Corrosion.* Metallurgical Review, 1962. **7**(25): p. 95-132.

12. Powell, D.J., R. Pilkington, and D.A. Miller, *The Precipitation Characteristics of 20Cr/25Ni/Nb Stabilised Stainless Steel.* Acta Metallurgica, 1988. **36**(3): p. 713-724.
13. Ryan, M. P., Williams, D. E., Chater, R. J., Hutton, B. M. and McPhail, D. S, *Why Stainless Steel Corrodes.* Nature, 2002. **415**(6873): p. 770-774.
14. Williams, D. E., Kilburn, M. R., Cliff, J. and Waterhouse, G. I. N., *Composition Changes Around Sulphide Inclusions in Stainless Steels and Implications for the Initiation of Pitting Corrosion.* Corrosion Science, 2010. **52**(11): p. 3702-3716.
15. Bohni, H., T. Suter, and F. Assi, *Micro-electrochemical Techniques for Studies of Localized Processes on Metal Surfaces in the Nanometer Range.* Surface & Coatings Technology, 2000. **130**(1): p. 80-86.
16. Evans, H.E. and R.C. Lobb, *Conditions for the Initiation of Oxide Scale Cracking and Spallation.* Corrosion Science, 1984. **24**(3): p. 209-222.
17. Millward, G. R., Evans, H. E., Jones, I. P. and Eley, C. D., *Carbon Deposition on Stainless Steel in Oxidising Environments.* Materials at High Temperatures, 2003. **20**(4): p. 535-541.
18. Norris, D.I.R., C. Baker, and J.M. Titchmarsh, *A Study of Radiation-Induced Sensitization in 20/25/Nb Steel by Compositional Profile Measurements at Grain Boundaries*, 1987, British Library: London. p. 277.
19. Ashworth, M.A., D.I.R. Norris, and I.P. Jones, *Radiation-Induced Segregation in Fe-20Cr-25Ni-Nb Based Austenitic Stainless Steels.* Journal of Nuclear Materials, 1992. **189**(3): p. 289-302.
20. Waddington, J.S. and R.B. Jones. *Properties of Stainless Steel Cladding for Use in Advanced Gas-Cooled Reactors*. in *Physical Metallurgy of Reactor Fuel Elements*. 1973. Berkeley Nuclear Laboratories, Gloucestershire: The Metals Society.
21. Davis, J.R. and ASM International Handbook Committee., *Metals Handbook*. Desk ed. 1998, Materials Park, Ohio USA: ASM International. 1521.
22. Ng, K.K., *Complete Guide to Semiconductor Devices*. 2nd ed. 2002, New York: Wiley. 740.
23. Hampel, C.A., *Rare Metals Handbook*. 2nd ed. 1961: Reinhold. 715.
24. He, Y. D., Li, Z. W., Qi, H. B. and Gao, W., *Standard Free Energy Change of Formation per Unit Volume: A New Parameter for Evaluating Nucleation*

and Growth of Oxides, Sulphides, Carbides and Nitrides. Materials Research Innovations, 1997. **1**(3): p. 157-160.

25. Sourmail, T., *Precipitation in Creep Resistant Austenitic Stainless Steels.* Materials Science and Technology, 2001. **17**(1): p. 1-14.
26. Beddoes, J. and J.G. Parr, *Introduction to Stainless Steels*. 3rd ed. 1999, Materials Park, Ohio USA: ASM International. 315.
27. Millward, G. R., Evans, H. E., Aindow, M. and Mowforth, C. W., *The Influence of Oxide Layers on the Initiation of Carbon Deposition on Stainless Steel.* Oxidation of Metals, 2001. **56**(3-4): p. 231-250.
28. Millward, G. R., Evans, H. E., Jones, I. P., Eley, C. D. and Simpson, K. A., *Burn-off of Filamentous Carbon and Subsequent Re-deposition on a 20Cr25Ni Austenitic Steel.* Materials at High Temperatures, 2009. **26**(1): p. 57-61.
29. Martin, J.W., *Precipitation Hardening*. 2nd ed. 1998, Oxford: Butterworth-Heinemann. 256 p.
30. Merica, P.D., *The Precipitation-Hardening of Metals.* Journal of the Franklin Institute, 1942. **234**(2): p. 137-146.
31. Merica, P.D., R.G. Waltenberg, and H. Scott, *The Heat Treatment of Duralumin.* Journal of the Franklin Institute, *1919*. **188**(4): p. 549-550.
32. BNFL Brochure, *Oxide Fuels for the Worlds Energy Suppliers: New Oxide Fuels Complex*, 2008, Copyright © British Nuclear Fuels Plc .
33. Pocock, R.F., *Nuclear Power: Its Development in the United Kingdom*. 1977, Old Woking London: Unwin Brothers Ltd ; Institution of Nuclear Engineers. 272.
34. Olander, D., *Nuclear Fuels - Present and Future.* Journal of Nuclear Materials, 2009. **389**: p. 1-22.
35. Abram, T. and S. Ion, *Generation-IV Nuclear Power: A Review of the State of the Science.* Energy Policy, 2008. **36**(12): p. 4323-4330.
36. Weisman, J., *Elements of Nuclear Reactor Design*. 1977, Amsterdam ; Oxford: Elsevier.
37. Frost, B.R.T., *Nuclear Fuel Elements: Design, Fabrication and Performance*. Pergamon international library of science, technology, engineering and social sciences. 1982, Oxford: Pergamon.

38. Hill, J.F., *Textbook of Reactor Physics: An Introduction*. 1961, London: Allen and Unwin.
39. Grover, R.B., *Nuclear Energy: Emerging Trends.* Current Science, 2000. **78**(10): p. 1191-1195.
40. Lobb, R.C., *Observations on the Microstructure of 20Cr-25Ni-Nb Stainless Steel After Exposure to Iodine Vapor during Creep at 750C.* Oxidation of Metals, 1981. **15**(1-2): p. 147-167.
41. Hejzlar, P., Todreas, N. E., Shwageraus, E., Nikiforova, A., Petroski, R. and Driscoll, M. J., *Cross-comparison of Fast Reactor Concepts with Various Coolants.* Nuclear Engineering and Design, 2009. **239**(12): p. 2672-2691.
42. Krane, K.S. and D. Halliday, *Introductory Nuclear Physics*. 1988, Hoboken, NJ: John Wiley & Sons, Inc. 845.
43. Marsh, G. P., Taylor, K. J., Bryan, G. and Worthington, S. E., *The Influence of Radiation on the Corrosion of Stainless Steel.* Corrosion Science, 1986. **26**(11): p. 971-982.
44. Damcott, D.L., T.R. Allen, and G.S. Was, *Dependence of Radiation-Induced Segregation on Dose, Temperature and Alloy Composition in Austenitic Alloys.* Journal of Nuclear Materials, 1995. **225**: p. 97-107.
45. Marwick, A.D., *Segregation in Irradiated Alloys - Inverse Kirkendall Effect and Effect of Constituition on Void Swelling.* Journal of Physics F-Metal Physics, 1978. **8**(9): p. 1849-1861.
46. Nakajima, H., *The Discovery and Acceptance of the Kirkendall Effect: The Result of a Short Research Career.* Jom-Journal of the Minerals Metals & Materials Society, 1997. **49**(6): p. 15-19.
47. Watanabe, S., Sakaguchi, N., Hashimoto, N., Nakamura, M., Takahashi, H., Namba, C. and Lam, N. Q., *Radiation-Induced Segregation Accompanied by Grain Boundary Migration in Austenitic Stainless Steel.* Journal of Nuclear Materials, 1996. **232**(2-3): p. 113-118.
48. Simonen, E.P. and S.M. Bruemmer, *Radiation Effects on Environmental Cracking of Stainless Steels.* Journal of the Minerals Metals & Materials Society, 1998. **50**(12): p. 52-55.
49. Smallman, R.E., *Physical Metallurgy and Advanced Materials Engineering*, 2007, Elsevier.

50. Yakabuskie, P.A., J.M. Joseph, and J.C. Wren, *The Effect of Interfacial Mass Transfer on Steady-State Water Radiolysis.* Radiation Physics and Chemistry, 2010. **79**(7): p. 777-785.
51. Wyllie, W.E., D. Steiner, and D.J. Duquette, *The Effect of Water Radiolysis on the Stress Corrosion Behavior of UNS S31600 Stainless Steel at 50 and 90 degrees C.* Journal of Nuclear Materials, 1996. **233**: p. 1372-1377.
52. IAEA Technical Document, *Further Analysis of Extended Storage of Spent Fuel*, 1996, Document Number: IAEA-TECDOC-944, International Atomic Energy Association (IAEA) Publication: Vienna.
53. Sedriks, A.J., *Corrosion of Stainless Steels*. 2nd ed. Corrosion monograph series. 1996, New York ; Chichester: John Wiley.
54. Laycock, N.J. and R.C. Newman, *Localised Dissolution Kinetics, Salt Films and Pitting Potentials.* Corrosion Science, 1997. **39**(10-11): p. 1771-1790.
55. Ernst, P., Laycock, N. J., Moayed, M. H., and Newman, R. C., *The Mechanism of Lacy Cover Formation in Pitting.* Corrosion Science, 1997. **39**(6): p. 1133-1136.
56. Sugimoto, K. and Y. Sawada, *Role of Molybdenum Additions to Austenitic Stainless-Steels in Inhibition of Pitting in Acid Chloride Solutions.* Corrosion Science, 1977. **17**(5): p. 425-445.
57. Evans, H.E. and R.C. Lobb, *The Influence on Oxide Spallation of Annealing Periods During a Cooling Cycle.* Corrosion Science, 1993. **35**(5-8): p. 999-1005.
58. Taylor, C.D., *The Transition from Metal-Metal Bonding to Metal-Solvent Interactions During a Dissolution Event as Assessed from Electronic Structure.* Chemical Physics Letters, 2009. **469**(1-3): p. 99-103.
59. Frankel, G.S. and N. Sridhar, *Understanding Localized Corrosion.* Materials Today, 2008. **11**(10): p. 38-44.
60. Deforce, B. and H. Pickering, *A Clearer View of How Crevice Corrosion Occurs.* Journal of the Minerals Metals & Materials Society, 1995. **47**(9): p. 22-27.
61. Galvele, J.R., *Transport Processes and Mechanism of Pitting of Metals.* Journal of the Electrochemical Society, 1976. **123**(4): p. 464-474.
62. Galvele, J.R., *Transport Processes in Passivity Breakdown-II Full Hydrolysis of the Metal Ions.* Corrosion Science, 1981. **21**(8): p. 551-579.

63. Szklarska-Smialowska, Z., *Pitting Corrosion of Metals*. 1986, Houston, Tex.: National Association of Corrosion Engineers.
64. Soltis, J., D. Krouse, and N. Laycock, *Localised Dissolution of Iron in Buffered and Non-Buffered Chloride-Containing Solutions.* Corrosion Science, 2011. **53**(6): p. 2152-2160.
65. Linhardt, P., G. Ball, and E. Schlemmer, *Electrochemical Investigation of Chloride Induced Pitting of Stainless Steel under the Influence of a Magnetic Field.* Corrosion Science, 2005. **47**(7): p. 1599-1603.
66. Ernst, P. and R.C. Newman, *Pit Growth Studies in Stainless Steel Foils II: Effect of Temperature, Chloride Concentration and Sulphate Addition.* Corrosion Science, 2002. **44**(5): p. 943-954.
67. Scholz, F., *Electroanalytical Methods: Guide to Experiments and Applications*. 2002, Berlin ; London: Springer. 331.
68. Frankel, G.S., M. Stratmann, and A.J. Bard, *Encyclopedia of Electrochemistry*. 2003, Weinheim: Wiley-VCH. 745.
69. Delahay, P., *Double Layer and Electrode Kinetics*. 1965, New York: Interscience Publishers. 321.
70. Monk, P.M.S., *Fundamentals of Electro-Analytical Chemistry*. Analytical techniques in the sciences. 2001, Chichester: Wiley. 361 p.
71. Piron, D.L., *The Electrochemistry of Corrosion*. 1991, Houston, TX: National Association of Corrosion Engineers.
72. Frankel, G.S., *Pitting Corrosion of Metals. A Review of the Critical Factors.* Journal of the Electrochemical Society, 1998. **145**(8): p. 2970-2970.
73. Gileadi, E., *The Enigma of Metal Deposition.* Journal of Electroanalytical Chemistry, 2011. **660**(2): p. 247-253.
74. Gileadi, E. and E. Kirowa-Eisner, *Some Observations Concerning the Tafel Equation and its Relevance to Charge Transfer in Corrosion.* Corrosion Science, 2005. **47**(12): p. 3068-3085.
75. Gileadi, E., *Can an Electrode Reaction Occur without Electron Transfer across the Metal/Solution Interface?* Chemical Physics Letters, 2004. **393**(4-6): p. 421-424.
76. Ernst, P. and R.C. Newman, *Pit Growth Studies in Stainless Steel Foils I: Introduction and Pit Growth Kinetics.* Corrosion Science, 2002. **44**(5): p. 927-941.

77. Tachibana, M., Ishida, K., Wada, Y., Aizawa, M. and Fuse, M., *Study of Polarization Curve Measurement Method for Type 304 Stainless Steel in BWR High Temperature-High Purity Water.* Journal of Nuclear Science and Technology, 2009. **46**(2): p. 132-141.

78. Lawes, G., A.M. James, and Analytical Chemistry by Open Learning (ACOL), *Scanning Electron Microscopy and X-ray Microanalysis*. Analytical chemistry. 1987, Chichester: Published on behalf of ACOL by Wiley.

79. Pardo, A., Merino, M. C., Coy, A. E., Viejo, F., Arrabal, R. and Matykina, E., *Pitting Corrosion Behaviour of Austenitic Stainless Steels - Combining Effects of Mn and Mo Additions.* Corrosion Science, 2008. **50**(6): p. 1796-1806.

80. Leach, R., Brown, L., Xiangqian, J., Blunt, R., Conroy, M. and Mauger, D., *Measurement Good Practice Guide No. 108. Guide to the Measurement of Smooth Surface Topography using Coherence Scanning Interferometry*, 2008, National Physics Laboratory.

81. Giannuzzi, L.A. and F.A. Stevie, *A Review of Focused Ion Beam Milling Techniques for TEM Specimen Preparation.* Micron, 1999. **30**(3): p. 197-204.

82. Munroe, P.R., *The Application of Focused Ion Beam Microscopy in the Material Sciences.* Materials Characterization, 2009. **60**(1): p. 2-13.

83. Phaneuf, M.W., *Applications of Focused Ion Beam Microscopy to Materials Science Specimens.* Micron, 1999. **30**(3): p. 277-288.

84. Ooi, T.N., McPhail, D. S., Chater, R. J. and Shollock, B. A., *Isotope Exchange Studies of Oxidation Mechanisms in Nickel-Base Superalloys using FIB-SIMS Techniques.* Surface & Coatings Technology, 2006. **201**(7): p. 3885-3888.

85. Overwijk, M.H.F., F.C. Vandenheuvel, and C.W.T. Bullelieuwma, *Novel Scheme for the Preparation of Transmission Electron-Microscopy Specimens with a Focused Ion-Beam.* Journal of Vacuum Science & Technology B, 1993. **11**(6): p. 2021-2024.

86. Williams, D.B. and C.B. Carter, *Transmission Electron Microscopy: A Textbook for Materials Science*. 2nd ed. 2009, New York ; London: Springer. 760.

87. Silk, J.R., R.J. Dashwood, and R.J. Chater, *Determination of Lattice Orientation in Aluminium Alloy Grains by Low Energy Gallium Ion-Channelling.* Nuclear Instruments & Methods in Physics Research Section B-Beam Interactions with Materials and Atoms, 2010. **268**(11-12): p. 2064-2068.
88. Weidmann, E., A. Guesnier, and B. Taylor, *Struers Application Note: Metallographic Preparation of Stainless Steel*, S. A/S, Editor 2005, Struers Ltd: Ballerup, Denmark.
89. Galvele, J.R., *Tafel's Law in Pitting Corrosion and Crevice Corrosion Susceptibility.* Corrosion Science, 2005. **47**(12): p. 3053-3067.
90. Laycock, N.J., J. Stewart, and R.C. Newman, *The Initiation of Crevice Corrosion in Stainless Steels.* Corrosion Science, 1997. **39**(10-11): p. 1791-1809.
91. Moayed, M.H. and R.C. Newman, *Deterioration in Critical Pitting Temperature of 904L Stainless Steel by Addition of Sulfate Ions.* Corrosion Science, 2006. **48**(11): p. 3513-3530.
92. Williams, G. and H.N. McMurray, *Localized Corrosion of Magnesium in Chloride-Containing Electrolyte Studied by a Scanning Vibrating Electrode Technique.* Journal of the Electrochemical Society, 2008. **155**(7): p. C340-C349.
93. Espinosa, R.M., L. Franke, and G. Deckelmann, *Phase Changes of Salts in Porous Materials: Crystallization, Hydration and Deliquescence.* Construction and Building Materials, 2008. **22**(8): p. 1758-1773.
94. Buchheit, R. G., Grant, R. P., Hlava, P. F., McKenzie, B., Zender, G. L., *Local Dissolution Phenomena Associated with S-phase (Al_2CuMg) Particles in Aluminum Alloy 2024-T3.* Journal of the Electrochemical Society, 1997. **144**(8): p. 2621-2628.
95. Suter, T. and R.C. Alkire, *Microelectrochemical Studies of Pit Initiation at Single Inclusions in Al 2024-T3.* Journal of the Electrochemical Society, 2001. **148**(1): p. B36-B42.

Appendices

Appendix 1 – MATLAB algorithm for electrode surface area determination

```
%OPEN THE IMAGE FILE
I=imread('A4PS.tif');
figure, imshow(I)
title ('Original Image');

%THRESHOLD THE IMAGE IMMEDIATELY
level=graythresh(I);
bw=im2bw(I,level);
figure, imshow(bw);
%title('Thresholded Image');

%FIND IMAGE OF THE LARGEST AREA AND EDIT
CC = bwconncomp(bw,4);
STATS= regionprops(bw, 'all');
idx=find([STATS.Area]>2); %%1000 is arbritary
bw2=ismember(labelmatrix(CC), idx);
imwrite(bw2,'THRESHOLDEDIMAGE.jpeg');

%SEE WHICH ARE AT FAULT (DOUBLE CHECKING)
n=CC.NumObjects;
for i = 1:n
    grain = false(size(bw));
    eval(['grain(CC.PixelIdxList{',int2str(i),'})=true;'])
    figure, imshow(grain);
    eval(['title(', int2str(i),');']);
%end

%DISPLAY THE IMAGE TO CONFIRM
disp ('***IMAGE FILE THRESHOLDING COMPLETE***');
disp ('(Check all objects associated with thresholding)');
disp ('The image to be propped is named THRESHOLDEDIMAGE-
JPEG:');
disp ('1. Edit THRESHOLDEDIMAGE-JPEG with windows Paint.');
disp ('2. Run PROP to re-treshold.');
disp ('   *exposed electrolyte area in cm2 will be provided');

%ERODE IMAGE
%se=strel('disk',2); %condition for erosion
%I2=imerode(bw,se);
%figure, imshow(I2);
%title('Eroded Image');

%PLEASE ENTER IMAGE 'REAL' DIMENSIONS
disp('PHOTOSHOP DATA NEEDED:');
width = input ('     Enter Width (mm) of Photoshop File:    ');
height = input ('     Enter Height (mm)of Photoshop File:   ');

%OPEN THE FILE
I=imread('THRESHOLDEDIMAGE.jpeg');
%figure, imshow(I)
%title ('Edited Image');
```

```
%[ypixel,xpixel,zpixel] = size(I);
%xpixelbycm = 2.54*xpixel/DPI;
%ypixelbycm = 2.54*ypixel/DPI;

totalareabymm2 = width*height;
totalareabycm2 = (width/10.0)*(height/10.0);

%RETHRESHOLD THE IMAGE
level=graythresh(I);
rebw=im2bw(I,level);
figure, imshow(rebw);
title('ReThresholded Image');

%FIND IMAGE OF THE LARGEST AREA AND EDIT
CC = bwconncomp(rebw,4);
STATS= regionprops(rebw, 'all');
idx=find([STATS.Area]>10); %%1000 is arbritary
rebw2=ismember(labelmatrix(CC), idx);
%imwrite(rebw2,'neweditedimage.jpeg', 'Quality', 100);

%ONLY ONE AREA IN QUESTION
n=CC.NumObjects;
if (n>1), error ('n > 1: somethings wrong; exist additional
object in image'),end

totareamm2=totalareabymm2*(1-STATS.Solidity);
totareacm2=totalareabycm2*(1-STATS.Solidity);
disp(' ');
disp('CALCULATED DATA:');
fprintf ('Area exposed to electrolyte (pc): %f\n', 1-
STATS.Solidity);
fprintf ('Area exposed to electrolyte (mm2): %f\n',
totareamm2);
fprintf ('Area exposed to electrolyte (cm2): %f\n',
totareacm2);

mycell = { 'width(mm)', 'height(mm)', 'totarea(mm)',
'totarea(cm)', 'NaClArea(%)', 'NaClArea(mm2)',
'NaClArea(cm2)'};
%save data.txt mycell xpixel ypixel -ASCII

filename = 'data.txt';
fid = fopen(filename, 'w');
fprintf(fid, '%s %s %s %s %s %s %s\n', mycell{':,:'});
fprintf(fid, '%f %f %f %f %f %f %f\n', width, height,
totalareabymm2, totalareabycm2, 1-STATS.Solidity, totareamm2,
totareacm2 );
fclose(fid);

disp(' ');
disp('**DATA ALSO SAVED IN DATA.TXT');
```